THE UNIVERSITY OF CHICAGO

CROSS-SPECIES MAPPING OF FUNCTIONAL CONNECTIVITY ALTERATIONS AND THERAPEUTIC RESPONSES IN HYPER-ACUTE ISCHEMIC STROKE

A DISSERTATION SUBMITTED TO
THE FACULTY OF THE DIVISION OF THE BIOLOGICAL SCIENCES
AND THE PRITZKER SCHOOL OF MEDICINE
IN CANDIDACY FOR THE DEGREE OF
DOCTOR OF PHILOSOPHY

COMMITTEE ON MEDICAL PHYSICS

BY
CHISONDI SIMBA WARIOBA

CHICAGO, ILLINOIS
JUNE 2025

Abstract

Since the advent of magnetic resonance imaging (MRI) in the 1970s, the field of medical imaging has witnessed remarkable progress, allowing unprecedented examination of both structural and functional aspects of the human body. Among these developments, functional MRI (fMRI) has emerged as a powerful modality for probing neural activity and deciphering the intricate patterns of connectivity that underlie cognition, perception, and motor control. Resting-state functional MRI (rsfMRI), in particular, provides a non-invasive means of observing the brain's intrinsic functional organization without the need for explicit behavioral tasks, making it especially valuable for investigating complex pathologies such as ischemic stroke, where network-level disruptions can critically influence patient prognosis.

This thesis establishes and validates a rigorous cross-species functional connectivity mapping framework designed to enhance the translational relevance of preclinical stroke models for clinical neuroscience. Focusing on canine models of acute ischemic stroke, it leverages advanced MRI acquisition protocols, comprehensive preprocessing pipelines, and sophisticated computational methods—including manifold alignment algorithms, nonlinear registration techniques, and graph-theoretic analyses—to characterize stroke-induced alterations in large-scale brain networks. Critically, this research evaluates how novel hemodynamic and oxygenation-enhancing interventions, specifically NEH and Sanguinate, modulate these disrupted networks. By quantitatively assessing network reorganization and functional recovery patterns in canines treated with these agents, the framework identifies conserved features of connectivity that can be mapped onto human stroke data.

Building on this cross-species alignment, the thesis employs predictive modeling strategies to infer potential therapeutic outcomes in human stroke patients. Machine learning tools

are used to integrate animal-derived biomarkers, connectivity metrics, and inferred network topologies into predictive models that estimate patient-specific responses to analogous interventions. This approach capitalizes on the biophysical parallels between canine and human cerebrovascular systems, thereby reducing uncertainties associated with direct extrapolation and improving the reliability of translational insights.

The outcomes of this research reinforce the notion that intrinsic network dynamics, captured via rsfMRI, offer crucial information about tissue viability, metabolic demands, and the capacity for functional reorganization following ischemic injury. Moreover, by methodically bridging the gap between preclinical and clinical domains, the thesis demonstrates how cross-species connectivity mapping can inform precision medicine approaches in stroke care. Taken together, these findings not only advance fundamental knowledge of stroke-induced network perturbations but also pave the way for more targeted, evidence-based clinical interventions and the refinement of therapeutic strategies aimed at improving patient outcomes in neurological rehabilitation.

To my father and mother, my birth-mom, my brothers, and my wife

I'm not a traitor to my class. I am just an extreme example of what a working man can achieve.

-Thomas Shelby

Table of Contents

List of Figures

List of Tables

Glossary

BOLD contrast Blood Oxygenation Level Dependent contrast, the basis for fMRI signal detection

canine models Preclinical animal models using canines, valued for their neurovascular similarities to humans in stroke research

cross-species mapping A methodology for aligning and comparing neurobiological data across different species, crucial for translational research

functional connectivity The temporal correlation of neurophysiological events between anatomically separate brain regions

k-space A conceptual space in MRI where spatial frequency information of an image is stored

neurovascular unit A functional ensemble comprising neurons, astrocytes, vascular endothelial cells, pericytes, and smooth muscle cells that regulates cerebral blood flow

penumbra The potentially salvageable tissue surrounding the ischemic core in stroke, characterized by reduced blood flow and altered cellular function

Sanguinate A bovine-derived, pegylated carboxyhemoglobin-based oxygen carrier designed to treat acute ischemic conditions. It functions through a dual mechanism: delivering oxygen to oxygen-deprived tissues while simultaneously releasing carbon monoxide, which helps reduce inflammation and prevent reperfusion injury

stroke A neurological event caused by the interruption of blood supply to the brain, leading to tissue damage and functional impairment

Acronyms

BBB Blood-Brain Barrier

BOLD Blood Oxygenation Level Dependent

CBF Cerebral Blood Flow

CBV Cerebral Blood Volume

CMRO2 Cerebral Metabolic Rate of Oxygen

DCM Dynamic Causal Modeling

DMN Default Mode Network

fMRI Functional Magnetic Resonance Imaging

GLM General Linear Model

HRF Hemodynamic Response Function

ICA Independent Component Analysis

MMP Matrix Metalloproteinase

MRI Magnetic Resonance Imaging

NEH Norepinephrine and Hydralazine

ROS Reactive Oxygen Species

rsfMRI Resting-State Functional MRI

RSN Resting-State Network

SNR Signal-to-Noise Ratio

TE Echo Time

TR Repetition Time

Acknowledgments

I am indebted to the many individuals who have supported, encouraged, and inspired me throughout this journey. Their confidence in my potential and dedication to my success have shaped both my academic pursuits and personal growth.

First and foremost, I extend my deepest gratitude to my advisor, **Dr. Timothy Carroll**. His guidance, intellectual generosity, and trust in my scientific instincts allowed me to pursue my ideas with independence and confidence. His unwavering support and thoughtful counsel were instrumental in guiding me through each stage of this doctoral process.

I am also profoundly grateful to my wife, **Brittany**, whose steadfast love, patience, and partnership have been a constant source of strength. Her understanding and willingness to stand by me during long hours and inevitable setbacks have been indispensable. I am committed to ensuring she knows how much I value her presence in my life and the many ways she has enabled me to persevere.

I owe special thanks to **Dr. Ruth Anne Eatock**, whose insights challenged me to engage more deeply with the neuroscientific implications of my work. Her influence led me to refine my approach under **Dr. Charlotte Stagg** at Oxford University, where I benefited immensely from her team's expertise. I am especially grateful to Dr. Stagg and **Dr. Ioana Grigoras** for guiding me through the neuroscience and statistical analyses that enriched the rigor of my rsfMRI findings.

My early life in Tanzania sparked a curiosity that my father, **Simba**, nurtured, encouraging me to aim high and pursue education abroad. Upon arriving in America, I benefited from mentors who helped me adapt and thrive. Professors **Dr. Ken Kihlstrom**, **Dr. Amanda Silberstein**, and **Professor Carrie Hill** expanded my intellectual horizons, while **Dr.**

Marianne Robins and **Dr. Brandon Haines** fostered my love of learning and research. **Dr. Emily Marshall** provided invaluable guidance during my first rotation, setting a tone of collaboration and respect throughout my graduate studies.

Within my lab and cohort, **Julian Bertini**, **Mira Liu**, **Sagada Penano**, **Gia Jadick**, **Lucas Berens**, and **Amy Renee** helped make the challenges of doctoral work more manageable. I also thank friends such as **Tori Davis**, **Christian Checkcinco**, **Ramses Ngachoko**, **George Mathen**, **Nathan Chen**, and **Luvuyo Magwaza**, whose humor and good spirit provided much-needed balance.

I acknowledge my brothers **Mniko** and **Robert**, and my mother, **Vevette**, whose unwavering belief in my aspirations laid the foundation for my academic journey. Their faith and encouragement have been constants, affirming my efforts at every milestone.

On a lighter note, I'd be remiss not to thank the musicians and artists—**Kendrick Lamar**, **Lana Del Rey**, **Abel Tesfaye**, **Nilüfer Yanya**, **Vampire Weekend**, and others—whose music provided the perfect soundtrack for countless problem sets, journal articles, and late-night writing sessions. Their tunes were my co-pilots, keeping the creative energy (and my sanity) intact.

Completing this PhD has been a collective endeavor, realized through the support, insight, and generosity of many remarkable individuals. To all who have helped me along the way, I offer my most heartfelt gratitude.

Chapter 1 Motivation and Thesis Outline

Over the past several decades, medical imaging techniques have evolved from rudimentary scanning approaches into refined modalities capable of capturing both the structural and functional complexity of the human brain [1]. Within this landscape, **functional MRI (fMRI)** has emerged as a powerful tool, enabling researchers and clinicians to observe intricate patterns of neural activity and connectivity that underpin cognition, perception, and motor control [2]. Such capabilities are especially valuable when investigating **neurological disorders**, where disruptions in brain networks can shed light on underlying disease mechanisms, inform prognoses, and guide the development of more effective therapeutic interventions.

Ischemic stroke, a leading contributor to mortality and long-term disability worldwide, highlights the importance of these network-level perspectives. Although current treatments exist, they often reach only a fraction of patients, emphasizing the urgent need for novel therapeutic approaches that broaden treatment windows or enhance overall outcomes [3]. In this context, **resting-state functional MRI (rsfMRI)** provides a powerful platform. By capturing the brain's intrinsic functional organization without relying on explicit tasks, rsfMRI allows researchers to assess large-scale network disruptions—a critical factor in understanding stroke pathophysiology and recovery potential [4, 5].

To advance beyond isolated findings and toward a translational framework, this thesis integrates rsfMRI approaches with **canine models**, whose neurovascular and anatomical similarities to humans offer a more direct path for translating preclinical insights. Additionally, it

explores emerging treatments such as **NEH (norepinephrine and hydralazine)** and **Sanguinate**, aiming to establish a robust **cross-species connectivity mapping** framework that bridges preclinical results and human clinical applications. Ultimately, this approach aspires to guide stroke research toward more personalized and impactful therapies.

1.1 Thesis Outline

The chapters that follow are organized to progress from foundational principles to practical methodologies and, ultimately, clinical translation:

- **Chapter 2 - Introduction** offers a comprehensive overview of rsfMRI-based functional connectivity in the context of ischemic stroke, elaborates on the rationale for employing canine models, and introduces the novel therapeutic agents (NEH and Sanguinate). It also consolidates the thesis objectives, research aims, and hypotheses to provide a cohesive roadmap for the ensuing chapters.

- **Chapter 3 - Background** delves into the technical and theoretical underpinnings of MRI, fMRI, and rsfMRI, as well as the mathematical frameworks underpinning functional connectivity analysis. It examines the principles governing the blood-oxygen-level-dependent (BOLD) signal, the pathophysiology of ischemic stroke at molecular and network scales, and existing cross-species mapping strategies, setting the stage for the methodological developments that follow.

- **Chapter 4 - Development of a Cross-Species Connectivity Mapping Framework** details the experimental protocols, imaging parameters for canine models, preprocessing pipelines, and computational methods employed to align and compare connectivity patterns between canines and humans.

- **Chapter 5 - Results of Cross-Species Connectivity Mapping** presents empirical findings using the developed framework. It characterizes how ischemic stroke and

subsequent interventions (NEH and Sanguinate) alter connectivity in canine models and evaluates how these patterns relate to human data, thereby validating and refining the cross-species approach.

- **Chapter 6 - Predictive Modeling of Human Stroke Outcomes** leverages insights derived from preclinical data and cross-species comparisons to build predictive models for human stroke responses. By applying machine learning techniques, this chapter explores how network-level characterizations can forecast therapeutic outcomes and recovery trajectories, informing personalized treatment strategies.

- **Chapter 7 - Conclusions and Recommendations for Future Work** synthesizes the key contributions of this thesis, highlighting advances in cross-species mapping and predictive modeling. It concludes by suggesting directions for future research, including methodological refinements and the exploration of additional therapeutic modalities.

In essence, this thesis aims to deepen our understanding of stroke-induced connectivity alterations, establish a framework for cross-species translational research, and pave the way for more effective, patient-tailored interventions in stroke care.

Chapter 2 Introduction

This chapter provides the conceptual and contextual foundation for the research presented in this thesis. It begins by offering a comprehensive overview of **resting-state functional MRI (rsfMRI)** and its significance in understanding **functional connectivity**—particularly in the context of **ischemic stroke**, where disruptions in brain networks critically impact patient recovery and therapeutic effectiveness.

Next, the chapter explains the rationale for employing **canine models** as a translational bridge between preclinical studies and human applications. Canines, with their human-like neurovascular architectures and functional connectivity patterns, present a unique opportunity to investigate the pathophysiological underpinnings of stroke at a systems level. A thorough justification for their use will be presented, coupled with a comparison to other animal models and an assessment of their strengths and limitations.

Further, this chapter introduces the novel therapeutic interventions under investigation—**NEH (norepinephrine and hydralazine)** and **Sanguinate**—which offer the prospect of improving blood flow, oxygenation, and ultimately connectivity preservation post-stroke. Their potential mechanisms, relevance to clinical scenarios, and current standing in preclinical research will be delineated.

Bringing these elements together, the chapter then articulates the **thesis objectives, research aims, and hypotheses**. By outlining these goals in detail here—rather than distributing them across multiple chapters—this chapter serves as the primary reference point for the motivations, questions, and anticipated contributions of the research. It sets the stage for the technical background, methodological frameworks, and predictive modeling strategies that will follow in subsequent chapters.

2.1 Resting-State fMRI and its Importance in Stroke Research

Resting-state fMRI provides a non-invasive means of probing the brain's intrinsic activity. Without the need for explicit tasks, rsfMRI can reveal temporally correlated fluctuations in the Blood-Oxygen-Level-Dependent (BOLD) signal, thereby uncovering **resting-state networks (RSNs)** that represent fundamental organizational principles of the human brain [6]. In stroke, these RSNs often exhibit disrupted connectivity, reflecting underlying damage and compensatory mechanisms at both local and global scales [4, 7].

Identifying and quantifying these connectivity alterations is crucial for understanding stroke pathophysiology. Beyond assessing the extent of damage, rsfMRI-based connectivity metrics can predict recovery potential, gauge the effectiveness of treatments, and guide rehabilitation strategies. These capabilities position rsfMRI as an indispensable tool in stroke research, enabling objective evaluations of interventions like NEH and Sanguinate that aim to restore or enhance functional network integrity.

2.2 Rationale for Using Canine Models

Animal models are cornerstone tools in biomedical research, providing controlled platforms for elucidating disease mechanisms and testing candidate therapies before moving into human trials. While rodent models are widely used due to accessibility and cost-effectiveness, their lissencephalic brains and differing cerebrovascular dynamics limit their translational relevance for complex conditions like stroke.

Canine models offer several advantages in this context. Their brain size, degree of gyrencephaly, and vascular anatomy more closely approximate human conditions [8]. This anatomical and functional similarity facilitates the analysis of functional connectivity patterns that bear greater resemblance to human RSNs (Figure 4.1). By examining how ischemic insults and subsequent treatments modify these networks in canines, researchers gain insights

more directly applicable to the human brain.

Moreover, because canines naturally possess a more human-like cortical complexity, their post-stroke connectivity patterns and responses to interventions can yield richer datasets for understanding network-level changes. This forms a stronger foundation for cross-species mapping, enabling the development of algorithms and metrics that more accurately align canine and human connectivity data.

2.3 Introduction to NEH and Sanguinate Therapies

Current stroke interventions, including thrombolysis and mechanical thrombectomy, remain constrained by narrow therapeutic windows and patient eligibility criteria [3]. Emerging treatments target alternative pathways, such as improved perfusion or enhanced oxygen delivery to vulnerable brain regions. In this vein, **NEH (norepinephrine and hydralazine)** and **Sanguinate** have been proposed as novel strategies.

NEH therapy modulates systemic hemodynamics to preserve perfusion in ischemic territories, potentially stabilizing or restoring disrupted connectivity [9]. Sanguinate, an oxygen-carrying solution, aims to enhance oxygen delivery beyond what standard reperfusion therapies achieve, potentially mitigating the metabolic deficits that compromise network integrity [10].

Investigating these therapies in canine models via rsfMRI connectivity analyses offers a clearer picture of their network-level impact. By quantifying how these interventions shift the functional connectivity landscape—restoring certain RSNs, enhancing coupling between critical nodes, or modifying global network topology—we can begin to understand their mechanisms and therapeutic potential in a more targeted manner.

2.4 Thesis Objectives, Research Aims, and Hypotheses

The overarching goal of this thesis is to **develop and validate a cross-species functional connectivity mapping framework** that enables robust translation of findings from canine stroke models to human stroke conditions. Within this broad objective lie several interconnected aims:

1. **Characterize Functional Connectivity Alterations in Canine Models**: Examine rsfMRI data from canine models pre- and post-occlusion to identify network-specific changes in connectivity induced by ischemic stroke. Evaluate how NEH and Sanguinate therapies influence these patterns, testing the hypothesis that such interventions can differentially preserve or restore functional connectivity.

2. **Develop a Cross-Species Mapping Framework**: Establish computational and mathematical strategies for aligning canine and human connectivity data. This involves implementing advanced registration algorithms and similarity metrics that accommodate anatomical and organizational differences. The hypothesis here is that despite evolutionary divergences, fundamental aspects of network organization can be reliably matched across species.

3. **Build Predictive Models for Translational Insights**: Leverage the cross-species alignment to construct predictive models that infer potential human therapeutic responses based on canine data. The hypothesis is that the connectivity changes observed in canine models following interventions can serve as predictive biomarkers for human stroke patients, guiding treatment selection and informing prognostic assessments.

Together, these aims and hypotheses form a cohesive framework for advancing translational stroke research. By thoroughly characterizing connectivity disruptions, establishing a cross-species bridge, and ultimately linking preclinical insights to clinical predictions, the

thesis aspires to make meaningful contributions to the field of neuroimaging, stroke therapy, and precision medicine.

Subsequent chapters will build upon this foundation. Chapter 3 provides the technical and theoretical background needed for the connectivity analyses and cross-species mapping methods, while Chapters 4 through 6 detail the methodologies, results, and predictive modeling approaches. Finally, Chapter 7 consolidates these findings, offering reflections on the progress made and identifying promising directions for future investigations.

Chapter 3 Background

This chapter provides the theoretical and mathematical foundation for understanding the principles of magnetic resonance imaging (MRI), functional MRI (fMRI), and resting-state functional MRI (rsfMRI). It begins by introducing the physics of MRI, including key concepts such as nuclear spin, magnetic moment, Boltzmann distribution, Bloch equations, and the dynamics of nuclear spins under an external magnetic field. The discussion transitions to the mathematical basis for signal acquisition and reconstruction, followed by an exploration of the Blood-Oxygen-Level-Dependent (BOLD) signal and the neurovascular mechanisms that influence its generation. The chapter also introduces the principles of functional connectivity analysis in both task-based and resting-state paradigms, with an emphasis on the mathematical frameworks used to quantify connectivity. Finally, it explores the pathophysiology of ischemic stroke and outlines cross-species mapping frameworks, emphasizing their relevance and challenges in translational neuroscience.

3.1 Physics and Mathematics of Magnetic Resonance Imaging (MRI)

Magnetic Resonance Imaging (MRI) is a sophisticated and non-invasive imaging technique that provides high-resolution images of the internal structures of the body. By exploiting the intrinsic magnetic properties of atomic nuclei, particularly hydrogen protons abundant in biological tissues, MRI enables detailed visualization without the use of ionizing radiation. Understanding the fundamental principles of MRI requires an exploration of nuclear spin dynamics, magnetic field interactions, signal generation and detection, spatial encoding, and the mathematical frameworks that govern these phenomena.

3.1.1 Basic Principles of MRI

At the core of MRI lies the manipulation of nuclear spins within an external magnetic field and the detection of the resulting signals [11]. This process involves a complex interplay between quantum mechanics and classical electromagnetism, allowing for the generation of images based on the magnetic properties of different tissues.

Nuclear Spin and Magnetic Moment

Atomic nuclei are composed of protons and neutrons, each possessing an intrinsic angular momentum known as **spin**. This spin is a fundamental quantum mechanical property and is quantized. In nuclei with an odd number of protons or neutrons, such as hydrogen (^{1}H), there is a net nuclear spin due to the unpaired nucleon [12, 11, 13].

Associated with the nuclear spin $\mathbf{I}$ is a **magnetic moment** $\boldsymbol{\mu}$, which arises because the spinning charged particle generates a tiny magnetic field, analogous to a small bar magnet. The magnetic moment is given by:

$$\boldsymbol{\mu} = \gamma \hbar \mathbf{I}, \tag{3.1}$$

where γ is the gyromagnetic ratio, a constant specific to each type of nucleus (for hydrogen, $\gamma \approx 42.58\,\mathrm{MHz\,T^{-1}}$), and $\hbar$ is the reduced Planck constant. In a macroscopic sample, the individual magnetic moments are randomly oriented due to thermal motion, resulting in no net magnetization at the macroscopic level.

Alignment in an External Magnetic Field

When a sample containing nuclei with spin is placed in a strong static external magnetic field $\mathbf{B}_0$, typically oriented along the z-axis, the magnetic moments experience a torque that tends to align them with the field [11, 13]. Quantum mechanics dictates that the component

of the nuclear spin along the direction of the magnetic field can only take on certain discrete values, leading to quantized energy states. For spin-$\frac{1}{2}$ nuclei like hydrogen, there are two possible energy states: a lower energy state where the magnetic moment is aligned with $\mathbf{B}_0$ (parallel) and a higher energy state where it is opposed to $\mathbf{B}_0$ (antiparallel).

The slight excess of nuclei in the lower energy state results in a net macroscopic magnetization vector $\mathbf{M}_0$ aligned along $\mathbf{B}_0$ [11]. The population difference between the two energy states is given by the Boltzmann distribution:

$$\frac{N_\uparrow}{N_\downarrow} = e^{\Delta E/kT}, \tag{3.2}$$

where $N_\uparrow$ and $N_\downarrow$ are the number of nuclei in the low and high energy states, respectively, $\Delta E = \hbar\omega_0$ is the energy difference between the states, k is Boltzmann's constant, and T is the absolute temperature. The net magnetization is proportional to the strength of the external magnetic field and inversely proportional to the temperature:

$$M_0 = \frac{N\gamma^2\hbar^2 B_0}{4kT}, \tag{3.3}$$

where N is the number of spins per unit volume. This relationship underscores the importance of strong magnetic fields in achieving a detectable signal in MRI.

Larmor Precession and Resonance

The magnetic moments do not align perfectly with $\mathbf{B}_0$ but instead precess around the direction of the magnetic field due to the torque exerted by $\mathbf{B}_0$. This precessional motion occurs at the **Larmor frequency** ω_0, given by:

$$\omega_0 = \gamma B_0. \tag{3.4}$$

This frequency is specific to the type of nucleus and the strength of the magnetic field.

For hydrogen nuclei in a 1.5 Tesla field, $\omega_0 \approx 63.86\,\text{MHz}$. The precession can be visualized as the magnetic moments tracing out cones around the direction of $\mathbf{B}_0$.

Resonance is achieved when an external radiofrequency (RF) magnetic field $\mathbf{B}_1$, oscillating at the Larmor frequency, is applied perpendicular to $\mathbf{B}_0$. This RF field can induce transitions between the energy states of the nuclei, effectively tipping the net magnetization vector $\mathbf{M}$ away from alignment with $\mathbf{B}_0$ and into the transverse (xy) plane. The resonance condition allows for efficient energy transfer and is essential for manipulating the net magnetization [13].

RF Excitation and the Rotating Frame

To analyze the effects of the RF field on the magnetization vector, it is convenient to adopt a **rotating frame of reference** that rotates at the Larmor frequency ω_0. In this frame, the $\mathbf{B}_1$ field appears stationary, simplifying the dynamics of the system. The magnetization vector $\mathbf{M}$ precesses around $\mathbf{B}_1$ at a frequency determined by the magnitude of $\mathbf{B}_1$.

The angle by which $\mathbf{M}$ is tipped away from the z-axis, known as the **flip angle** α, is given by:

$$\alpha = \gamma B_1 \tau, \tag{3.5}$$

where τ is the duration of the RF pulse. By controlling the amplitude and duration of the RF pulse, specific flip angles can be achieved (e.g., 90° for maximum transverse magnetization or 180° for inversion of the magnetization).

Relaxation Processes

After the RF pulse is terminated, the magnetization vector $\mathbf{M}$ begins to return to its equilibrium state along $\mathbf{B}_0$. This relaxation process involves two key mechanisms (Figure 3.1):

longitudinal relaxation (spin-lattice relaxation) and **transverse relaxation** (spin-spin relaxation).

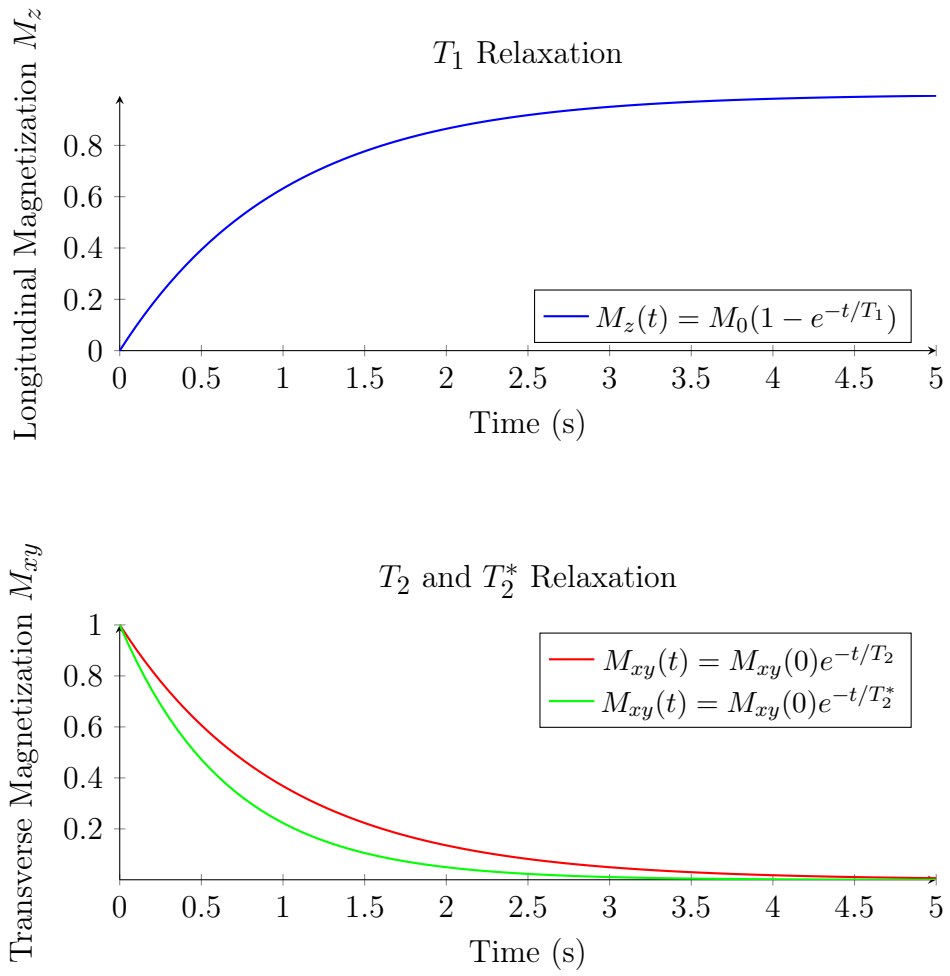

Figure 3.1: Illustration of relaxation processes in MRI (a) T_1 **Relaxation**: The recovery of longitudinal magnetization (M_z) following an RF pulse, characterized by the time constant T_1. Different tissues exhibit distinct T_1 values, contributing to image contrast. (b) T_2 **and** T_2^* **Relaxation**: The decay of transverse magnetization (M_{xy}) due to spin-spin interactions (T_2) and magnetic field inhomogeneities (T_2^*). The faster decay observed in T_2^* relaxation highlights the additional effect of magnetic field inhomogeneities, which can be partially corrected using spin echo techniques.

Longitudinal Relaxation (T_1 Relaxation) Longitudinal relaxation describes the recovery of the magnetization component along the z-axis (M_z) back toward its equilibrium value M_0. This process occurs as the spins release energy to their surroundings, or lattice, allowing

the system to return to thermal equilibrium. The recovery follows an exponential function:

$$M_z(t) = M_0(1 - e^{-t/T_1}), \tag{3.6}$$

where T_1 is the longitudinal relaxation time constant, characteristic of the tissue and its molecular environment. Tissues with tightly bound water molecules, such as fat, tend to have shorter T_1 times, while those with more freely moving water, like cerebrospinal fluid, have longer T_1 times.

Transverse Relaxation (T_2 Relaxation) Transverse relaxation refers to the decay of the magnetization component in the transverse plane (M_{xy}) due to dephasing of the individual spins. This dephasing arises from interactions between neighboring spins, leading to slight variations in their precessional frequencies. The decay is exponential:

$$M_{xy}(t) = M_{xy}(0)e^{-t/T_2}, \tag{3.7}$$

where T_2 is the transverse relaxation time constant. Like T_1, T_2 varies among different tissues and contributes to image contrast in T2-weighted imaging.

Combined Effects and T_2^* Relaxation In practice, the observed decay of transverse magnetization is faster than predicted by T_2 relaxation alone due to magnetic field inhomogeneities and susceptibility differences within tissues. This combined effect is characterized by the time constant T_2^*:

$$\frac{1}{T_2^*} = \frac{1}{T_2} + \frac{1}{T_{\text{inh}}}, \tag{3.8}$$

where T_{inh} accounts for dephasing caused by inhomogeneities in the external magnetic field $\mathbf{B}_0$. Techniques such as spin echo sequences can refocus some of these dephasing effects, isolating true T_2 relaxation.

Tissue Contrast and Relaxation Times

The differences in T_1 and T_2 relaxation times among various tissues (Figure 3.2) are fundamental to the contrast observed in MRI images. For example, fat has a relatively short T_1 and T_2 due to efficient energy exchange and restricted molecular motion, resulting in bright signals on T1-weighted images. In contrast, fluids like cerebrospinal fluid have long T_1 and T_2 times, appearing dark on T1-weighted images and bright on T2-weighted images [12]. By adjusting imaging parameters such as repetition time (TR) and echo time (TE), MRI can emphasize these differences to produce images with desired contrast characteristics.

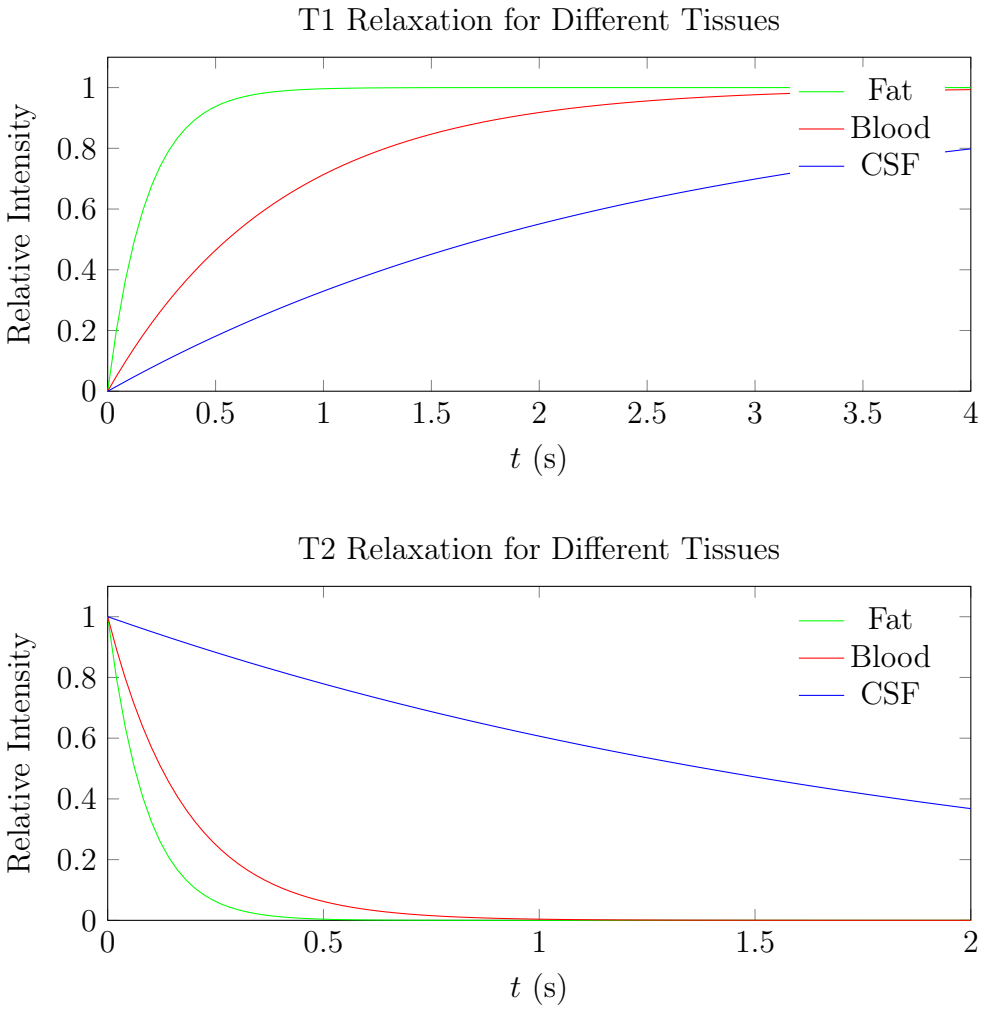

Figure 3.2: Time courses of magnetization recovery for T1 relaxation (top) and decay for T2 relaxation (bottom) are shown for different tissue types: fat, blood, and cerebrospinal fluid (CSF). The T1 plot highlights the differences in longitudinal recovery, with fat showing the fastest relaxation, followed by blood, and then CSF, due to variations in molecular environments and energy exchange efficiency. The T2 plot demonstrates the differences in transverse decay rates, where CSF exhibits the slowest decay, indicating a longer T2 time, while fat decays much more quickly. These distinctions in relaxation times are fundamental for generating tissue contrast in MRI, with each tissue type contributing unique signal characteristics based on its specific T1 and T2 relaxation properties.

3.1.2 MRI Hardware Components

The successful implementation of MRI relies on specialized hardware designed to generate precise magnetic fields, transmit and receive RF signals, and process the resulting data. The

main components include the main magnet, gradient coils, and RF coils.

Main Magnet

The main magnet produces the strong, static magnetic field $\mathbf{B}_0$ required to align the nuclear spins. Most clinical MRI systems use superconducting magnets capable of generating fields ranging from 1.5 to 7 Tesla [12]. These magnets are cooled to extremely low temperatures using liquid helium to maintain superconductivity, allowing for high field strengths with excellent homogeneity across the imaging volume. Field uniformity is critical because variations in $\mathbf{B}_0$ can lead to image distortions and artifacts. Shim coils and passive shimming techniques are employed to fine-tune the magnetic field and correct for inhomogeneities.

Gradient Coils

Gradient coils are essential for spatial encoding in MRI. They produce controlled, linear variations in the magnetic field along the x, y, and z axes, superimposed on the main magnetic field $\mathbf{B}_0$. The gradients cause the Larmor frequency to become position-dependent:

$$\omega(\mathbf{r}) = \gamma(B_0 + G_x x + G_y y + G_z z), \tag{3.9}$$

where G_x, G_y, and G_z are the gradient strengths along their respective axes, and $\mathbf{r} = (x, y, z)$ represents position. By manipulating the gradient strengths and durations, spatial information is encoded into the frequency and phase of the MR signals. Gradient coils are precisely engineered to produce linear field variations with minimal distortion and are capable of rapid switching, which is crucial for advanced imaging techniques.

RF Coils

RF coils serve as both transmitters and receivers in MRI:

Transmit Coils Transmit coils generate the RF pulses necessary to excite the spins [13]. They are designed to produce a uniform $\mathbf{B}_1$ field over the region of interest to ensure consistent excitation. Body coils, which are integrated into the scanner bore, are commonly used for whole-body imaging, while specialized coils may be employed for specific anatomical regions.

Receive Coils Receive coils detect the weak MR signals emitted by the precessing transverse magnetization [13]. Coil sensitivity and geometry significantly affect the signal-to-noise ratio (SNR). Surface coils are placed close to the area of interest to maximize SNR, while phased-array coils consist of multiple small coil elements that can improve spatial resolution and enable advanced techniques like parallel imaging.

3.1.3 Spatial Encoding and K-Space

Spatial encoding allows MRI to reconstruct spatially resolved images from the MR signals [11]. This is achieved through the application of gradient fields and the collection of data in the frequency domain, known as **k-space**.

Slice Selection

To image a specific slice within the body, a gradient field (e.g., G_z) is applied along the z-axis during the RF excitation pulse. This gradient causes the Larmor frequency to vary linearly with position along z:

$$\omega(z) = \gamma(B_0 + G_z z). \tag{3.10}$$

By applying an RF pulse with a frequency bandwidth $\Delta\omega$, only spins within a slice of thickness Δz are excited:

$$\Delta z = \frac{\Delta \omega}{\gamma G_z}. \tag{3.11}$$

Using a sinc-shaped RF pulse ensures a rectangular frequency profile, providing precise slice selection and minimizing excitation of adjacent slices.

Frequency Encoding (Readout Gradient)

After slice selection, spatial encoding within the slice is achieved using frequency and phase encoding gradients [11]. The frequency encoding gradient (G_x) is applied along the x-axis during signal acquisition. This gradient causes the Larmor frequency to vary with position along x:

$$\omega(x) = \gamma(B_0 + G_x x). \tag{3.12}$$

As a result, spins at different x-positions precess at different frequencies. The received signal is a superposition of these frequencies, and applying a Fourier transform allows for the reconstruction of spatial information along the x-axis.

Phase Encoding

Phase encoding involves applying a gradient (G_y) along the y-axis for a short duration before signal acquisition. This gradient induces a position-dependent phase shift in the spins:

$$\phi(y) = \gamma G_y y \Delta t, \tag{3.13}$$

where Δt is the duration of the phase encoding gradient. By incrementally changing the amplitude of G_y across multiple repetitions (called phase encoding steps), different phase encodings are obtained, enabling spatial resolution along the y-axis. Collecting data with varying phase encoding gradients fills k-space line by line [11].

K-Space and Image Reconstruction

K-space is a conceptual space where each point corresponds to a specific spatial frequency component of the image [11, 13]. The coordinates in k-space are defined by:

$$k_x(t) = \gamma \int_0^t G_x(t')dt', \quad k_y = \gamma G_y \Delta t. \tag{3.14}$$

The MR signal $S(k_x, k_y)$ acquired during readout is related to the spatial distribution of magnetization $\rho(x, y)$ by the Fourier transform:

$$S(k_x, k_y) = \int_{-\infty}^{\infty} \int_{-\infty}^{\infty} \rho(x, y) e^{-i2\pi(k_x x + k_y y)} dx dy. \tag{3.15}$$

Reconstructing the image involves performing an inverse Fourier transform of the k-space data:

$$\rho(x, y) = \int_{-\infty}^{\infty} \int_{-\infty}^{\infty} S(k_x, k_y) e^{i2\pi(k_x x + k_y y)} dk_x dk_y. \tag{3.16}$$

The sampling density and trajectory in k-space influence the resolution and quality of the reconstructed image.

K-Space Sampling Strategies

Different strategies are used to fill k-space (Figure 3.3), each affecting acquisition time, image quality, and sensitivity to artifacts:

Cartesian Sampling In Cartesian sampling, k-space is filled line by line in a rectilinear fashion by sequentially varying the phase encoding gradient. This method is straightforward and compatible with fast Fourier transform algorithms but can be sensitive to motion artifacts.

Radial and Spiral Sampling Radial sampling acquires data along spokes radiating from the center of k-space, while spiral sampling traverses k-space in a spiral trajectory. These methods offer robustness against motion artifacts and can provide faster acquisition times but require more complex reconstruction algorithms.

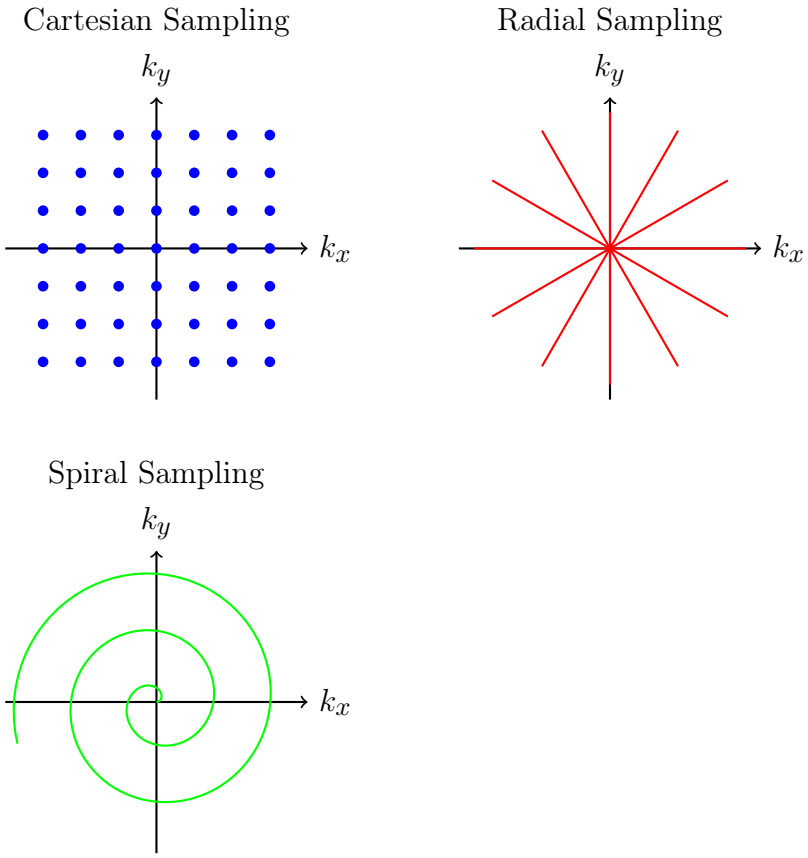

Figure 3.3: Illustration of different k-space sampling strategies. **Top left**: Cartesian sampling, where k-space is filled line by line in a rectilinear manner. This method is compatible with fast Fourier transform algorithms and provides straightforward reconstruction but is sensitive to motion artifacts. **Top right**: Radial sampling, which acquires data along spokes radiating from the center of k-space. This approach is more robust to motion artifacts and can provide fast acquisitions but requires more complex reconstruction. **Bottom**: Spiral sampling, where data is acquired in a spiral trajectory. Spiral sampling is efficient in acquisition time and is less sensitive to motion, but its reconstruction is computationally intensive due to the non-Cartesian path.

3.1.4 Pulse Sequences and Image Contrast

Pulse sequences define the timing and application of RF pulses and gradient fields, controlling the contrast and quality of the MRI images [11, 13]. Key parameters influencing image contrast include repetition time (TR), echo time (TE), and flip angle (α).

Repetition Time (TR) and Echo Time (TE)

The **repetition time** TR is the time interval between successive excitation pulses. It determines the extent of longitudinal relaxation that occurs between excitations, influencing T1 weighting. A short TR minimizes T1 relaxation differences, while a long TR allows for greater recovery of M_z.

The **echo time** TE is the time between the excitation pulse and the peak of the echo signal. TE affects the amount of transverse relaxation that influences the signal, thereby controlling T2 or T2* weighting. A short TE reduces T2 decay effects, while a long TE accentuates differences in T2 relaxation times among tissues.

By adjusting TR and TE, different tissue contrasts can be achieved:

- **T1-Weighted Imaging**: Short TR and short TE emphasize differences in T1 relaxation times, making tissues with short T1 appear bright.
- **T2-Weighted Imaging**: Long TR and long TE emphasize differences in T2 relaxation times, highlighting tissues with long T2.
- **Proton Density Imaging**: Long TR and short TE minimize relaxation effects, emphasizing differences in proton density.

Flip Angle

The flip angle α determines the extent to which the net magnetization is tipped into the transverse plane during excitation. In gradient echo sequences, varying the flip angle allows for control over image contrast and can reduce acquisition times. Smaller flip angles reduce saturation effects and allow for shorter TR, enabling faster imaging.

Spin Echo and Gradient Echo Sequences

Spin Echo Sequences Spin echo sequences (Figure 3.4) use a 90° excitation pulse followed by a 180° refocusing pulse. The 180° pulse inverts the dephased spins, refocusing them at time TE to form an echo [11]. This sequence compensates for dephasing due to magnetic field inhomogeneities and is sensitive to true T2 relaxation. Spin echo sequences are considered the gold standard for image contrast but have longer acquisition times compared to gradient echo sequences.

Gradient Echo Sequences Gradient echo sequences (Figure 3.4) use variable flip angles and gradient reversals to refocus spins without the need for a 180° pulse [11]. These sequences are faster and more versatile but are sensitive to T2* effects due to field inhomogeneities. They are useful in applications where rapid imaging is required, such as dynamic studies and functional MRI.

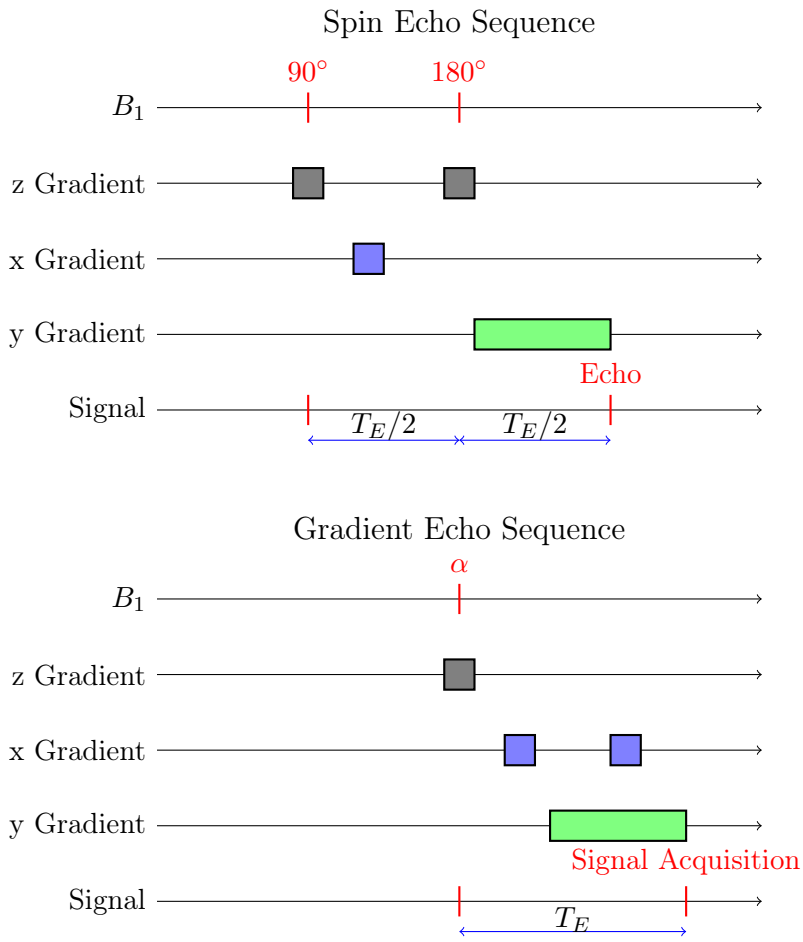

Figure 3.4: **Comparison of Spin Echo and Gradient Echo Pulse Sequences.** The spin echo sequence (top) uses a 90° excitation pulse followed by a 180° refocusing pulse to correct for magnetic field inhomogeneities, producing an echo at time T_E. In contrast, the gradient echo sequence (bottom) uses a variable flip angle excitation pulse (α) and gradient reversals to achieve faster imaging, with sensitivity to T2* effects. Spin echo sequences offer accurate T2 contrast, while gradient echo sequences are suited for rapid imaging but are more susceptible to artifacts.

Advanced Pulse Sequences

Advanced imaging techniques utilize specialized pulse sequences to achieve specific imaging goals:

Inversion Recovery Inversion recovery sequences begin with an inversion pulse (typically 180°) to invert the net magnetization. By selecting an appropriate inversion time (TI), tissues

with specific T1 values can be nulled, enhancing contrast between different tissues. For example, fluid-attenuated inversion recovery (FLAIR) suppresses signals from cerebrospinal fluid to better visualize lesions in the brain.

Fast Spin Echo (Turbo Spin Echo) Fast spin echo sequences acquire multiple echoes following a single excitation by using a train of 180° refocusing pulses. This approach significantly reduces scan time while maintaining T2 weighting. It is widely used in clinical imaging due to its efficiency and image quality.

Echo Planar Imaging (EPI) Echo planar imaging enables the rapid acquisition of an entire image following a single excitation pulse by traversing k-space in a single shot. EPI is critical for applications that require high temporal resolution, such as functional MRI and diffusion imaging. However, it is sensitive to magnetic field inhomogeneities and may suffer from geometric distortions.

3.1.5 Applications and Clinical Imaging

MRI's versatility and superior soft tissue contrast make it invaluable in numerous clinical and research applications.

Brain Imaging

High-resolution structural imaging of the brain is essential for diagnosing neurological conditions. T1-weighted imaging provides detailed anatomical structures, useful for detecting tumors, malformations, and assessing brain development. T2-weighted imaging highlights fluid-filled spaces and pathological changes such as edema, inflammation, and demyelination, aiding in the diagnosis of multiple sclerosis, stroke, and infections.

Functional MRI (fMRI) Functional MRI maps brain activity by detecting changes in blood oxygenation levels, leveraging the BOLD contrast mechanism discussed earlier. It allows for the non-invasive study of brain function, connectivity, and neural networks, providing insights into cognitive processes and neurological disorders.

Cardiac Imaging

MRI offers a comprehensive, non-invasive assessment of cardiac structure and function. Cine MRI captures dynamic images of the beating heart, enabling evaluation of ventricular function, wall motion, and valvular function [12]. Perfusion imaging assesses myocardial blood flow using contrast agents, aiding in the detection of ischemia. Late gadolinium enhancement identifies areas of myocardial infarction or fibrosis by highlighting regions where contrast agent accumulates due to damaged myocardium.

Musculoskeletal Imaging

MRI provides excellent soft tissue contrast for evaluating muscles, ligaments, tendons, and cartilage. Fat-suppressed imaging enhances visualization of edema, inflammation, and tumors by suppressing signals from fatty tissues. Cartilage imaging assesses cartilage integrity and degeneration in joint diseases like osteoarthritis, using techniques such as T2 mapping and delayed gadolinium-enhanced MRI of cartilage (dGEMRIC) [12].

3.1.6 Bloch Equations and Spin Dynamics

The **Bloch equations** provide a semiclassical description of nuclear magnetic resonance phenomena, combining quantum mechanical principles with classical electromagnetic theory. For a magnetization vector $\mathbf{M} = (M_x, M_y, M_z)$ under an external magnetic field $\mathbf{B}$, the

equations take the form:

$$\frac{d\mathbf{M}}{dt} = \gamma \mathbf{M} \times \mathbf{B} - \begin{pmatrix} \frac{M_x}{T_2} \\ \frac{M_y}{T_2} \\ \frac{M_z - M_0}{T_1} \end{pmatrix}. \tag{3.17}$$

When considering both static ($\mathbf{B}_0$) and time-varying ($\mathbf{B}_1(t)$) fields, the total field becomes:

$$\mathbf{B}(t) = B_0 \hat{k} + B_1(t)[\cos(\omega t)\hat{i} + \sin(\omega t)\hat{j}]. \tag{3.18}$$

Rotating Frame Analysis

The transformation to the rotating frame introduces a coordinate system (x', y', z') rotating at angular frequency ω about the z-axis [11, 13]. The transformation matrix $\mathbf{R}(t)$ is given by:

$$\mathbf{R}(t) = \begin{pmatrix} \cos(\omega t) & \sin(\omega t) & 0 \\ -\sin(\omega t) & \cos(\omega t) & 0 \\ 0 & 0 & 1 \end{pmatrix}. \tag{3.19}$$

The effective field in this frame becomes:

$$\mathbf{B}_{\text{eff}} = \left(B_0 - \frac{\omega}{\gamma} \right) \hat{k} + B_1 \hat{i}'. \tag{3.20}$$

Solutions and Applications

For specific cases, analytical solutions exist [11]. During free precession with no RF field:

$$M_{xy}(t) = M_{xy}(0) e^{-t/T_2} e^{-i\gamma \Delta B_0 t} \tag{3.21}$$

$$M_z(t) = M_0 - [M_0 - M_z(0)] e^{-t/T_1} \tag{3.22}$$

For more complex scenarios involving time-varying gradients $\mathbf{G}(t)$, the Bloch equations

become:

$$\frac{d\mathbf{M}}{dt} = \gamma \mathbf{M} \times [\mathbf{B}_0 + \mathbf{G}(t) \cdot \mathbf{r} + \mathbf{B}_1(t)] - \mathbf{R}(\mathbf{M}) \tag{3.23}$$

where $\mathbf{R}(\mathbf{M})$ represents the relaxation terms [11].

These equations form the basis for advanced pulse sequence design, including:

- Composite pulse optimization
- Adiabatic pulse design
- Magnetization preparation schemes
- Multi-component relaxation analysis

Numerical solutions typically employ methods such as the Runge-Kutta algorithm or matrix exponential approaches for accurate trajectory prediction, particularly important in quantitative imaging applications.

3.1.7 Summary

Magnetic Resonance Imaging combines principles of physics, mathematics, and engineering to produce detailed images of the body's internal structures. By manipulating nuclear spins with precisely timed magnetic fields and RF pulses, MRI offers unparalleled flexibility and contrast in medical imaging. A deep understanding of the underlying physics and mathematical models is crucial for advancing MRI technology, improving image quality, and expanding its clinical applications. This foundation sets the stage for exploring advanced topics such as functional MRI and the study of resting-state functional connectivity, which continue to enhance our understanding of human physiology and disease.

3.2 Functional MRI and Resting-State fMRI

Functional Magnetic Resonance Imaging (fMRI) is a non-invasive neuroimaging technique that enables researchers and clinicians to observe brain activity by detecting changes associated with blood flow. It leverages the principle that cerebral blood flow and neuronal activation are coupled; when a region of the brain is active, blood flow to that area increases. Resting-State fMRI (rsfMRI) extends this capability by examining the brain's functional organization during rest, revealing intrinsic connectivity networks without the need for explicit tasks or stimuli.

3.2.1 Principles of fMRI

The fundamental principle underlying fMRI is the detection of changes in blood oxygenation levels that occur in response to neural activity. This mechanism is known as the **Blood Oxygenation Level Dependent** (BOLD) contrast [14, 15]. Active neurons consume oxygen and glucose, leading to localized changes in the concentration of oxygenated and deoxygenated hemoglobin. Oxygenated hemoglobin is diamagnetic, while deoxygenated hemoglobin is paramagnetic, affecting the local magnetic field and thus the MR signal [16, 17].

During neuronal activation, the increase in cerebral blood flow (CBF) to a region is typically greater than the increase in oxygen consumption [15]. This results in a net decrease in the concentration of deoxygenated hemoglobin (dHb) in that area. Since dHb causes local magnetic field inhomogeneities that shorten the effective transverse relaxation time T_2^*, a decrease in dHb leads to an increased T_2^* and, consequently, an increase in the MR signal in T2*-weighted images. This signal change forms the basis of the BOLD contrast used in fMRI [15, 6, 2].

Mathematically, the change in MR signal ΔS due to a change in the effective transverse relaxation rate ΔR_2^* can be approximated by:

$$\frac{\Delta S}{S} \approx e^{-TE \cdot \Delta R_2^*} - 1 \approx -TE \cdot \Delta R_2^*, \tag{3.24}$$

where S is the baseline signal intensity, TE is the echo time, and ΔR_2^* represents the change in $1/T_2^*$. The negative sign indicates that an increase in ΔR_2^* (more dHb) leads to a signal decrease. However, during activation, ΔR_2^* decreases due to reduced dHb, leading to a signal [18].

The BOLD signal is inherently complex, influenced by multiple physiological processes, including the cerebral metabolic rate of oxygen consumption ($CMRO_2$), cerebral blood volume (CBV), and cerebral blood flow (CBF) [18]. Accurately modeling the BOLD signal requires consideration of these factors and their interplay.

3.2.2 Hemodynamic Response Function (HRF)

The relationship between neuronal activation and the BOLD signal is characterized by the **Hemodynamic Response Function** (HRF), which describes how the BOLD signal evolves over time following a brief neural stimulus [18, 17]. The HRF in fMRI because allows prediction of the expected BOLD signal resulting from a given pattern of neuronal activity.

The typical HRF exhibits a characteristic shape with several distinct phases (Figure 3.5). Immediately following neuronal activation, there may be a small initial dip in the BOLD signal, thought to reflect the rapid increase in oxygen consumption before the vascular response. This is followed by the main positive peak, occurring around 4 to 8 seconds after stimulus onset, reflecting the influx of oxygenated blood that exceeds metabolic demands. After the peak, the signal returns to baseline but often undershoots, resulting in a post-stimulus undershoot that can last several seconds. This undershoot may be due to delayed normalization of cerebral blood volume or continued elevated metabolic rates.

Mathematically, the HRF can be modeled using a combination of gamma functions, capturing the delay, rise, and fall of the BOLD response:

$$h(t) = A_1 \left(\frac{t - d_1}{b_1} \right)^{a_1} e^{-(t-d_1)/b_1} - A_2 \left(\frac{t - d_2}{b_2} \right)^{a_2} e^{-(t-d_2)/b_2}, \tag{3.25}$$

where A_i are amplitude scaling factors, a_i are shape parameters, b_i are time constants controlling the width, and d_i are delays for the peak and undershoot components, respectively [17]. This model allows flexibility in fitting the observed BOLD response across different brain regions and subjects.

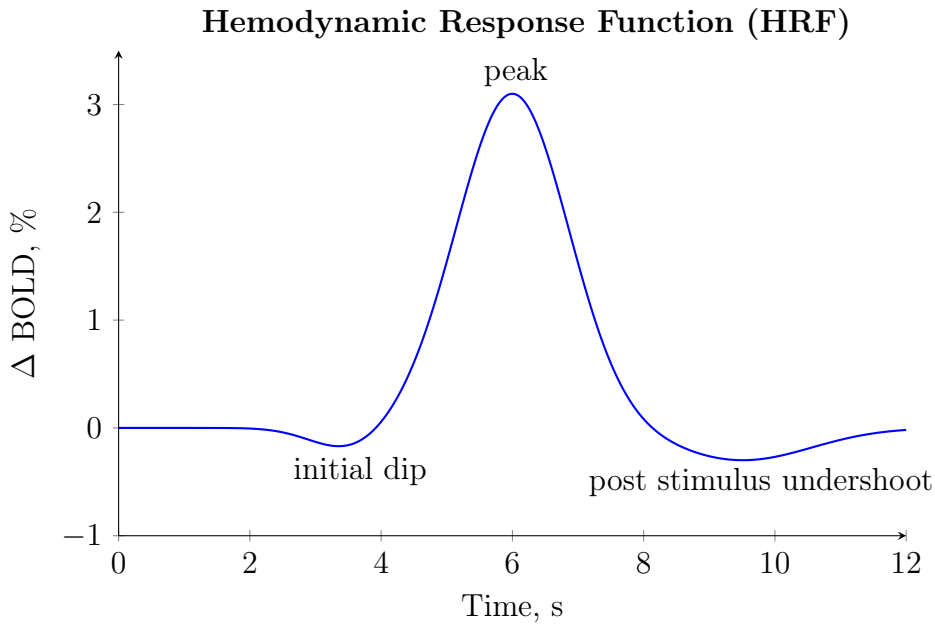

Figure 3.5: **Hemodynamic Response Function (HRF).** The plot illustrates the BOLD signal evolution after a brief neural stimulus. Key phases include an initial dip due to increased oxygen consumption, a positive peak (4–8 seconds) reflecting an influx of oxygenated blood, and a post-stimulus undershoot related to delayed cerebral blood volume adjustments.

3.2.3 fMRI Data Analysis

Analyzing fMRI data involves several complex steps aimed at extracting meaningful information about brain function from the raw MR signals [18]. The process begins with **preprocessing**, which includes correcting for differences in slice acquisition timing, realigning images to compensate for subject motion, normalizing brain images to a standard anatomical

space, smoothing to enhance signal-to-noise ratio, and filtering to remove physiological noise and drifts.

After preprocessing, **statistical analysis** is performed to identify brain regions where the BOLD signal correlates with the experimental design or task. The most commonly used framework for this analysis is the **General Linear Model** (GLM), which models the observed BOLD time series as a linear combination of predictors (regressors) and noise:

$$\mathbf{Y} = \mathbf{X}\boldsymbol{\beta} + \boldsymbol{\epsilon}, \tag{3.26}$$

where $\mathbf{Y}$ is the vector of observed fMRI signals over time, $\mathbf{X}$ is the design matrix containing convolved regressors (e.g., the HRF convolved with stimulus timing), $\boldsymbol{\beta}$ are the parameters to be estimated (reflecting the magnitude of activation), and $\boldsymbol{\epsilon}$ is the residual error term [18].

Parameter estimation is typically achieved using ordinary least squares, yielding estimates $\hat{\boldsymbol{\beta}}$ that minimize the sum of squared errors. Hypothesis testing involves specifying contrast vectors to test specific effects of interest, and statistical significance is assessed using t-tests or F-tests. To account for the multiple comparisons inherent in voxel-wise analysis, corrections such as the Bonferroni correction or False Discovery Rate (FDR) are applied to control the family-wise error rate.

3.2.4 Resting-State fMRI (rsfMRI)

Resting-State fMRI focuses on spontaneous fluctuations in the BOLD signal that occur in the absence of explicit tasks or stimuli [18, 17, 19]. These low-frequency fluctuations (less than 0.1 Hz) are thought to reflect the brain's intrinsic functional architecture, revealing networks of regions that are functionally connected [18]. Unlike task-based fMRI, rsfMRI examines the temporal coherence of BOLD signals between different brain areas during rest.

Functional connectivity in rsfMRI is typically assessed by computing the temporal cor-

relation between the BOLD time series of different regions [17, 20, 21, 22]. For example, the Pearson correlation coefficient between time series $x_i(t)$ and $x_j(t)$ from regions i and j is given by:

$$r_{ij} = \frac{\sum_{t=1}^{T}(x_i(t) - \bar{x}_i)(x_j(t) - \bar{x}_j)}{\sqrt{\sum_{t=1}^{T}(x_i(t) - \bar{x}_i)^2}\sqrt{\sum_{t=1}^{T}(x_j(t) - \bar{x}_j)^2}}, \tag{3.27}$$

where $\bar{x}_i$ and $\bar{x}_j$ are the mean signals over time for regions i and j, respectively. High correlation coefficients suggest functional connectivity, implying that these regions are part of the same resting-state network (RSN).

Independent Component Analysis

One common approach to identify RSNs is **Independent Component Analysis** (ICA), a powerful data-driven method used to decompose the fMRI data into statistically independent spatial components [18]. ICA is especially valuable in rsfMRI analysis due to its ability to identify brain networks without any prior knowledge or model of their spatial locations, making it a flexible method for discovering novel functional networks.

In ICA, the observed rsfMRI data matrix $\mathbf{X}$, which typically has dimensions $V \times T$ (where V represents the number of voxels and T represents the number of time points), is assumed to be a linear mixture of unknown independent components:

$$\mathbf{X} = \mathbf{AS}, \tag{3.28}$$

where:

- $\mathbf{A}$ is the **mixing matrix**, of size $T \times N$, containing the time courses associated with each independent component.
- $\mathbf{S}$ is a matrix of size $N \times V$, containing the **independent components**, which are

spatial maps indicating the areas of the brain with correlated BOLD signal fluctuations.

The goal of ICA is to determine both $\mathbf{A}$ and $\mathbf{S}$ based solely on the observations in $\mathbf{X}$. This is done under the assumption that the components in $\mathbf{S}$ are statistically independent from each other. Independence is typically measured by non-Gaussianity, with the assumption that the source signals are non-Gaussian and independent.

To achieve this, iterative algorithms, such as FastICA, are often employed. FastICA is an efficient method for finding independent components by maximizing a measure of non-Gaussianity, such as negentropy, which can be expressed as:

$$J(y) = H(y_{\text{Gaussian}}) - H(y), \tag{3.29}$$

where $H(y)$ represents the entropy of the random variable y, and $H(y_{\text{Gaussian}})$ is the entropy of a Gaussian variable with the same variance as y. By maximizing negentropy, ICA effectively finds a representation of the data where the components are maximally independent and non-Gaussian.

Another approach used by ICA algorithms involves minimizing the mutual information $I(y_1, y_2, \ldots, y_N)$ of the components, where mutual information is defined as:

$$I(y_1, y_2, \ldots, y_N) = \sum_{i=1}^{N} H(y_i) - H(\mathbf{y}), \tag{3.30}$$

with $H(\mathbf{y})$ representing the joint entropy of all components. In practical terms, minimizing mutual information implies that the joint distribution of the components becomes as close as possible to the product of their marginal distributions, achieving statistical independence.

Once ICA decomposes the data into its constituent components, each independent component represents a distinct RSN, which includes areas of the brain that exhibit temporally correlated activity. Examples of RSNs that are commonly identified using ICA include:

- The **Default Mode Network (DMN)**, which is active during rest and involved in

processes such as mind-wandering and self-referential thought.

- The **Sensorimotor Network**, which encompasses regions involved in somatosensory and motor functions, including the primary motor cortex and somatosensory cortex.
- The **Visual Network**, located primarily in the occipital cortex, responsible for visual processing.
- The **Attentional Networks**, such as the dorsal attention network, involved in voluntary attention control, and the ventral attention network, associated with detecting salient stimuli.

The output from ICA (Figure 3.6) consists of a set of spatial maps (**S**) and their associated time courses (**A**). The spatial maps highlight voxels whose activity contributes to a specific RSN, while the corresponding time courses reflect the temporal fluctuation of activity within those networks.

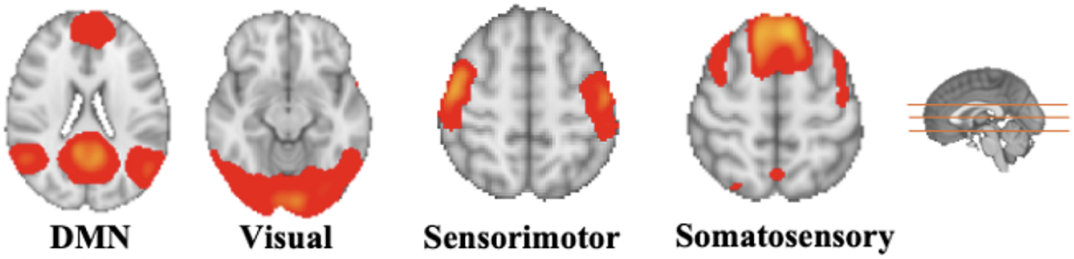

Figure 3.6: **Example ICA Spatial Maps.** The figure shows example spatial maps derived from ICA applied to resting-state fMRI data. Each spatial map represents a specific Resting-State Network (RSN), highlighting regions of the brain where voxel activity is temporally correlated, contributing to distinct functional networks. **Left to Right**: The **Default Mode Network (DMN)**, which is involved in introspective tasks and deactivates during externally-focused activities; the **Visual Network**, which is primarily responsible for visual processing; the **Sensorimotor Network**, involved in coordinating motor activities and processing somatosensory information; and the **Somatosensory Network**, related to sensory information processing. Each RSN is characterized by specific patterns of connectivity, captured through ICA decomposition, where the red regions indicate areas of higher activity correlation within that network. The figure also includes a sagittal view to demonstrate the approximate slices used in generating these spatial maps.

The advantages of ICA are not only its ability to identify functionally coherent networks but also its capacity to separate artifacts from true neural signals. For instance, ICA can identify and isolate components related to physiological noise (e.g., cardiac or respiratory fluctuations) or head motion, thereby improving the quality of rsfMRI data analysis. This denoising capability makes ICA an essential tool in preprocessing pipelines for resting-state rsfMRI.

Another mathematical perspective on ICA is its ability to solve the "blind source separation" problem, where the task is to recover the original independent sources from their mixtures without knowing the nature of the mixing process. This aspect is particularly powerful in rsfMRI data analysis, as the sources (neural networks) are not directly measurable, and only their mixed signals (observed voxel intensities) are available.

ICA provides a robust and flexible methodology for identifying RSNs by maximizing

statistical independence between components, allowing for unbiased identification of brain networks. This independence-based uncovers consistent functional networks across individuals, populations, and even species, thereby playing a central role in understanding the intrinsic connectivity and functional architecture of the human brain.

3.2.5 Neurological Underpinnings of fMRI and rsfMRI

The BOLD signal arises from a complex interplay between neuronal activity, metabolism, and hemodynamics [15, 17, 18]. Understanding the neurophysiological basis of the BOLD signal is essential for accurate interpretation of fMRI data.

Neurovascular Coupling and the Neurovascular Unit

Neurovascular coupling refers to the relationship between neuronal activity and subsequent changes in cerebral blood flow [18, 17, 23, 24]. This process is mediated by the **neurovascular unit** (Figure 3.7), a functional ensemble comprising neurons, astrocytes, vascular endothelial cells, pericytes, and smooth muscle cells [24, 25]. The neurovascular unit orchestrates the regulation of cerebral blood flow in response to neuronal activity.

When neurons become active, they release neurotransmitters such as glutamate, which propagate neural signals and activate receptors on adjacent astrocytes [23]. Astrocytes respond by increasing intracellular calcium levels, leading to the release of vasoactive substances like prostaglandins and nitric oxide (NO) [23]. These substances act on the smooth muscle cells of arterioles and capillaries, causing vasodilation and increasing blood flow to the active region.

Pericytes, located along capillaries, also play a role in regulating blood flow at the microvascular level. Endothelial cells contribute by releasing factors that influence vessel diameter and permeability [23, 26, 27]. The integrated response of the neurovascular unit ensures a timely and localized increase in blood flow, matching the metabolic demands of active

neurons.

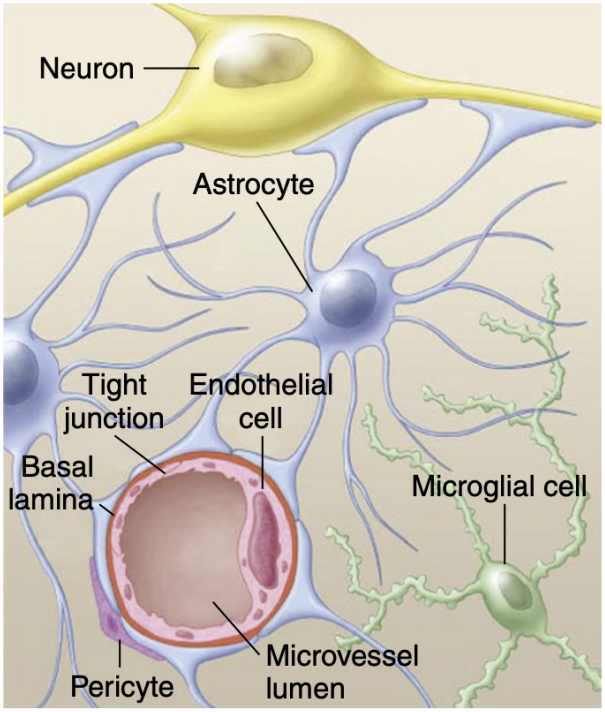

Figure 3.7: Illustration of the neurovascular unit, highlighting the interactions between neurons, astrocytes, endothelial cells, pericytes, and smooth muscle cells in regulating cerebral blood flow. The illustration is adapted directly from Zoppo et al [28].

Disruption in the function of the the neurovascular unit can affect neurovascular coupling and, consequently, the BOLD signal [17, 2]. In pathological conditions such as stroke, neurodegenerative diseases, or aging, alterations in neurovascular unit components can lead to impaired blood flow regulation.

Neuroenergetics

Neuronal activity increases the demand for ATP, which is primarily produced through oxidative metabolism of glucose [23]. The mismatch between oxygen delivery (due to increased CBF) and oxygen consumption leads to changes in the Oxygen Extraction Fraction (OEF), defined as:

$$\text{OEF} = \frac{\text{CMRO}_2}{\text{CBF} \times [\text{O}_2]}, \tag{3.31}$$

where CMRO_2 is the cerebral metabolic rate of oxygen consumption, CBF is the cerebral blood flow, and $[\text{O}_2]$ is the arterial oxygen concentration. Changes in OEF contribute to the dynamics of the BOLD signal [18, 29, 30].

Spontaneous Neural Activity

Resting-state BOLD fluctuations are thought to reflect spontaneous neuronal activity that is organized into coherent patterns rather than random noise [18, 17]. These intrinsic activities may play roles in maintaining synaptic connections, consolidating memories, and preparing the brain for responsive action. The consistent observation of RSNs across individuals suggests that these networks are fundamental to brain function.

3.2.6 Mathematical Models of Neurovascular Coupling

To quantitatively relate neuronal activity to the observed BOLD signal, biophysical models have been developed. One such model is the **Balloon Model** (Figure 3.8), which describes the dynamics of blood flow, volume, and deoxyhemoglobin content in response to neuronal activation [31, 18].

The Balloon Model comprises differential equations governing the changes in normalized venous blood volume $v(t)$ and deoxyhemoglobin content $q(t)$:

$$\frac{dv(t)}{dt} = \frac{1}{\tau_0}[f(t) - v(t)^{1/\alpha}], \tag{3.32}$$

$$\frac{dq(t)}{dt} = \frac{1}{\tau_0}\left[\frac{f(t)\left(1-(1-E_0)^{1/f(t)}\right)}{E_0} - \frac{q(t)}{v(t)}v(t)^{1/\alpha}\right], \tag{3.33}$$

where $f(t)$ is the normalized cerebral blood flow, τ_0 is the mean transit time of blood through the venous compartment, α is Grubb's exponent relating blood volume and flow, and E_0 is the resting oxygen extraction fraction [17, 18].

The BOLD signal change ΔS can then be modeled as a function of $v(t)$ and $q(t)$:

$$\frac{\Delta S}{S_0} = V_0 \left[k_1(1 - q(t)) + k_2 \left(1 - \frac{q(t)}{v(t)} \right) + k_3(1 - v(t)) \right], \tag{3.34}$$

where V_0 is the resting blood volume fraction, S_0 is the baseline signal, and k_1, k_2, k_3 are constants dependent on the magnetic field strength and imaging parameters.

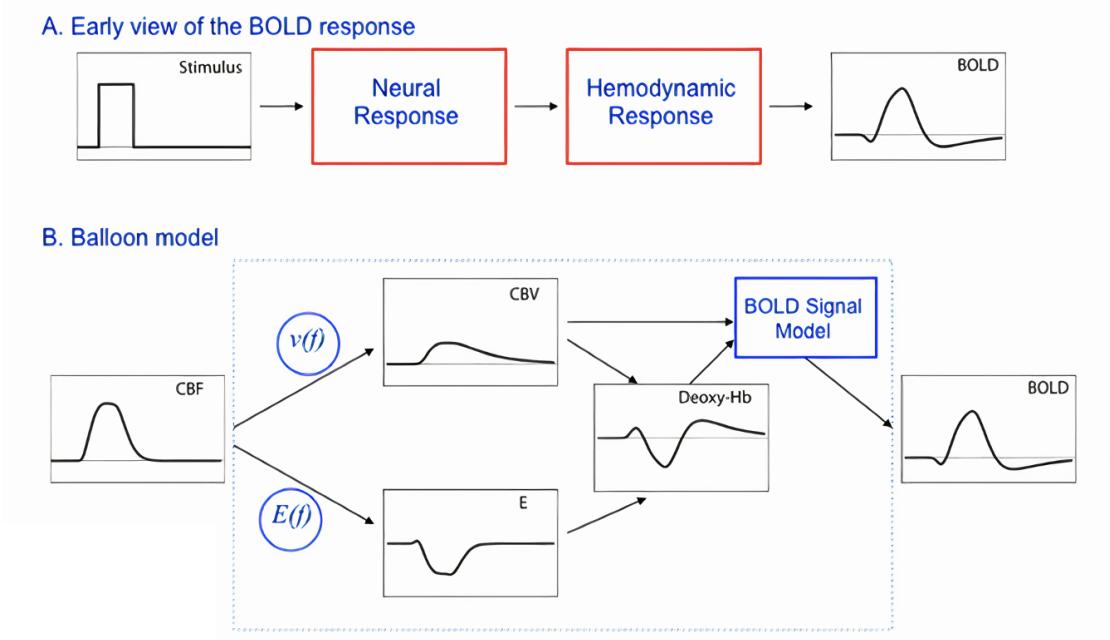

Figure 3.8: **Balloon Model of the BOLD Response.** (A) An early view of the BOLD response represents the chain of events from stimulus onset, through neural activation and hemodynamic response, to the resultant BOLD signal. This approach simplifies the understanding of how vascular dynamics influence the BOLD signal. (B) The Balloon model further details the relationship between cerebral blood flow (CBF), cerebral blood volume (CBV), and deoxyhemoglobin content. This model accounts for the passive expansion of venous blood volume in response to changes in CBF and helps to understand how these changes produce the BOLD signal during and after neuronal activation. The schematic emphasizes the physiological basis of the BOLD signal, as well as the temporal dynamics of its components. Adapted from Buxton (2012) [31].

Another approach is **Dynamic Causal Modeling** (DCM), which integrates neuronal and hemodynamic models to infer hidden neuronal states from the BOLD signal [18, 17, 32]. In DCM, the neuronal state vector $\mathbf{z}(t)$ evolves according to:

$$\frac{d\mathbf{z}(t)}{dt} = \mathbf{A}\mathbf{z}(t) + \mathbf{C}\mathbf{u}(t), \tag{3.35}$$

where $\mathbf{A}$ represents intrinsic connections between brain regions, $\mathbf{C}$ represents the influence of external inputs $\mathbf{u}(t)$, and the hemodynamic model links $\mathbf{z}(t)$ to the predicted BOLD response [18].

3.2.7 Challenges and Considerations in fMRI and rsfMRI

Interpreting fMRI data requires careful consideration of several factors that can influence the BOLD signal. Physiological noise from cardiac and respiratory cycles can introduce artifacts, which can be mitigated by recording physiological signals during scanning and applying retrospective correction algorithms [32, 18]. Additionally, scanner drift and thermal noise necessitate appropriate temporal filtering and preprocessing steps.

Spatial and temporal resolution are critical considerations. Higher spatial resolution improves localization of activation but may reduce the signal-to-noise ratio and increase scan times. Temporal resolution affects the ability to detect rapid changes in neural activity and the accurate estimation of functional connectivity.

Reproducibility and reliability are paramount, especially for clinical applications and longitudinal studies. Ensuring standardized imaging protocols, consistent preprocessing pipelines, and rigorous statistical analyses enhances the validity of findings.

3.2.8 Future Directions and Advanced Techniques

Advancements in fMRI technology and analysis methods continue to expand its capabilities. Multimodal imaging approaches, combining fMRI with electroencephalography (EEG) or magnetoencephalography (MEG), offer complementary spatial and temporal resolution, providing a more comprehensive understanding of brain function [2, 33, 34].

High-field MRI scanners (7 Tesla and above) provide increased signal-to-noise ratio and enhanced sensitivity to susceptibility effects, allowing for finer spatial resolution and improved detection of subtle functional changes [34]. However, they also present challenges such as increased susceptibility artifacts and safety considerations related to higher magnetic fields.

Machine learning and artificial intelligence techniques are increasingly applied to fMRI data for pattern recognition, classification, and predictive modeling [34]. These approaches can handle high-dimensional data and uncover complex patterns that may not be apparent through traditional analysis methods.

3.2.9 Summary

Functional MRI and resting-state fMRI have revolutionized our ability to study the human brain in vivo. By leveraging the BOLD contrast mechanism and understanding the role of the neurovascular unit in neurovascular coupling, these techniques provide insights into the neural correlates of cognitive processes, functional connectivity, and brain organization. A comprehensive grasp of the physiological and mathematical foundations of the BOLD signal is essential for designing experiments, analyzing data, and interpreting results. As technology advances and computational methods evolve, fMRI will continue to be a vital tool in neuroscience research and clinical applications such as in stroke management.

3.3 Pathophysiology of Ischemic Stroke

Acute ischemic stroke is a devastating neurological event resulting from the sudden interruption of blood flow to a region of the brain [1, 35]. This interruption deprives neurons and glial cells of essential nutrients and oxygen, leading to a complex cascade of cellular and molecular events that culminate in neuronal injury and death. Understanding the intricate pathophysiological mechanisms underlying ischemic stroke is crucial for developing effective therapeutic strategies and improving patient outcomes.

3.3.1 Cellular and Molecular Mechanisms

The onset of ischemia initiates a series of interconnected pathological processes (Figure 3.9), each contributing to the progression of brain injury. The primary event is the reduction or cessation of cerebral blood flow due to arterial occlusion, typically caused by a thrombus or embolus [36, 37]. This leads to an immediate energy crisis within affected brain regions.

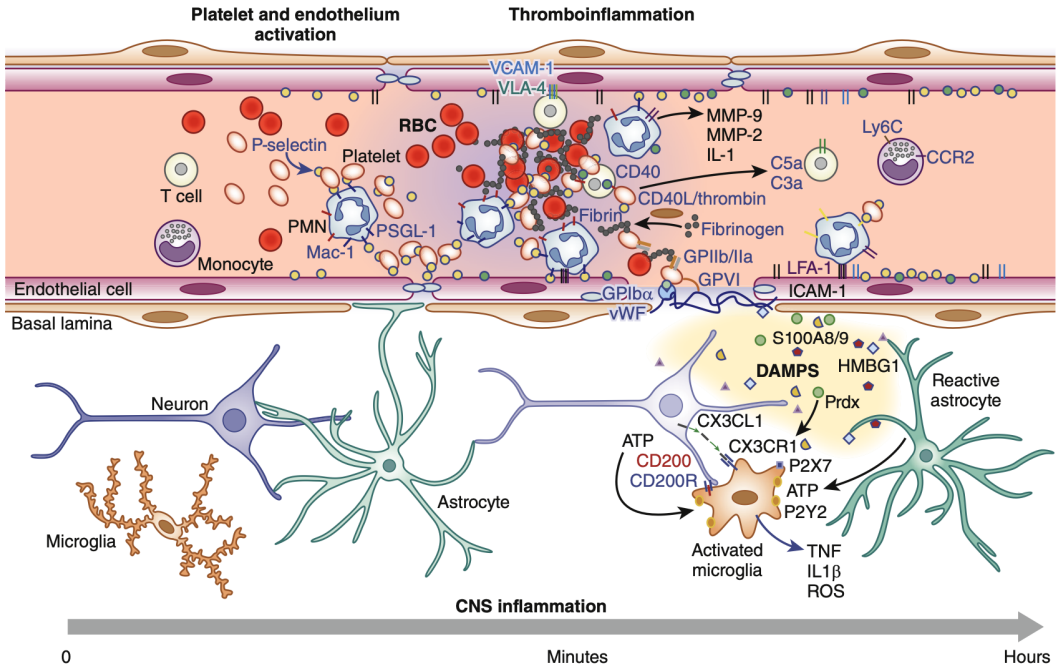

Figure 3.9: **Neurovascular Interactions During Ischemic Stroke.** The **top portion** depicts platelet and endothelium activation, contributing to thromboinflammation through the release of mediators like MMP-9, MMP-2, and IL-1, and through leukocyte adhesion via molecules such as P-selectin, ICAM-1, and VCAM-1. Activated platelets and immune cells adhere to the endothelium, releasing pro-inflammatory factors and promoting thrombus formation. The **bottom portion** illustrates the **CNS inflammatory response**, including microglia, astrocytes, and neurons. Microglia release TNF, IL-1β, and ROS in response to DAMPS and ATP, contributing to neuronal damage, while reactive astrocytes exacerbate inflammation through cytokine production. These processes underlie the progression of stroke-induced injury and highlight key targets for therapeutic intervention. Adapted from Garcia-Bonilla et al [38].

Energy Failure and Ionic Imbalance

Neurons are highly dependent on aerobic metabolism for ATP production. The abrupt loss of oxygen and glucose supply halts oxidative phosphorylation within mitochondria, rapidly depleting ATP stores [36]. The energy failure impairs the function of ATP-dependent ion pumps, particularly the Na^+/K^+-ATPase, which is essential for maintaining ionic gradients across the neuronal membrane [1, 36].

As the Na^+/K^+-ATPase pump fails, there is an accumulation of intracellular sodium

(Na^+) and calcium (Ca^{2+}) ions, while potassium (K^+) ions leak out of the cell. This ionic imbalance leads to the depolarization of neurons and the opening of voltage-gated calcium channels, further increasing intracellular Ca^{2+} levels [36, 39, 40]. The disrupted ionic homeostasis sets the stage for excitotoxicity and initiates detrimental enzymatic processes.

Excitotoxicity

Depolarized neurons release excessive amounts of excitatory neurotransmitters, predominantly glutamate, into the synaptic cleft. The elevated extracellular glutamate overstimulates ionotropic glutamate receptors, such as NMDA and AMPA receptors, on postsynaptic neurons. Activation of these receptors facilitates a massive influx of Ca^{2+} and Na^+ ions into the cell [40, 28].

The surge in intracellular Ca^{2+} concentration activates various calcium-dependent enzymes, including proteases like calpains, phospholipases, and endonucleases. Calpains degrade cytoskeletal proteins, compromising neuronal structural integrity [40]. Phospholipases break down membrane phospholipids, leading to the generation of arachidonic acid and subsequent production of pro-inflammatory eicosanoids. Endonucleases cause DNA fragmentation, which can trigger apoptotic pathways.

Oxidative and Nitrosative Stress

The mitochondrial dysfunction resulting from energy failure and calcium overload leads to the generation of reactive oxygen species (ROS). Impaired electron transport chain function causes leakage of electrons, which react with molecular oxygen to form superoxide radicals (O_2^-). Superoxide can be converted to hydrogen peroxide (H_2O_2) by superoxide dismutase (SOD), and further to hydroxyl radicals ($OH\cdot$) via the Fenton reaction in the presence of iron [40]. These ROS are highly reactive and can damage lipids, proteins, and DNA.

Concurrently, nitric oxide synthase (NOS) enzymes produce nitric oxide (NO). Under

ischemic conditions, inducible NOS (iNOS) and neuronal NOS (nNOS) become overactive, leading to excessive NO production [40, 28]. NO reacts with superoxide to form peroxynitrite ($ONOO^-$), a potent reactive nitrogen species (RNS) that exacerbates cellular damage through nitration of tyrosine residues in proteins and lipid peroxidation.

Inflammatory Response

The inflammatory response (Figures 3.9 & 3.10) is a critical component of ischemic stroke pathophysiology. Within minutes of ischemia onset, resident microglia in the brain are activated [35]. These cells transition from a resting to an activated state, adopting amoeboid morphology and producing pro-inflammatory cytokines such as TNF-α, IL-1β, and IL-6. Astrocytes also become reactive, contributing to the release of inflammatory mediators and upregulation of adhesion molecules [41, 40].

These cytokines promote the expression of adhesion molecules like ICAM-1 and VCAM-1 on endothelial cells of the cerebral vasculature [40]. This facilitates the recruitment and transmigration of peripheral immune cells, including neutrophils, monocytes, and lymphocytes, into the brain parenchyma [40, 28].

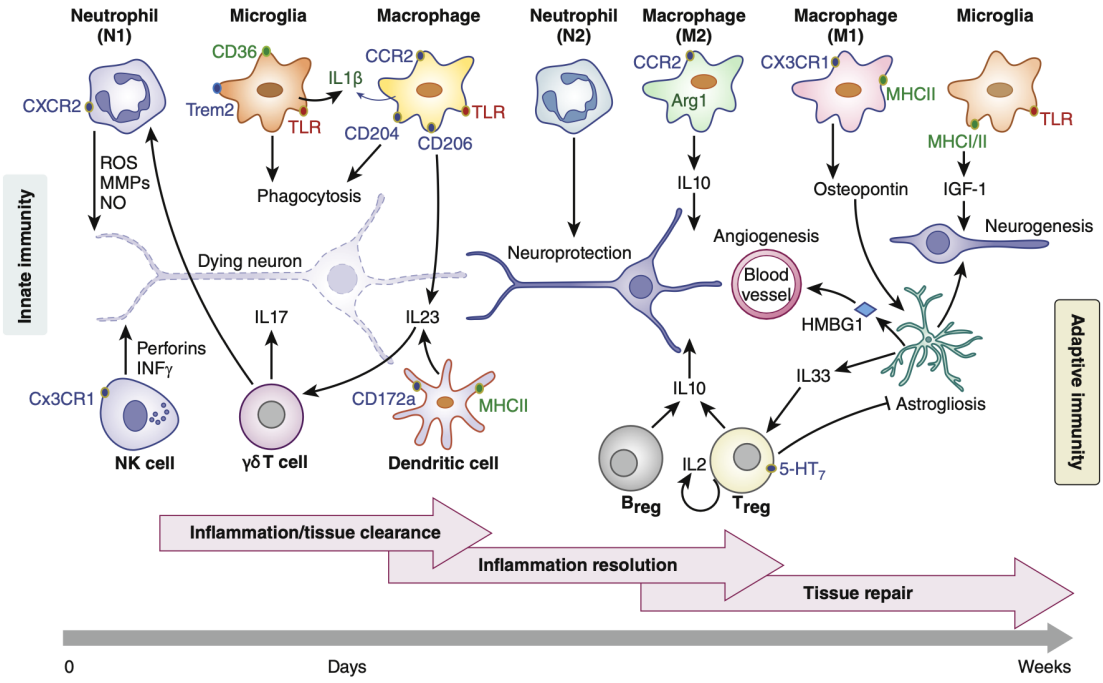

Figure 3.10: **Temporal Progression of the Inflammatory Response in Ischemic Stroke.** The coordinated innate and adaptive immune responses following an ischemic stroke are shown, detailing key cellular players and their interactions over time. **Innate Immunity (Left)**: Neutrophils (N1) are among the first responders, releasing reactive oxygen species (ROS), matrix metalloproteinases (MMPs), and nitric oxide (NO) to clear damaged cells and debris. Microglia and macrophages are activated, with M1 macrophages contributing to inflammation, and M2 macrophages promoting tissue repair and angiogenesis. Microglia phagocytose dying neurons and interact with macrophages and other immune cells. **Adaptive Immunity (Right)**: As inflammation evolves, the adaptive immune system becomes involved, with regulatory T cells (Tregs) releasing anti-inflammatory cytokines like IL-10 to resolve inflammation and support tissue repair. The progression of inflammation, from acute tissue clearance by innate cells to adaptive immune-mediated resolution and tissue repair, spans from the acute phase (days) to the chronic phase (weeks). Adapted from Garcia-Bonilla et al [38].

Neutrophils are among the first infiltrating cells and contribute to secondary injury by releasing proteases, ROS, and pro-inflammatory cytokines. Monocytes differentiate into macrophages within the brain and can adopt either pro-inflammatory (M1) or anti-inflammatory (M2) phenotypes, influencing the balance between further injury and repair processes.

Blood-Brain Barrier Disruption

The blood-brain barrier (BBB) is a selective barrier formed by endothelial cells, tight junction proteins, astrocyte end-feet, and pericytes [40]. Ischemia leads to the disruption of the BBB through several mechanisms. Inflammatory cytokines and oxidative stress upregulate matrix metalloproteinases (MMPs), particularly MMP-2 and MMP-9 [40]. MMPs degrade extracellular matrix components and tight junction proteins like occludin and claudins, increasing BBB permeability.

The compromised BBB allows plasma proteins, such as fibrinogen and albumin, and immune cells to enter the brain parenchyma. This extravasation contributes to vasogenic edema, increasing intracranial pressure and potentially leading to herniation [40, 41, 28]. Additionally, the influx of peripheral immune cells amplifies the inflammatory response within the brain.

Cell Death Pathways

Cell death in ischemic stroke occurs through a continuum of mechanisms (Figure 3.11), including necrosis, apoptosis, autophagy, and necroptosis. The mode of cell death is influenced by the severity and duration of ischemia and varies across different brain regions [28, 40, 42, 43].

In the ischemic core, where blood flow reduction is most severe, neurons rapidly undergo necrosis due to profound energy failure. Necrotic cells exhibit swelling, loss of membrane integrity, and uncontrolled release of intracellular contents, which can provoke further inflammation.

In the penumbra, neurons experience less severe ischemia and may die through apoptosis, a regulated form of cell death [40]. Apoptosis involves caspase activation, chromatin condensation, DNA fragmentation, and the formation of apoptotic bodies, which are phagocytosed

without triggering inflammation.

Autophagy, a process of cellular self-digestion, is upregulated in response to stress and can have dual roles. While moderate autophagy may promote cell survival by removing damaged organelles, excessive autophagy can lead to autophagic cell death.

Necroptosis is a programmed form of necrosis mediated by receptor-interacting protein kinases RIPK1 and RIPK3, and the mixed lineage kinase domain-like protein (MLKL) [40, 38]. Necroptosis shares features with both necrosis and apoptosis and contributes to inflammation due to the release of cellular contents.

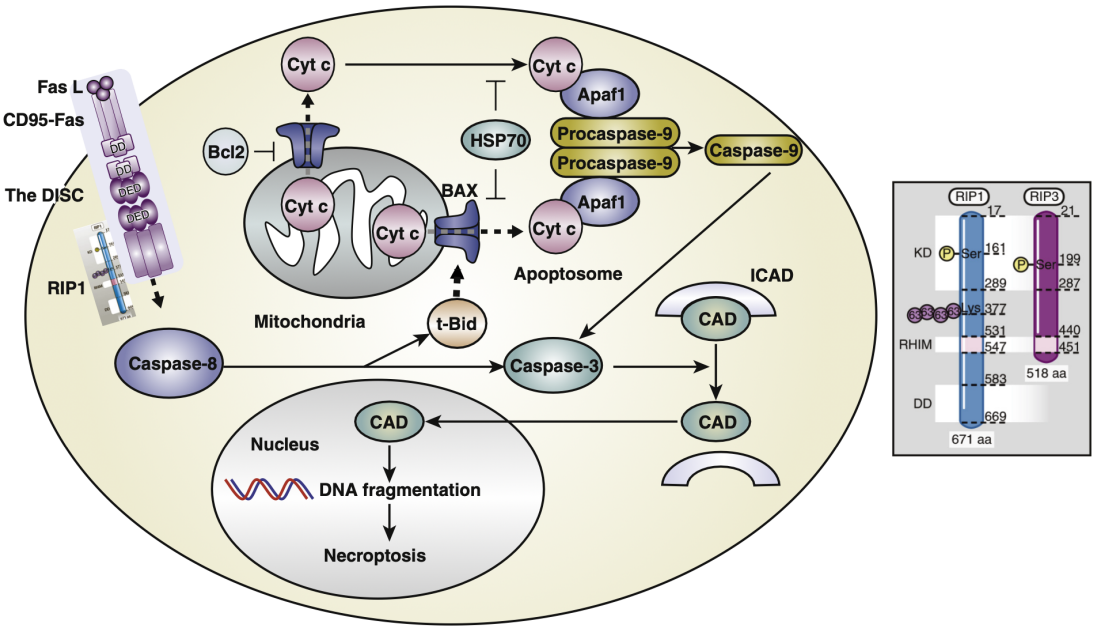

Figure 3.11: **Molecular Mechanisms of Cell Death in Ischemic Stroke.** Key molecular players involved in different cell death pathways, including necrosis, apoptosis, and necroptosis, are illustrated. The **extrinsic apoptotic pathway** is initiated by binding of Fas ligand (FasL) to the CD95-Fas receptor, forming the death-inducing signaling complex (DISC) and leading to caspase-8 activation. Caspase-8 subsequently cleaves and activates downstream caspases such as caspase-3, resulting in DNA fragmentation by CAD (Caspase-Activated DNase). The **intrinsic apoptotic pathway** is characterized by mitochondrial release of cytochrome c (Cyt c), which binds Apaf-1, forming the apoptosome that activates caspase-9 and downstream caspase-3. Necroptosis, mediated by receptor-interacting proteins (RIP1 and RIP3), is also illustrated, emphasizing its interplay with apoptosis and its contribution to inflammation through necrotic release of cellular contents. The crosstalk between these pathways highlights the complexity of cell death mechanisms in ischemic conditions. Adapted from Yang et al [40].

3.3.2 Temporal Dynamics of Ischemic Injury

The progression of ischemic injury unfolds over time (Figures 3.9 & 3.10), with distinct phases characterized by specific pathophysiological processes [35, 44, 28, 37, 45]. Understanding these temporal dynamics is essential for identifying therapeutic windows and tailoring interventions.

Hyperacute Phase (Minutes to Hours)

In the hyperacute phase, immediate energy failure leads to rapid neuronal depolarization and the onset of excitotoxicity. The accumulation of extracellular glutamate and calcium overload initiates destructive enzymatic cascades. Early oxidative and nitrosative stress exacerbate mitochondrial dysfunction and energy deficits.

Microglial activation begins within minutes, and the release of pro-inflammatory cytokines sets the foundation for the inflammatory response. BBB disruption starts due to the activation of MMPs and degradation of tight junction proteins.

Acute Phase (Hours to Days)

The acute phase is marked by the amplification of inflammatory responses. Peripheral immune cells infiltrate the brain, with neutrophils arriving first. These cells release enzymes and ROS, contributing to secondary injury and BBB disruption. Vasogenic edema peaks during this phase, increasing intracranial pressure and risking herniation.

Apoptotic cell death becomes prominent in the penumbra. Therapeutic interventions during this phase aim to reduce inflammation, protect the BBB, and prevent further neuronal loss.

Subacute Phase (Days to Weeks)

In the subacute phase, there is a transition from injury to repair. Inflammation begins to subside as anti-inflammatory cytokines like IL-10 and TGF-β are produced [41, 46]. Macrophages shift towards an M2 phenotype, promoting tissue repair and angiogenesis.

Neurogenesis and angiogenesis are stimulated by growth factors such as VEGF, BDNF, and NGF [40]. Endothelial cells proliferate, forming new blood vessels that restore perfusion. Neural progenitor cells migrate towards the ischemic area, potentially contributing to neuronal replacement.

Astrocytes proliferate and form a glial scar around the infarcted tissue. While this scar contains the injury and prevents the spread of damage, it can also inhibit axonal regeneration due to the secretion of inhibitory molecules.

Chronic Phase (Weeks to Months)

The chronic phase involves remodeling and plasticity as the brain attempts to recover function. Surviving neurons undergo synaptic plasticity, forming new connections to compensate for lost pathways. Dendritic sprouting and changes in neurotransmitter receptor expression facilitate neural network reorganization.

Persistent low-grade inflammation may continue, potentially impacting long-term recovery. Remote effects, such as diaschisis, can occur where regions distant from the infarct exhibit altered function due to disrupted connectivity.

Rehabilitation efforts are critical during this phase to enhance neuroplasticity. Therapeutic interventions focus on facilitating functional recovery through physical therapy, occupational therapy, and cognitive rehabilitation.

3.3.3 Collateral Circulation and Penumbral Salvage

The extent of ischemic injury is influenced by the adequacy of collateral circulation. Collateral vessels provide alternative routes for blood flow when primary arteries are occluded, supplying the penumbral regions with oxygen and nutrients.

Robust collateral circulation can prolong the survival of at-risk tissue, extending the therapeutic window for interventions such as thrombolysis and mechanical thrombectomy. Factors affecting collateral flow include individual vascular anatomy, blood pressure, and systemic vascular health.

Efforts to enhance collateral flow, such as pharmacological vasodilation or induced hypertension, are under investigation. Imaging techniques like perfusion MRI and CT angiography help assess collateral status and guide treatment decisions.

3.3.4 Molecular Targets for Therapeutic Intervention

Advances in understanding the molecular mechanisms of ischemic stroke have identified numerous therapeutic targets aimed at mitigating damage and promoting recovery.

Modulating Excitotoxicity

Therapies targeting excitotoxicity focus on reducing glutamate release or blocking glutamate receptors [37, 46]. While NMDA receptor antagonists showed promise in preclinical studies, clinical trials have been limited by side effects and lack of efficacy, highlighting the challenge of targeting excitatory neurotransmission without disrupting normal brain function.

Reducing Oxidative Stress

Antioxidant therapies aim to neutralize ROS and protect cellular components from oxidative damage. Agents like edaravone, a free radical scavenger, have demonstrated efficacy

in reducing infarct size and improving outcomes in some patient populations. Enhancing endogenous antioxidant defenses through upregulation of enzymes like SOD and catalase is another strategy under exploration.

Anti-inflammatory Approaches

Modulating the inflammatory response offers potential for limiting secondary injury. Strategies include inhibiting pro-inflammatory cytokines, blocking leukocyte adhesion and infiltration, and promoting anti-inflammatory mediators. Selective inhibition of MMPs to preserve BBB integrity is also a therapeutic avenue. Balancing immune modulation to avoid impairing host defenses is a critical consideration.

Promoting Neuroprotection and Repair

Neuroprotective agents aim to inhibit apoptotic pathways, support mitochondrial function, and enhance cell survival signaling. Growth factors such as erythropoietin and granulocyte colony-stimulating factor have neuroprotective properties and may promote neurogenesis and angiogenesis.

Cell-based therapies using stem cells or progenitor cells offer potential for replacing damaged neurons and supporting repair processes. These approaches are in early stages of research, with challenges including cell delivery, survival, and integration into existing neural networks.

Enhancing Neuroplasticity

Rehabilitation strategies that harness neuroplasticity are essential for functional recovery [41]. Pharmacological agents that modulate neurotransmitter systems, such as selective serotonin reuptake inhibitors (SSRIs), may enhance plasticity and improve outcomes when combined with rehabilitation therapies.

Non-invasive brain stimulation techniques, like transcranial magnetic stimulation (TMS) and transcranial direct current stimulation (tDCS), are being investigated for their ability to modulate cortical excitability and promote reorganization of neural circuits [37, 44].

3.3.5 Summary

Ischemic stroke is a multifactorial event involving a cascade of cellular and molecular mechanisms that evolve over time. The initial energy failure triggers processes of excitotoxicity, oxidative and nitrosative stress, and inflammation, leading to neuronal death through various pathways. The temporal dynamics of injury highlight critical periods for intervention, emphasizing the importance of timely therapeutic strategies.

Understanding the complex interplay of these mechanisms offers opportunities for developing targeted treatments. While significant challenges remain in translating preclinical findings into effective clinical therapies, ongoing research continues to explore novel approaches aimed at reducing injury and enhancing recovery. Advances in imaging, molecular biology, and neuroscience hold promise for improving outcomes and reducing the burden of stroke on individuals and society.

3.4 Cross-Species Mapping Frameworks

Understanding the human brain remains one of the greatest challenges in neuroscience. Given ethical and practical limitations in studying the human brain directly, researchers often rely on animal models to investigate neural mechanisms. Cross-species mapping frameworks are essential for translating findings from animal studies to humans, enabling the study of brain function, evolution, and disease. These frameworks help bridge the gap between what we learn from different species and how that information can be applied to understand human brain function, particularly in the context of neurological disorders and treatments.

This section provides a comprehensive discussion on the frameworks for cross-species

mapping in neuroscience, setting the stage for the development of the proposed functional connectivity mapping approach in subsequent chapters. By exploring the integration of structural and functional connectivity data, advanced computational tools, and network science techniques, we aim to provide a foundational understanding for the cross-species methodology adopted in this thesis.

3.4.1 Introduction to Cross-Species Mapping

Cross-species studies in neuroscience play an important role in understanding fundamental mechanisms underlying brain function. These studies enable researchers to translate findings from animal models to humans, thus providing valuable insights into human neurobiology. However, challenges arise in aligning structural and functional brain data across species due to interspecies variability in brain size, anatomy, and functional organization [47]. To address these challenges, frameworks integrating both structural and functional connectivity have been developed, allowing researchers to identify conserved and divergent features across species.

3.4.2 Structural Connectivity Mapping

Structural connectivity mapping relies on diffusion MRI (dMRI) and tract-tracing methods to investigate the white matter architecture of the brain. Rogier Mars et al. have proposed a framework (Figure 3.12) for structural connectivity mapping that leverages connectivity fingerprints, which are derived from diffusion data to characterize inter-regional anatomical connections [48]. This framework uses dimensionality reduction techniques such as multidimensional scaling (MDS) to visualize cross-species similarities in connectivity patterns, thus facilitating comparisons between the structural connectomes of different species.

To mathematically describe structural connectivity, let us define the connectivity matrix $C \in \mathbb{R}^{n \times n}$, where n is the number of regions of interest (ROIs) in the brain. Each element

C_{ij} represents the strength of the structural connection between regions i and j. Diffusion MRI provides estimates of these connection strengths by modeling the diffusion of water molecules along white matter tracts, often using a tensor-based approach. The diffusion tensor $\mathbf{D}$ is a symmetric positive-definite matrix that can be diagonalized as:

$$\mathbf{D} = \mathbf{E}\mathbf{\Lambda}\mathbf{E}^T, \tag{3.36}$$

where $\mathbf{E}$ is the matrix of eigenvectors and $\mathbf{\Lambda}$ is the diagonal matrix of eigenvalues. The principal eigenvector indicates the primary direction of diffusion, which is assumed to align with the orientation of white matter fibers.

Connectivity fingerprints offer a compact representation of the connectivity profile of each brain region, highlighting unique and conserved anatomical features. Mathematically, let $\mathbf{f}_i \in \mathbb{R}^n$ represent the connectivity fingerprint of region i, which is defined as the i-th row of the connectivity matrix C. Dimensionality reduction techniques like MDS and principal component analysis (PCA) are often used to transform the high-dimensional connectivity data into a low-dimensional space that captures the most important features of the connectome [48]. Specifically, given the connectivity matrix C, PCA seeks to find a set of orthogonal components that maximize the variance in the data by solving the eigenvalue problem:

$$\mathbf{C}^T\mathbf{C}\mathbf{v} = \lambda\mathbf{v}, \tag{3.37}$$

where λ represents the eigenvalues and $\mathbf{v}$ represents the principal components. This allows for the quantitative assessment of cross-species similarities, helping identify homologous brain regions across species.

A key strength of structural connectivity approaches is their ability to provide a detailed mapping of anatomical pathways, which is particularly useful for identifying conserved white matter tracts. However, these methods also have limitations, such as the inability to de-

termine the directionality of connections and the potential for inaccuracies in regions with crossing fibers. Moreover, structural connectivity alone may not fully capture the dynamic nature of brain networks, necessitating the integration of functional connectivity data for a more complete understanding.

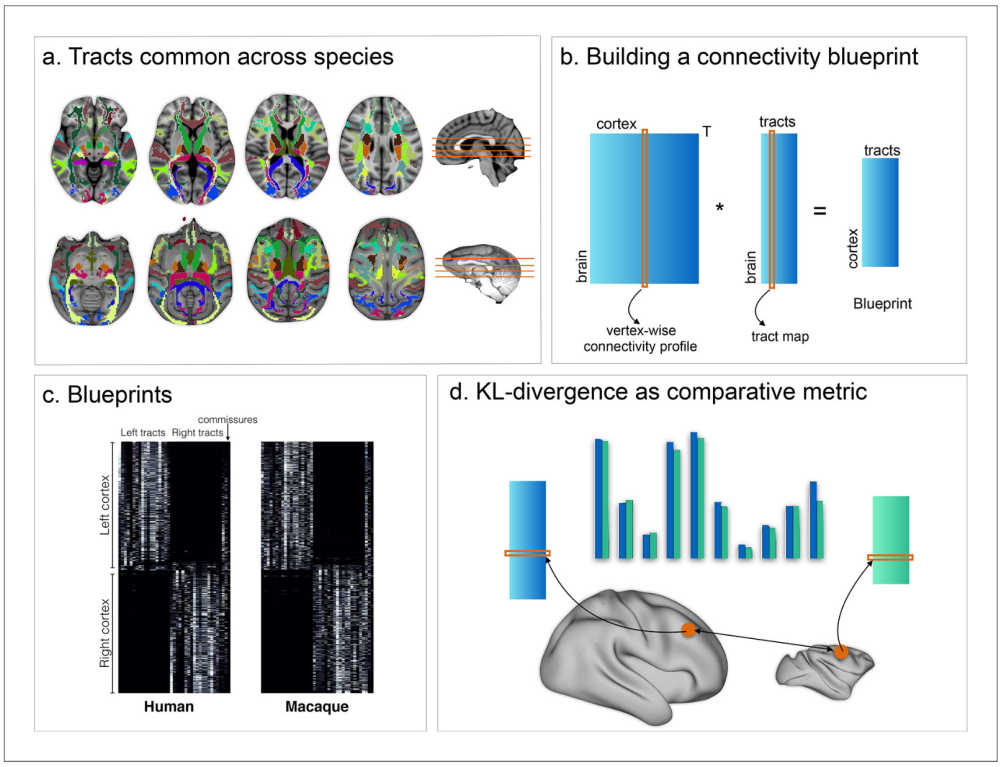

Figure 3.12: **Cross-Species Structural Connectivity Mapping Framework by Mars et al. (2018). (a) Tracts Common Across Species:** Structural tracts conserved between humans and non-human primates, visualized across multiple brain slices. These tracts serve as the foundation for comparing connectivity patterns between species. **(b) Building a Connectivity Blueprint:** The blueprint is constructed by computing vertex-wise connectivity profiles for each region in the brain, followed by a matrix multiplication with a tract map, resulting in a summary representation of connectivity patterns across the cortex. **(c) Blueprints:** Comparative visualization of connectivity blueprints for human and macaque cortex, emphasizing both left and right cortical tracts as well as commissural pathways. **(d) KL-Divergence as a Comparative Metric:** The Kullback-Leibler (KL) divergence is employed as a metric to quantify differences in connectivity blueprints between species, highlighting both similarities and unique features of each species' structural organization. Adapted from Mars et al 2018 [48].

3.4.3 Functional Connectivity Mapping

Resting-state fMRI has emerged as a powerful tool for investigating functional connectivity in both humans and animal models. In cross-species research, rsfMRI allows for the identification of conserved functional networks, such as the Default Mode Network (DMN), across species [47]. Graph theory approaches are commonly employed to analyze functional connectivity, wherein nodes represent brain regions and edges represent the statistical dependencies between them.

To represent functional connectivity mathematically, let us define a graph $G = (V, E)$, where V is the set of nodes representing brain regions, and E is the set of edges representing the functional connections between these regions. The functional connectivity between two regions i and j can be quantified by the Pearson correlation coefficient r_{ij} (eq. 3.27) of their respective time series $x_i(t)$ and $x_j(t)$.

Key metrics used in graph theory include the clustering coefficient, C_i, which measures the tendency of nodes to form tightly connected clusters. The clustering coefficient for node i is defined as:

$$C_i = \frac{2e_i}{k_i(k_i - 1)}, \tag{3.38}$$

where e_i is the number of edges between the neighbors of node i, and k_i is the degree of node i (i.e., the number of edges connected to node i).

Global efficiency, E_{glob}, quantifies the efficiency of information transfer across the entire network and is defined as:

$$E_{glob} = \frac{1}{n(n-1)} \sum_{i \neq j \in V} \frac{1}{d_{ij}}, \tag{3.39}$$

where d_{ij} is the shortest path length between nodes i and j, and n is the total number of nodes in the graph.

Modularity, Q, assesses the degree to which the network can be subdivided into distinct

modules and is defined as:

$$Q = \frac{1}{2m} \sum_{i,j \in V} \left[A_{ij} - \frac{k_i k_j}{2m} \right] \delta(c_i, c_j), \tag{3.40}$$

where A_{ij} is the adjacency matrix representing the presence of an edge between nodes i and j, k_i and k_j are the degrees of nodes i and j, m is the total number of edges in the network, and $\delta(c_i, c_j)$ is an indicator function that equals 1 if nodes i and j belong to the same module and 0 otherwise.

These metrics are useful for identifying homologous networks across species and for understanding the impact of neurological conditions, such as stroke, on brain network organization.

Despite its utility, functional connectivity mapping faces several challenges when applied across species. Anatomical differences between species lead to variability in network topology, making it difficult to directly compare functional networks. Moreover, differences in the temporal resolution of rsfMRI data across species can introduce discrepancies in connectivity metrics, necessitating the development of advanced alignment techniques.

3.4.4 Multimodal Integration Approaches

To address the limitations of using either structural or functional connectivity alone, multimodal integration approaches have been developed. These approaches combine structural and functional data to provide a more comprehensive understanding of brain connectivity. Joint embedding techniques, for example, allow for the simultaneous analysis of multiple modalities, facilitating the identification of cross-species correspondences [47].

Canonical Correlation Analysis (CCA) is another powerful tool for cross-species alignment. By maximizing the correlation between linear combinations of structural and functional connectivity features, CCA can identify shared patterns that may not be apparent from either modality alone. Integrating molecular and genetic data with connectivity mea-

sures further enhances the robustness of cross-species mapping, providing insights into the biological underpinnings of network organization.

3.4.5 Advanced Computational and Mathematical Frameworks

Advanced computational and mathematical tools are essential for tackling the complexity of cross-species brain mapping. Manifold alignment techniques, for example, provide a means of aligning brain connectivity data in a shared low-dimensional space. Procrustes analysis is commonly used for linear alignment, while non-linear manifold alignment techniques are better suited for capturing complex, non-linear relationships between species [48].

Optimal transport theory offers a mathematically rigorous framework for understanding cross-species differences in network topology. By modeling the problem of aligning brain networks as a transportation problem, optimal transport provides a principled way to match brain regions between species while minimizing the cost of alignment. Mathematically, given two probability distributions P and Q representing connectivity patterns in two species, the goal is to find a transport plan γ that minimizes the Wasserstein distance:

$$W(P,Q) = \inf_{\gamma \in \Gamma(P,Q)} \int_{\mathcal{X}\times\mathcal{Y}} d(x,y) d\gamma(x,y), \tag{3.41}$$

where $\Gamma(P,Q)$ is the set of all possible transport plans and $d(x,y)$ is the cost function associated with transporting mass from x to y. This approach has proven useful for quantifying interspecies differences in network organization and for identifying conserved features of brain architecture.

3.4.6 Network Science Tools for Cross-Species Mapping

Network science provides tools for comparing brain networks across species. Graph theory metrics have been extensively used to identify conserved topological features, such as

small-world properties and community structure, in the connectomes of various species [47]. Network control theory (NCT) further extends these analyses by modeling the brain as a dynamical system and identifying control points that can influence brain state transitions [47].

To represent the brain as a dynamical system, let us define the brain state vector $\mathbf{x}(t) \in \mathbb{R}^n$, where n is the number of brain regions, and $\mathbf{x}(t)$ represents the activity level of each region at time t. The evolution of the brain state can be modeled using a linear system:

$$\frac{d\mathbf{x}(t)}{dt} = A\mathbf{x}(t) + B\mathbf{u}(t), \tag{3.42}$$

where $A \in \mathbb{R}^{n \times n}$ is the structural connectivity matrix that defines the interactions between brain regions, $B \in \mathbb{R}^{n \times m}$ is the input matrix that defines how external inputs affect the brain, and $\mathbf{u}(t) \in \mathbb{R}^m$ is the control input vector.

The goal of network control theory is to determine the control input $\mathbf{u}(t)$ that drives the brain from an initial state $\mathbf{x}(0)$ to a desired target state $\mathbf{x}_f$ within a certain time frame. The minimum energy control input can be found by solving the following optimization problem:

$$\min_{\mathbf{u}(t)} \int_0^T \mathbf{u}^T(t)\mathbf{u}(t)\, dt, \tag{3.43}$$

subject to the constraint given by the state equation above. The solution to this problem provides the optimal control strategy for transitioning between brain states, which is crucial for understanding how perturbations can influence whole-brain dynamics.

One important concept in NCT is the controllability Gramian W_c, which is defined as:

$$W_c = \int_0^T e^{At} B B^T e^{A^T t}\, dt. \tag{3.44}$$

The Gramian W_c provides a measure of how controllable the system is from a given set of

inputs. If W_c is full rank, then the system is said to be completely controllable, meaning that it is possible to drive the system from any initial state to any final state using an appropriate control input.

By identifying key control points, NCT can predict how perturbations to specific regions will impact whole-brain dynamics, providing insights into potential therapeutic targets for modulating brain activity across species. For example, brain regions with high controllability are those that can efficiently drive the system to different states, making them important targets for interventions aimed at altering brain function.

3.4.7 Validation and Evaluation Techniques

The validation of cross-species mapping frameworks is a crucial step in ensuring their reliability and translational value. Statistical methods, such as cross-validation and permutation testing, are commonly used to assess the quality of the mappings. Biological validation, including the use of conserved networks like the DMN, further ensures that the identified correspondences are meaningful and not artifacts of the alignment process.

3.4.8 Future Directions and Challenges

Future work in cross-species brain mapping should address the variability in brain size, anatomy, and function across species. Expanding current frameworks to include multi-scale data, such as cellular resolution and gene expression, could enhance the robustness of cross-species comparisons. Additionally, machine learning approaches hold great promise for improving mapping accuracy by leveraging large-scale datasets and identifying complex, non-linear relationships between species [47].

3.5 Chapter Summary

Chapter 3 has established a comprehensive foundation for understanding the principles and challenges of cross-species connectivity mapping in the context of ischemic stroke. We began with an exploration of MRI fundamentals, the neurovascular mechanisms underlying functional MRI, and the key pathophysiological processes involved in stroke. This background is crucial for interpreting connectivity changes that occur during different stages of ischemic injury, and it guides the methodological approaches used in cross-species analysis.

The chapter also reviewed existing cross-species mapping frameworks, particularly the structural connectivity approaches developed by Rogier Mars and colleagues. These methods, along with advanced tools such as graph theory metrics, dimensionality reduction, and manifold alignment, provide a solid theoretical basis for comparing connectivity profiles across species. While structural mapping has traditionally dominated cross-species studies, this thesis emphasizes functional connectivity mapping, particularly using resting-state fMRI to explore network-level activity and identify conserved features between humans and canines.

With this groundwork laid, Chapter 4 will build on these concepts to describe the development of our cross-species functional connectivity mapping framework. This framework will involve experimental designs for human and canine rsfMRI data, as well as mathematical formulations to align and compare connectivity across species. By linking the detailed theoretical insights from this chapter to the practical approaches used in the next, we aim to develop a rigorous and effective tool for translating preclinical findings into clinical outcomes. This ultimately supports the overarching goal of advancing our understanding of brain function and improving therapeutic strategies for ischemic stroke.

Chapter 4 Development of a Cross-Species Connectivity Mapping Framework

The capacity to translate findings from animal models into clinically relevant human knowledge is a central objective in translational neuroscience. Although fMRI has greatly advanced our ability to probe neural connectivity and network organization, effectively bridging the gap between controlled animal studies and complex human pathophysiology remains challenging. The motivation for developing a cross-species connectivity mapping framework arises from this translational imperative, particularly in the context of ischemic stroke—a condition with profound implications for long-term patient disability and recovery potential.

Previous chapters have laid theoretical and foundational groundwork: we explored the physics and mathematics of MRI, the principles underlying the Blood-Oxygen-Level-Dependent (BOLD) signal, and the physiological and pathophysiological processes that underpin stroke-induced neural network disruption. Building upon these foundations, the present chapter turns to the practical dimensions of constructing a systematic, mathematically rigorous, and computationally robust pipeline. Here we address how to design experiments that yield comparable canine and human datasets, select appropriate MRI parameters, ensure stable physiological conditions, and integrate multimodal imaging data. We then detail a series of preprocessing steps—each mathematically justified and validated—to ensure that the resulting time-series data accurately reflect underlying neural signals.

The chapter then presents a variety of connectivity analysis methods, including seed-

based correlation, Independent Component Analysis (ICA), and graph-theoretical metrics. Each approach is dissected to reveal the mathematical formulations and statistical considerations that inform interpretations of functional connectivity. Following this, we introduce advanced cross-species alignment strategies, employing optimal transport theory, manifold alignment, and graph matching algorithms. These techniques, grounded in solid theoretical frameworks, enable us to identify meaningful correspondences between species at multiple scales of network complexity.

Moreover, we emphasize validation procedures to ensure that results are stable, reproducible, and biologically plausible. We highlight how simulations, known biological benchmarks, cross-validation schemes, and Bayesian uncertainty modeling can reinforce confidence in the derived correspondences. Finally, we discuss extensions of this framework, including time-varying connectivity modeling, multimodal integration, scaling analyses, and even evolutionary perspectives that broaden the utility and applicability of these methods.

Ultimately, this chapter offers a richly detailed blueprint to guide researchers in bridging the gap between preclinical animal models and human clinical populations, facilitating the translation of mechanistic insights into therapeutic strategies that can improve outcomes for patients recovering from stroke and related neurological disorders.

4.1 Experimental Design

4.1.1 Rationale for Employing Canine Models

Effective translation from animal models to human pathology hinges on selecting a model species that shares key anatomical, physiological, and functional characteristics with humans. Rodent models, while common, face limitations due to their relatively smooth, lissencephalic cortex and distinct vascular architectures. By contrast, canines offer several advantages (Figure 4.1):

- **Cortical Gyrification and Complexity:** The canine brain is gyrencephalic, more closely resembling the folded cortical structure of the human brain. This similarity supports more accurate anatomical registration and more comparable patterns of cortical network organization.

- **Vascular Architecture and Hemodynamics:** Canine cerebral vasculature and autoregulatory mechanisms approximate human conditions more closely than rodent models. This structural and physiological similarity is crucial when studying ischemic stroke, where vascular dynamics significantly influence tissue damage and network dysfunction.

- **Imaging Feasibility and Scale:** The larger canine brain size allows for MRI parameters that approach human image resolutions and contrasts, reducing confounding differences driven purely by scale.

- **Anesthetized Stability and Parameter Control:** Canines can be maintained under controlled anesthesia, ensuring stable physiological parameters (blood pressure, gases, temperature), minimizing motion, and enhancing reproducibility. Adapted from Arnold et al (2020) and Kyathanally et al (2015) [49, 8]

These characteristics collectively justify the canine model choice, allowing us to produce datasets with a higher likelihood of meaningful cross-species functional comparisons, ultimately strengthening the translational bridge from bench to bedside.

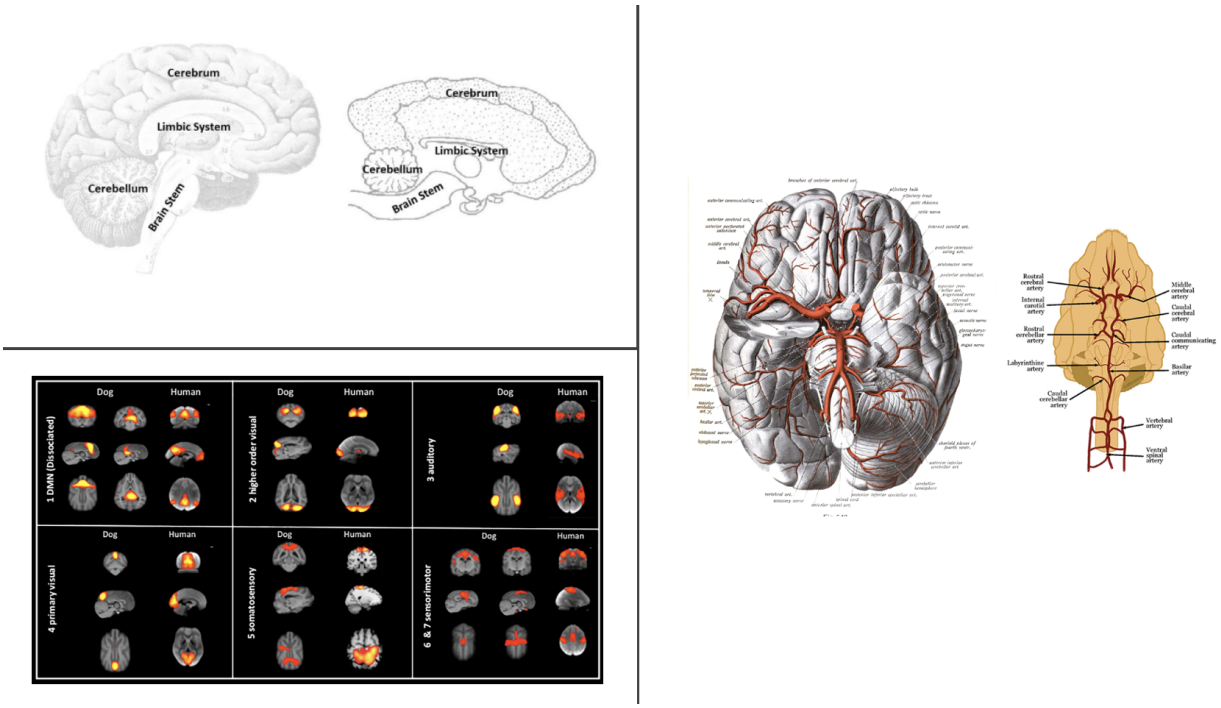

Figure 4.1: Cross-Species Brain Organization and Network Comparison. (Top Left) Sagittal views comparing canine (left) and human (right) brain anatomy, highlighting key structures including cerebrum, cerebellum, limbic system, and brain stem. Both species demonstrate gyrencephalic cortices with similar organizational principles. (Bottom Left) Comparison of resting-state functional networks between canine and human brains, showing remarkable conservation of network architecture across species. Networks displayed include default mode network (DMN), primary visual, higher-order visual, somatosensory, and sensorimotor networks. (Right) Vascular anatomy comparison highlighting the similarities in cerebral arterial organization between species, particularly in the distribution of major cerebral arteries. The structural and functional homologies between canine and human brains underscore the translational value of canine models in stroke research.

4.1.2 Cohort Composition and Temporal Alignment

To interrogate stroke-induced connectivity changes and test therapeutic strategies, we established three canine cohorts subjected to permanent middle cerebral artery occlusion (MCAO):

- **Control/Natural History Group:** MCAO without additional interventions, mapping the baseline trajectory of post-stroke network reorganization.

- **NEH Treatment Group:** Administration of norepinephrine and hydralazine to manipulate systemic hemodynamics, probing how vascular modulation affects functional connectivity (FC).
- **Sanguinate Treatment Group:** Infusion of an oxygen-carrying solution aimed at enhancing tissue oxygenation and potentially stabilizing or restoring functional networks.

Each group included approximately 12–14 animals, a sample size determined by power analyses incorporating pilot data on variability and expected effect sizes [9]. These analyses considered desired confidence intervals, ensuring that subsequent statistical tests have sufficient power to detect meaningful differences.

For the human data, we sourced resting-state fMRI datasets from the OpenNeuro platform. Specifically, we utilized the OpenNeuro **ds000224** dataset for human control subjects and the OpenNeuro **ds003999** dataset for human stroke patients. These public datasets offered standardized acquisition protocols, quality controls, and accompanying meta-data, thus providing a solid reference point for cross-species comparisons.

On the human side, datasets were matched to the canine imaging intervals by selecting patients scanned at comparable times post-stroke onset (t_{stroke}). Aligning the imaging timeline helps ensure that observed connectivity differences reflect cross-species phenomena rather than arbitrary temporal mismatches:

$$t_{\text{canine}}^{(imaging)} \approx t_{\text{human}}^{(imaging)}.$$

4.1.3 Ethical and Translational Justifications

All animal procedures were conducted under Institutional Animal Care and Use Committee (IACUC) guidelines, ensuring humane treatment and scientifically valid justifications for the chosen interventions and methodologies. By selecting a model that offers higher translational

fidelity, the effort and ethical cost of animal studies are justified by the increased potential for clinically relevant insights. The use of publicly available human data from OpenNeuro further promotes transparency, reproducibility, and broad accessibility of the analytic workflows.

4.2 Data Acquisition Protocols

4.2.1 MRI Parameter Optimization

Scanning was performed on high-field 3T MRI systems for both canines and humans. After iterative pilot studies to balance signal-to-noise ratio (SNR), temporal resolution, and BOLD sensitivity, we selected:

- **Canines:** TR $\approx$ 1400 ms, TE $\approx$ 20 ms, voxel size 2.5 mm isotropic, and approximately 300 volumes per run.
- **Humans (OpenNeuro ds000224 and ds003999):** TR $\approx$ 2000 ms, TE $\approx$ 30 ms, voxel size 3 mm isotropic, with similar total volumes per run.

While not identical, these parameters produce comparable temporal sampling of resting-state fluctuations and sufficient spatial resolution to resolve major cortical and subcortical structures. Coil selection and B0 shimming minimized susceptibility artifacts, ensuring more uniform image quality.

4.2.2 Physiological Monitoring and Stability Control

For canines, anesthesia (1% isoflurane) stabilized the metabolic and vascular baseline. We closely monitored arterial blood pressure (ABP), end-tidal CO_2 ($EtCO_2$), arterial blood gases (pO_2, pCO_2), and body temperature. Adjusting ventilation rates and anesthetic depths maintained these parameters within targeted ranges. This reduces physiological noise and

variability, ensuring that connectivity differences are more likely to stem from neural processes rather than systemic confounds.

In contrast, human subjects from OpenNeuro datasets remained awake but were typically instructed to rest quietly with eyes closed or fixating on a minimal visual stimulus to minimize head motion and non-neural variability. Although humans cannot be physiologically "standardized" like anesthetized canines, consistent protocols within these publicly available datasets and careful subject screening ensured that baseline conditions remained reasonably stable.

4.2.3 Multimodal Imaging and Structural References

In both species, high-resolution T1-weighted structural images supported spatial normalization, tissue segmentation, and atlas-based ROI definitions. Diffusion tensor imaging (DTI) provided structural connectivity estimates to cross-check functional alignments. In canines, digital subtraction angiography confirmed MCAO location and collateral patterns, informing interpretations of perfusion deficits and their relationship to FC changes.

For the human datasets from OpenNeuro, associated structural scans (T1-weighted MRIs) were also available, ensuring consistent processing and ROI definition strategies.

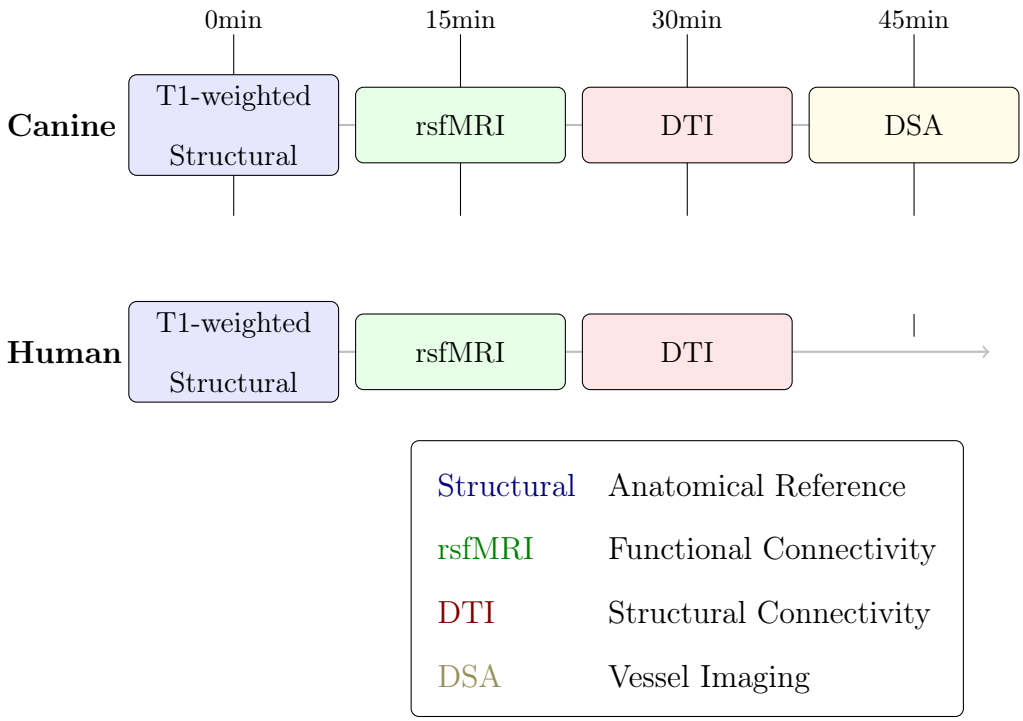

Figure 4.2: Multimodal imaging protocol timeline for cross-species connectivity mapping. The diagram illustrates the sequence and timing of different imaging modalities acquired for both canine and human subjects. For canines, the protocol includes Digital Subtraction Angiography (DSA) to confirm MCAO location and assess collateral patterns. Human data from OpenNeuro follows a similar protocol excluding DSA. All modalities contribute to a comprehensive assessment of brain structure, function, and connectivity patterns essential for cross-species mapping.

4.3 Preprocessing Pipeline

Note: All preprocessing steps conducted on the canine and human datasets were performed using various FSL tools [50].

4.3.1 Motion Correction and Artifact Mitigation

Raw fMRI data often contain motion-induced artifacts that obscure true neural signals. We employed a six-parameter rigid-body realignment step:

$$\mathbf{x}_t^* = \mathbf{M}_t \mathbf{x}_t,$$

where $\mathbf{x}_t \in \mathbb{R}^V$ is the volume at time t, and $\mathbf{M}_t$ encodes rotations and translations minimizing a cost function $D(\mathbf{x}_t, R)$ between the current volume and a reference R. This reduces spatial mismatch over time.

Framewise displacement (FD) and DVARS metrics identified time points with excessive movement:

$$FD_t = \sum_{\dim \in \{x,y,z\}} |u_t - u_{t-1}| + |v_t - v_{t-1}| + |w_t - w_{t-1}|,$$

$$DVARS_t = \sqrt{\frac{1}{V} \sum_v (x_t(v) - x_{t-1}(v))^2}.$$

Volumes exceeding pre-established thresholds were either censored or modeled as nuisance regressors, ensuring that motion spikes did not spuriously inflate connectivity estimates. These steps were consistently applied to both canine and human data, including the OpenNeuro datasets, promoting methodological uniformity.

4.3.2 Physiological Noise Regression

Physiological fluctuations—cardiac pulsation and respiration—introduce structured variance. Using RETROICOR and related techniques, we modeled these effects as expansions of sine and cosine terms at harmonics of the physiological frequencies:

$$S(t) = S_0(t) + \sum_{h=1}^{H} [a_h \cos(h\phi(t)) + b_h \sin(h\phi(t))],$$

where $\phi(t)$ represents the cardiac or respiratory phase. Additionally, principal component-based methods (CompCor) extracted noise components from WM and CSF masks, adding them as nuisance regressors.

The cleaned signal $\hat{S}(t)$ after regressing out nuisance terms is:

$$\hat{S}(t) = S(t) - X_{\text{nuis}}(t)\beta_{\text{nuis}},$$

substantially reducing non-neural variance and improving the fidelity of the resting-state signal.

4.3.3 Temporal Filtering and Detrending

We focused on low-frequency BOLD fluctuations (0.01–0.1 Hz) characteristic of resting-state networks. A bandpass filter:

$$Y_{\text{filtered}}(\omega) = H(\omega)Y_{\text{raw}}(\omega),$$

with $H(\omega)$=1 in the band of interest and 0 otherwise, isolates relevant temporal scales. Polynomial detrending (e.g., removing linear or quadratic trends) mitigated slow scanner drifts and thermal noise. The result is a temporally stable time-series centered on the frequency domain where meaningful rsFC signals reside.

4.3.4 Spatial Normalization and Nonlinear Registration

To facilitate group-level analyses and cross-species comparisons, we employed nonlinear registration to transform individual brains into a standardized template space. For canines:

$$\mathbf{x}^{(dog)}_{template} = f_{\theta_{dog}}(\mathbf{x}^{(dog)}_{native}),$$

and for humans:

$$\mathbf{x}_{template}^{(human)} = g_{\theta_{human}}(\mathbf{x}_{native}^{(human)}),$$

where $f_{\theta_{dog}}$ and $g_{\theta_{human}}$ are estimated via optimization algorithms (e.g., symmetric diffeomorphic normalization) that maximize similarity metrics (like mutual information) and impose smoothness constraints. This step ensures that voxel coordinates correspond to roughly analogous anatomical locations. Applying consistent normalization strategies to the OpenNeuro human datasets and the canine data promotes a common spatial framework crucial for subsequent cross-species alignment.

4.3.5 Smoothing and Quality Assurance

Spatial smoothing with a Gaussian kernel improves SNR but must be chosen carefully to avoid blurring distinct structures. We selected a full-width-at-half-maximum (FWHM) kernel proportional to brain size (e.g., 6 mm for humans, 5 mm for canines [7]) to maintain anatomical specificity. Quality assurance checks included evaluating temporal SNR distributions, ensuring no significant residual motion patterns remained, and verifying accurate alignment to the template.

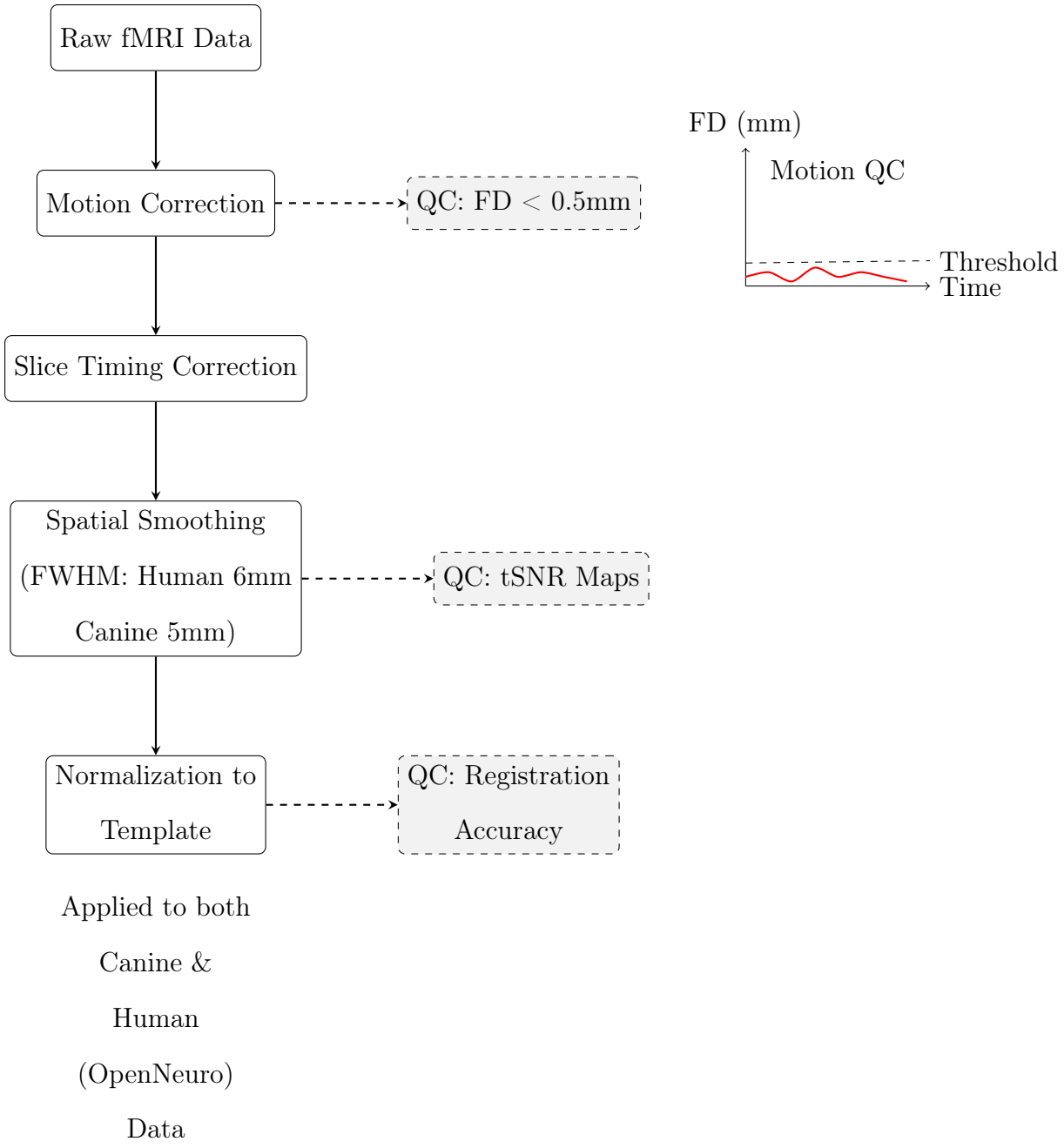

Figure 4.3: Preprocessing pipeline flowchart showing the progression from raw fMRI data to fully preprocessed datasets. Quality control (QC) checkpoints are indicated by dashed boxes, including framewise displacement (FD) monitoring, temporal SNR assessment, and registration validation. The example plot (right) shows typical FD values across time, with the 0.5mm threshold indicated. The same preprocessing steps are applied to both canine and human datasets, with species-specific smoothing kernels (FWHM: 6mm for humans, 5mm for canines) to maintain anatomical specificity while improving SNR.

4.4 Functional Connectivity Analysis and Quantification

4.4.1 Seed-Based Correlation Mapping

Seed-based analysis is conceptually straightforward: we define a seed ROI and compute the Pearson correlation of its time-series $x_s(t)$ with every other voxel/ROI $x_j(t)$:

$$r_{sj} = \frac{\sum_t (x_s(t) - \bar{x}_s)(x_j(t) - \bar{x}_j)}{\sqrt{\sum_t (x_s(t) - \bar{x}_s)^2}\sqrt{\sum_t (x_j(t) - \bar{x}_j)^2}}.$$

Applying the Fisher z-transform:

$$z_{sj} = \frac{1}{2} \ln \left(\frac{1 + r_{sj}}{1 - r_{sj}} \right),$$

yields a Gaussianized distribution amenable to parametric statistical testing. Seed-based maps can highlight well-known networks (e.g., the motor network from a primary motor cortex seed) and serve as an intuitive starting point for cross-species comparisons. By selecting homologous regions as seeds (based on known functional-anatomical correspondences), we can directly inspect similarities and differences in connectivity patterns.

4.4.2 Independent Component Analysis (ICA)

As previously discussed, ICA decomposes spatiotemporal data into statistically independent sources:

$$\mathbf{X} = \mathbf{AS},$$

with $\mathbf{X} \in \mathbb{R}^{T \times V}$, $\mathbf{A} \in \mathbb{R}^{T \times C}$, and $\mathbf{S} \in \mathbb{R}^{C \times V}$. The rows of $\mathbf{S}$ are spatial maps of independent components, often interpretable as intrinsic connectivity networks (ICNs). The number of components C is chosen via model order selection (e.g., information criteria or minimum description length).

Non-Gaussianity measures (e.g., neg-entropy) guide the ICA optimization. Once components are derived, we identify putative cross-species analogs by computing spatial correlation:

$$\text{Sim}(S_i^{(dog)}, S_j^{(human)}) = \frac{S_i^{(dog)} \cdot S_j^{(human)}}{\|S_i^{(dog)}\| \|S_j^{(human)}\|}.$$

High similarity values suggest that corresponding networks are preserved across species, enabling direct comparisons of network strength, extent, and vulnerability to stroke. Applying ICA consistently to canine and human datasets ensures that extracted networks are methodologically compatible.

4.4.3 Graph-Theoretical Metrics and Network Topology

Representing each subject's connectivity pattern as a weighted graph (Figure 4.4) $G = (N, E)$, where N is the node set (ROIs) and E encodes edges weighted by connectivity strength (z-values), we compute topological metrics that characterize the "connectome":

- **Global Efficiency:**

$$E_{glob}(G) = \frac{1}{N} \sum_i \left(\frac{1}{\frac{1}{N-1} \sum_{j \neq i} d_{ij}} \right),$$

  quantifies how efficiently information is exchanged globally in the network.

- **Modularity:**

$$Q = \sum_u (e_{uu} - (\sum_v e_{uv})^2),$$

  measures the strength of community structure, where e_{uv} is the fraction of edges between communities u and v.

- **Other Metrics:** Clustering coefficients C_i, characteristic path length L, and small-worldness σ offer nuanced views of network integration and segregation.

By comparing these metrics across species and under different conditions (e.g., before and after therapeutic intervention), we can identify fundamental network organizational principles and assess whether similar topological patterns emerge in canines and humans following ischemic insult.

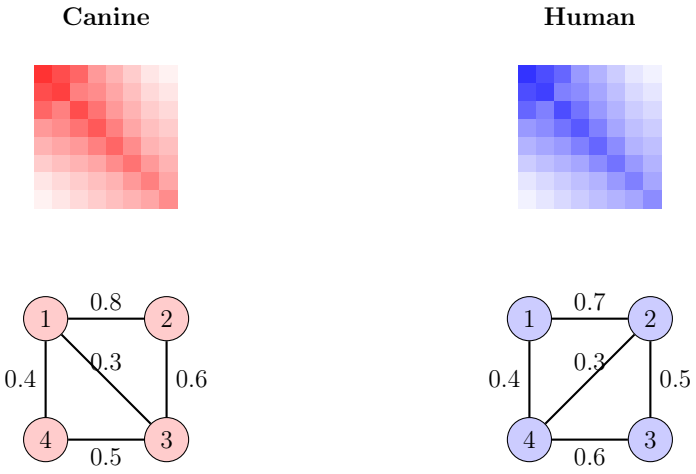

Metric	Canine	Human
Global Efficiency	0.65	0.62
Modularity	0.42	0.38
Clustering Coefficient	0.58	0.54

Figure 4.4: Cross-Species Network Analysis Comparison. Top: Connectivity matrices showing correlation strength between ROIs for canine (left) and human (right) resting-state networks. The color intensity represents the strength of functional connectivity (red/blue for positive correlations). Middle: Graph representations of the connectivity matrices, where nodes represent brain regions and edges represent functional connections weighted by correlation strength. Edge weights are shown numerically on the connections. Bottom: Comparison of key network metrics between species, including global efficiency, modularity, and clustering coefficients, demonstrating similar topological organization despite anatomical differences.

4.5 Cross-Species Mapping Methodology

4.5.1 Defining Functional Fingerprints

To align networks across species, we first encapsulate each ROI's functional profile into a feature vector (functional fingerprint) that may include:

- Mean connectivity strengths to various ROIs
- ICA component loadings
- Graph-theoretical metrics (node degree, betweenness, eigenvector centrality)

Let:

$$\mathbf{F}_i^{(dog)} \in \mathbb{R}^M, \quad \mathbf{F}_j^{(human)} \in \mathbb{R}^M,$$

representing the M-dimensional feature vectors for ROI i in canines and ROI j in humans.

4.5.2 Optimal Transport for Cross-Species Alignment

Optimal transport theory provides a powerful framework for matching distributions:

$$\min_{\Gamma \geq 0} \sum_{i,j} \Gamma_{ij} C_{ij}, \quad \sum_j \Gamma_{ij} = p_i, \ \sum_i \Gamma_{ij} = q_j,$$

where $C_{ij} = \|\mathbf{F}_i^{(dog)} - \mathbf{F}_j^{(human)}\|^2$ or another dissimilarity measure, and p_i, q_j represent distributions over ROIs in each species. Entropy-regularized optimal transport (using a Sinkhorn algorithm) solves this efficiently:

$$\Gamma^\lambda = \arg\min_{\Gamma} \sum_{i,j} \Gamma_{ij} C_{ij} + \lambda \sum_{i,j} \Gamma_{ij} \ln(\Gamma_{ij}).$$

Adjusting λ controls the degree of smoothing, balancing fidelity and robustness. The resulting coupling Γ identifies which canine ROIs correspond to which human ROIs in a global, distributional sense.

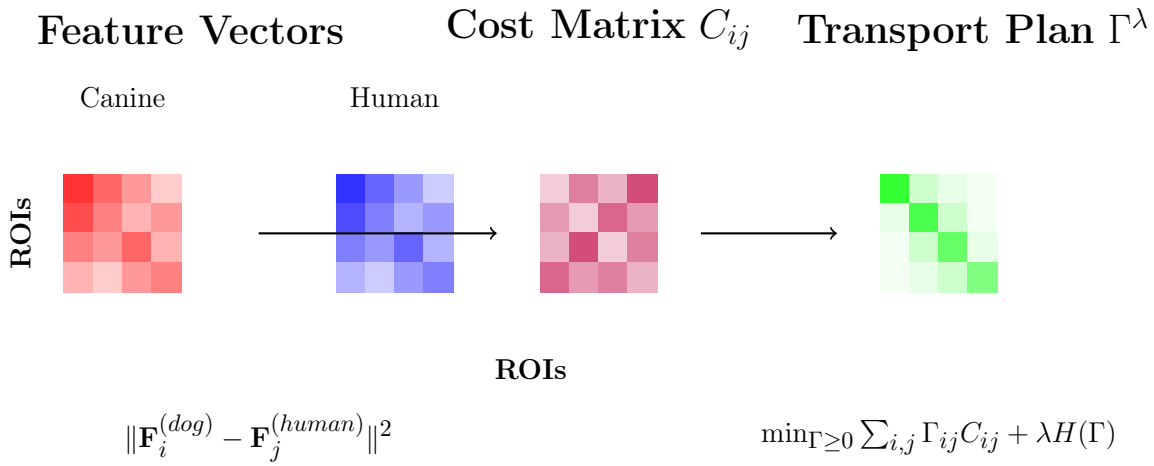

Figure 4.5: Cross-Species Optimal Transport Alignment Framework. The process begins with feature vectors (left) representing functional connectivity profiles for each ROI in both canine and human brains. These features are used to compute a cost matrix (center) measuring dissimilarity between ROI pairs across species. The optimal transport algorithm then produces a transport plan (right) that identifies corresponding regions while respecting global distributional constraints. Darker colors indicate stronger correspondence/higher values. The entropy regularization term $\lambda H(\Gamma)$ ensures smooth, robust solutions while maintaining biological plausibility in the final mapping.

4.5.3 Manifold Alignment and Geometric Approaches

Manifold alignment embeds both canine and human fingerprints into a lower-dimensional manifold while preserving local geometry:

$$\mathbf{Y}^{(dog)} = \mathcal{E}(\mathbf{F}^{(dog)}), \quad \mathbf{Y}^{(human)} = \mathcal{E}(\mathbf{F}^{(human)}),$$

where $\mathcal{E}$ could be Laplacian eigenmaps, diffusion maps, or Isomap embeddings. We then solve:

$$\min_{R \in O(d)} \|\mathbf{Y}^{(dog)} - R\mathbf{Y}^{(human)}\|_F,$$

an orthogonal Procrustes problem. By aligning the embedded manifolds, we map canine nodes to human nodes based on intrinsic structural similarity of their connectivity patterns. This geometric approach avoids relying solely on direct pairwise costs, leveraging global manifold structures to guide alignment.

4.5.4 Graph Matching Algorithms

When focusing on topological similarity, we can frame alignment as a graph matching problem:

$$\max_{\pi} \sum_{i,j} W_{ij}^{(dog)} W_{\pi(i)\pi(j)}^{(human)},$$

where $W^{(dog)}$ and $W^{(human)}$ are adjacency matrices derived from connectivity strengths. Although NP-hard, approximate solutions (e.g., spectral relaxations, relax-and-round algorithms) yield mappings that prioritize consistent network topology across species. Such topologically informed alignment can reveal homologous communities or modules that reflect conserved functional architectures.

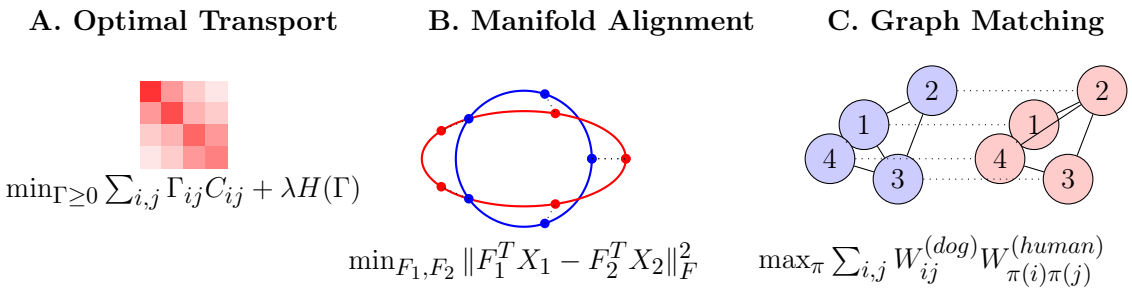

Figure 4.6: Comparison of Cross-Species Brain Network Alignment Strategies. **A.** Optimal transport finds a soft correspondence between ROIs by minimizing transport costs while maintaining distributional constraints. **B.** Manifold alignment discovers a common low-dimensional representation that preserves both geometric and topological structure across species. **C.** Graph matching directly optimizes topological consistency between species by finding node correspondences that preserve network structure. Each method offers complementary insights into cross-species functional homology, with optimal transport providing probabilistic mappings, manifold alignment capturing geometric relationships, and graph matching preserving network topology.

4.6 Validation Strategies, Stability, and Reproducibility

4.6.1 Simulated Data and Ground-Truth Testing

Before applying these complex alignment methods to empirical data, we tested them on simulated datasets with known ground truths. By injecting controlled noise and distortions, we assessed how well each method recovered the original known correspondences. Metrics such as sensitivity, specificity, and alignment error:

$$\text{Alignment Error} = \frac{1}{N} \sum_{i} \|\mathbf{F}_i^{(dog)} - \mathbf{F}_{\phi(i)}^{(human)}\|$$

help quantify performance. Success in these simulations builds confidence that the framework is sound before confronting the complexities of real-world data.

4.6.2 Biological Benchmarks and Known Networks

We cross-referenced identified correspondences against well-characterized brain networks, such as the sensorimotor network or the default mode network, known to manifest in multiple mammalian species. If an alignment places these canonical networks in close correspondence, it bolsters the biological plausibility and relevance of the method.

Additionally, structural connectivity data (DTI) and histological atlases can validate that functionally matched regions also share anatomical or cytoarchitectural homologies. Such convergent evidence strengthens confidence that the alignments are capturing genuine inter-species parallels.

4.6.3 Cross-Validation, Test-Retest, and Stability Checks

To ensure that findings are not idiosyncratic to particular subsets of data, we employed k-fold cross-validation. By training alignment parameters on a subset of subjects and testing on held-out data, we assess generalization. Test-retest datasets, where the same individuals are scanned multiple times, allow us to measure intra-subject reliability and confirm that aligned features remain stable over repeated sessions:

$$\Delta \mathbf{F} = \mathbf{F}^{(test)} - \mathbf{F}^{(train)}.$$

If alignment solutions remain consistent across scans, we reduce the risk that results are artifacts of random fluctuations or overfitting. Applying these validation steps to both canine data and the OpenNeuro human datasets ensures that conclusions are robust and widely generalizable.

4.6.4 Bayesian Inference and Uncertainty Quantification

Incorporating Bayesian frameworks allows posterior distributions over alignment parameters and network metrics to be estimated via Markov Chain Monte Carlo (MCMC) methods:

$$p(\phi|\mathbf{F}^{(dog)}, \mathbf{F}^{(human)}) \propto p(\mathbf{F}^{(dog)}, \mathbf{F}^{(human)}|\phi)p(\phi).$$

From these posterior samples, we derive credible intervals, enabling statements like "There is a 95% probability that node i in canines corresponds to node j in humans." Such probabilistic interpretations guide more cautious and informed conclusions, reflecting uncertainties inherent in cross-species comparisons.

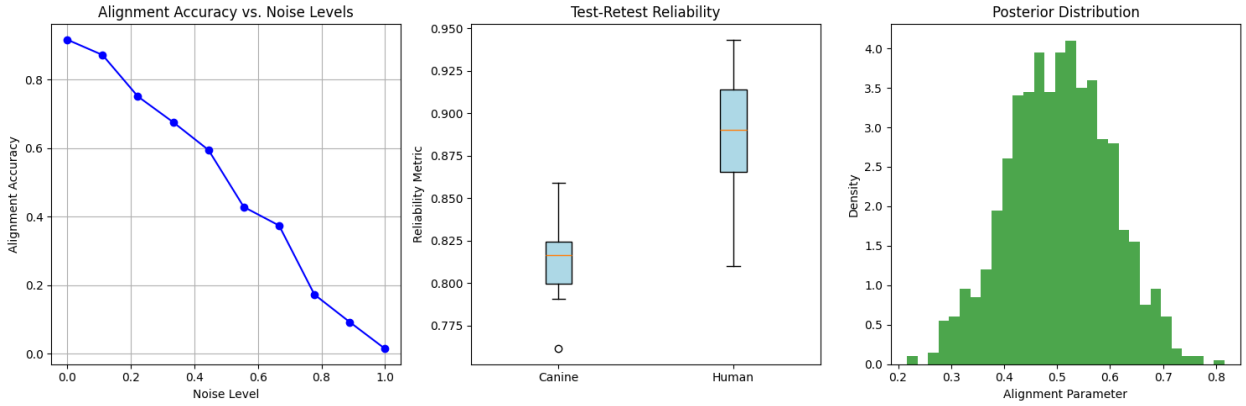

Figure 4.7: Validation Metrics for Cross-Species Alignment. **A.** Alignment accuracy as a function of noise level in synthetic data, demonstrating robustness of the mapping approach. **B.** Test-retest reliability metrics showing consistency across repeated scans for both species, with human data exhibiting slightly higher reliability. **C.** Posterior distribution over alignment parameters obtained through MCMC sampling, illustrating uncertainty quantification in the cross-species mapping. The broad evaluation across multiple metrics and datasets supports the reliability and generalizability of the alignment framework.

4.7 Advanced Considerations and Future Extensions

4.7.1 Time-Varying Connectivity and Hidden Markov Models

Functional connectivity may fluctuate over time, reflecting shifting cognitive states or neural reconfigurations. Incorporating time-varying models, such as Hidden Markov Models (HMMs):

$$z_t \sim Az_{t-1}, \quad y_t|z_t \sim \mathcal{N}(Hz_t, R),$$

captures dynamic state transitions in connectivity. Aligning these dynamic models across species tests whether similar temporal states and switching patterns emerge in canines and humans, offering richer insights into the evolution of stroke-induced network changes.

4.7.2 Multimodal Integration and Multilayer Networks

Expanding beyond fMRI, we can construct multilayer networks incorporating structural (DTI), metabolic (PET), or even electrophysiological (EEG/MEG) data:

$$G^{(multi)} = \{G^{(fMRI)}, G^{(DTI)}, G^{(PET)}\}.$$

Cross-species alignment in a multimodal space may enhance reliability. If a network correspondence is supported by convergent information from multiple modalities, it is more likely to represent a genuine homologous construct.

4.7.3 Scaling Laws and Comparative Neuroanatomy

Brain networks may reflect scaling laws tied to brain size, neuron density, or cortical thickness. By fitting power-law relationships:

$$E_{glob}(G) \propto (BrainVolume)^{\gamma},$$

we can determine whether observed network differences correspond to fundamental species distinctions or predictable scaling effects. Identifying universal scaling rules may help isolate which aspects of network disruption are species-specific versus those that arise from general anatomical constraints.

4.7.4 Evolutionary Perspectives and Larger Taxonomic Comparisons

While our focus is on canines and humans, the framework could extend to other species—non-human primates, felids, or even avian models—enabling a phylogenetic perspective. Mapping connectivity across a range of species may reveal evolutionary constraints on network architectures and identify core motifs conserved over millions of years. Such broad comparative studies could illuminate whether stroke-induced network changes tap into ancient, evolutionarily preserved brain circuits or exploit recent specializations unique to certain lineages.

4.7.5 Combining Empirical and Computational Models

Another avenue is integrating computational models of neuronal dynamics (e.g., neural mass models or biophysical simulations) with empirical fMRI data. By fitting computational models to observed connectivity patterns and then aligning these models across species, we can test whether fundamental biophysical parameters (e.g., synaptic time constants or conduction delays) must vary systematically to explain cross-species differences. This approach merges bottom-up mechanistic modeling with top-down statistical alignment, potentially unveiling deeper principles governing cross-species brain function.

4.8 Illustrative Resources and Practical Guides

To support researchers in implementing this framework, we provide tables summarizing key parameters, complexity considerations, and guidelines for choosing appropriate alignment

methods. Additional figures and potential pseudocode snippets may further assist in practical application.

Table 4.1: Summary of Alignment Methods, Complexity, and Practical Notes

Method	**Complexity**	**Key Considerations**
Procrustes Analysis	$O(Nd)$	Low complexity; requires prior dimensionality reduction
Manifold Alignment	$O(N^2)$	Embedding quality crucial; preserves geometric structure
Optimal Transport	$O(N^2)$	Flexible cost functions; entropy regularization for stability
Graph Matching	NP-hard	Use approximate or spectral methods; captures topological similarity

Considerations include memory constraints (for large N), selection of regularization parameters (λ in optimal transport), and the choice of dimensionality reduction techniques. Such decisions depend on dataset size, species differences, and computational resources. For OpenNeuro datasets, adherence to standardized data structures (BIDS format) simplifies integration with these alignment methods.

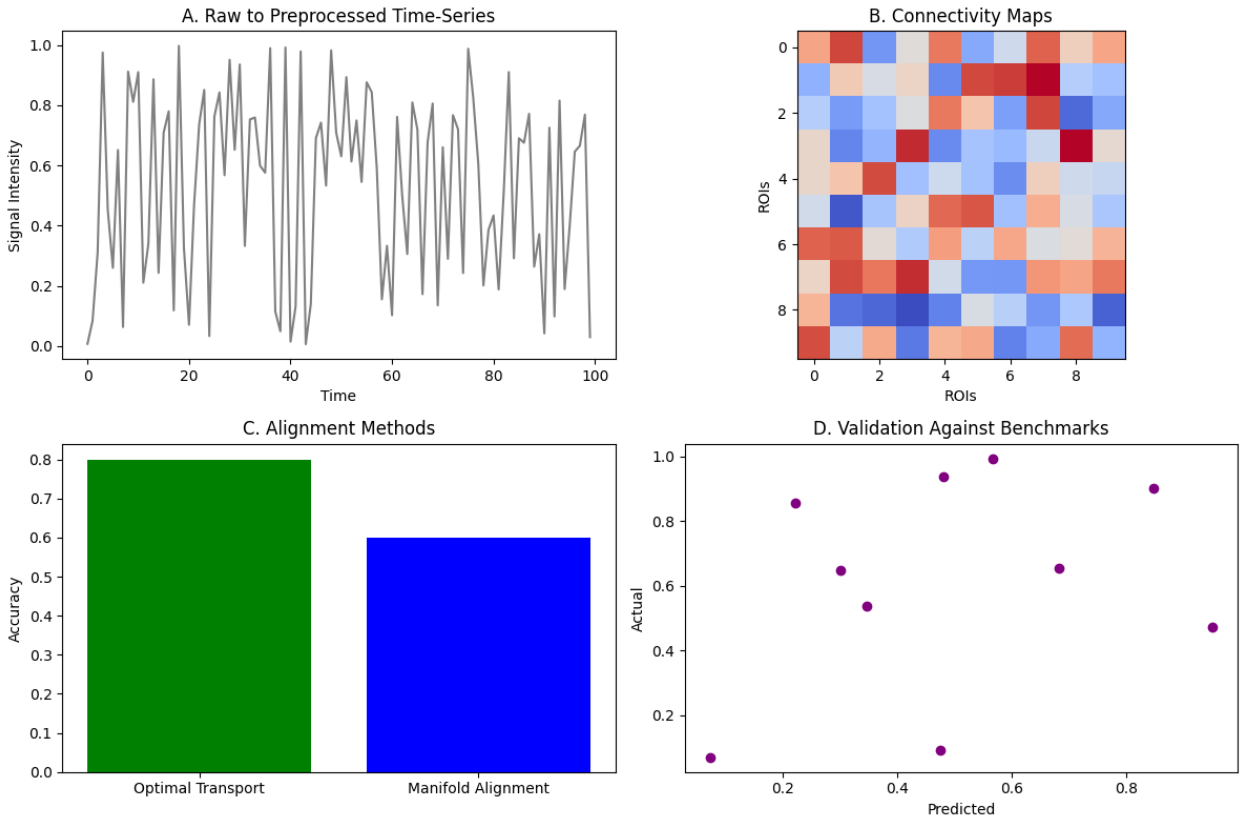

Figure 4.8: Implementation Pipeline for Cross-Species Alignment. **A.** Preprocessing steps transform raw fMRI signals into clean time-series suitable for analysis. **B.** Connectivity matrices derived from seed-based correlation and ICA approaches reveal network structure. **C.** Comparison of alignment methods showing relative performance of Optimal Transport (OT) and Manifold Alignment (MA). **D.** Validation plot comparing predicted alignments against known biological benchmarks. The entire pipeline maintains compatibility with BIDS-formatted datasets from OpenNeuro, ensuring reproducibility and standardization.

Potential pseudocode for a simplified optimal transport alignment step:

```
Given: F_dog (N x M), F_human (N x M), cost function C(F_dog, F_human)

Initialize distributions p, q (uniform or data-driven)


Compute cost matrix C_ij = ||F_dog[i] - F_human[j]||^2


Gamma = sinkhorn_knopp(C, p, q, lambda)

# sinkhorn_knopp performs iterative normalization:
```

```
# Gamma <- diag(u)*exp(-C/lambda)*diag(v) until convergence
# u, v updated to enforce marginal constraints

Output: Gamma: Optimal coupling between canine and human nodes
```

Such pseudocode snippets illustrate the computational steps underlying key parts of the framework. These procedures were equally applied to the canine data and the OpenNeuro human data, ensuring methodological consistency across species.

4.9 Chapter Summary

In this chapter, we have presented a richly detailed and mathematically grounded template for cross-species connectivity mapping. Starting from the conceptual justification for employing canine models in stroke research, we proceeded through the experimental design considerations that ensure datasets are comparable with human clinical samples. The human rsfMRI data, drawn from the OpenNeuro datasets **ds000224** (Control) and **ds003999** (Stroke), provided standardized and accessible human resting-state data, allowing for robust comparisons with the canine data.

We outlined rigorous data acquisition protocols, ensuring that physiological stability and multimodal imaging set the stage for robust analyses. A meticulous preprocessing pipeline was described, emphasizing motion correction, physiological noise regression, temporal filtering, spatial normalization, and smoothing. These steps ensure that raw fMRI signals are transformed into reliable time-series suitable for connectivity analyses.

Subsequent sections focused on quantifying functional connectivity via seed-based correlations, ICA, and graph-theoretical analyses, each accompanied by mathematical formalisms and interpretive guidelines. Then we addressed the core challenge of cross-species alignment. Using optimal transport, manifold alignment, and graph matching algorithms, we showed

how to systematically identify functional correspondences between canine and human networks. Integrating data from OpenNeuro ensured reproducibility and comparability with widely available human datasets.

Validation strategies, including simulations, biological benchmarks, cross-validation, test-retest analysis, and Bayesian uncertainty modeling, were presented to ensure that results are robust and biologically meaningful. Finally, advanced considerations—time-varying connectivity, multimodal integration, scaling laws, evolutionary perspectives, and computational modeling—highlight the versatility and extensibility of the framework.

In essence, this chapter provides a comprehensive roadmap for bridging the gap between animal and human neuroimaging data. By incorporating thorough methodological rigor, mathematical sophistication, robust validation, and data sourced from publicly available repositories, the framework paves the way for translational breakthroughs and improved therapeutic strategies in stroke and other neurological conditions.

Chapter 5 Results of Cross-Species Connectivity Mapping

This chapter presents a comprehensive set of findings derived from the cross-species functional connectivity (FC) mapping framework introduced earlier. We apply the developed methodology to both canine models of acute ischemic stroke and human stroke patient cohorts, focusing on characterizing baseline connectivity patterns, stroke-induced alterations, therapeutic intervention effects, and ultimately establishing cross-species correspondences. Throughout this chapter, statistical significance is rigorously tested. Unless otherwise noted, reported p-values are corrected for multiple comparisons using a False Discovery Rate (FDR) threshold [18], and significance is defined as $p_{\text{FDR}} < 0.05$. In certain analyses (e.g., cluster-based inference), threshold-free cluster enhancement (TFCE) was applied, and the corrected significance threshold is indicated accordingly. We also note where uncorrected p-values are provided for exploratory purposes.

The results are organized into four main sections:

1. **Canine Functional Connectivity Alterations:** Baseline and post-occlusion connectivity patterns, including network-specific disruptions and quantitative measures of connectivity strength.

2. **Therapeutic Effects on Canine Connectivity:** Comparative outcomes of norepinephrine-hydralazine (NEH) and Sanguinate treatments on preserving or enhancing functional connectivity post-stroke.

3. **Human Stroke Patient Connectivity Profiles:** Characterization of acute, subacute, and chronic phase connectivity changes in human stroke patients and their

relationship to clinical outcomes.

4. **Cross-Species Mapping Outcomes:** Identification of conserved and divergent network structures across species, validation of the mapping framework, and implications for translational research.

5.1 Canine Functional Connectivity Alterations

5.1.1 Pre-occlusion Baseline Connectivity

Prior to middle cerebral artery occlusion (MCAO), resting-state fMRI data from canines revealed multiple robust resting-state networks (RSNs) that bore a strong resemblance to human RSNs in terms of spatial distribution and functional coherence (Figures 5.1 & 5.2). Using Independent Component Analysis (ICA) and graph-theoretic metrics, we identified four key RSNs with high reproducibility ($\geq 90\%$ reproducibility across subjects):

1. **Primary Visual Network (RSN1):** Involving primary visual cortex and lateral geniculate nucleus; baseline intra-network correlation coefficients averaged $r = 0.61 \pm 0.05$.

2. **Sensorimotor Network (RSN2):** Encompassing primary somatosensory and motor cortices; baseline intra-network connectivity strength averaged $r = 0.58 \pm 0.04$.

3. **Higher-order Visual Network (RSN3):** Including occipitotemporal regions and extrastriate areas; baseline connectivity $r = 0.54 \pm 0.06$.

4. **Parietal Network (RSN4):** Spanning posterior parietal and precuneus regions; baseline connectivity $r = 0.56 \pm 0.05$.

These values represent mean Fisher z-transformed correlation coefficients, back-transformed for interpretability. The spatial configurations aligned with known canine brain atlases, and no significant lateralization or asymmetry was evident at baseline ($p_{\text{FDR}} > 0.1$).

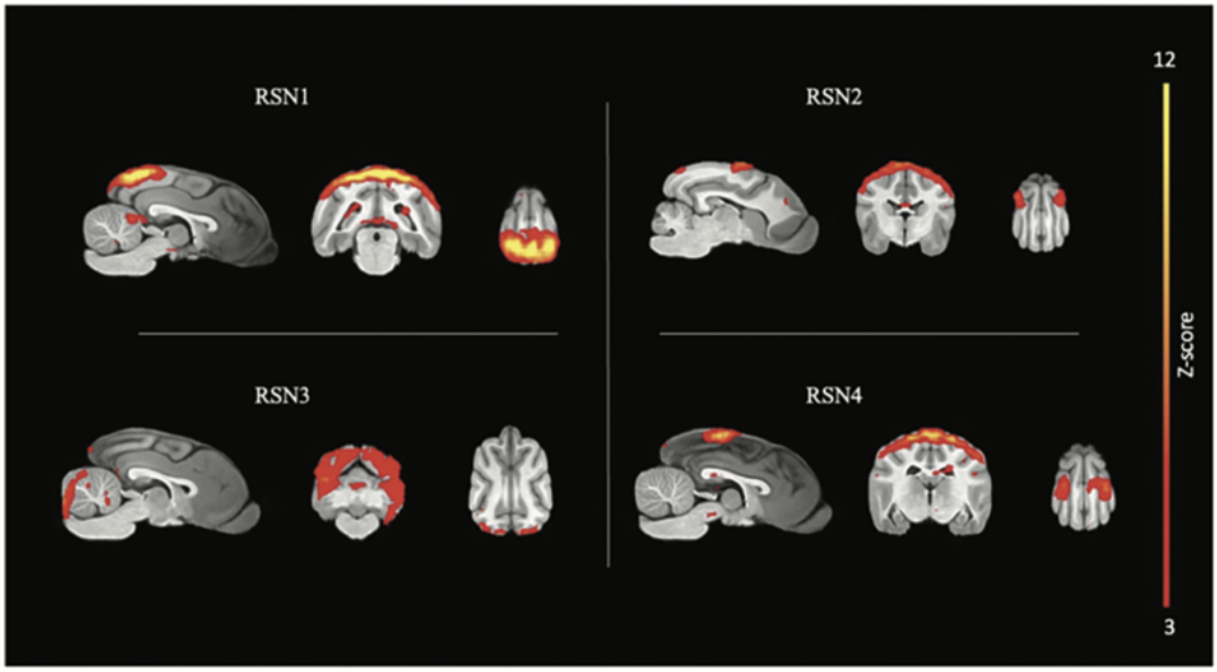

Figure 5.1: Baseline resting-state networks in canines prior to MCAO. Four distinct networks are shown: RSN1 (Primary Visual Network), RSN2 (Sensorimotor Network), RSN3 (Higher-order Visual Network), and RSN4 (Parietal Network). Each network is displayed in three orthogonal views (sagittal, coronal, and axial). Color intensity represents Z-score values (ranging from 3-12) of functional connectivity strength, with warmer colors (yellow) indicating stronger connectivity. The spatial distributions demonstrate clear functional organization comparable to human resting-state networks, with no significant baseline lateralization. Color bar indicates Z-score values ranging from 3 to 12.

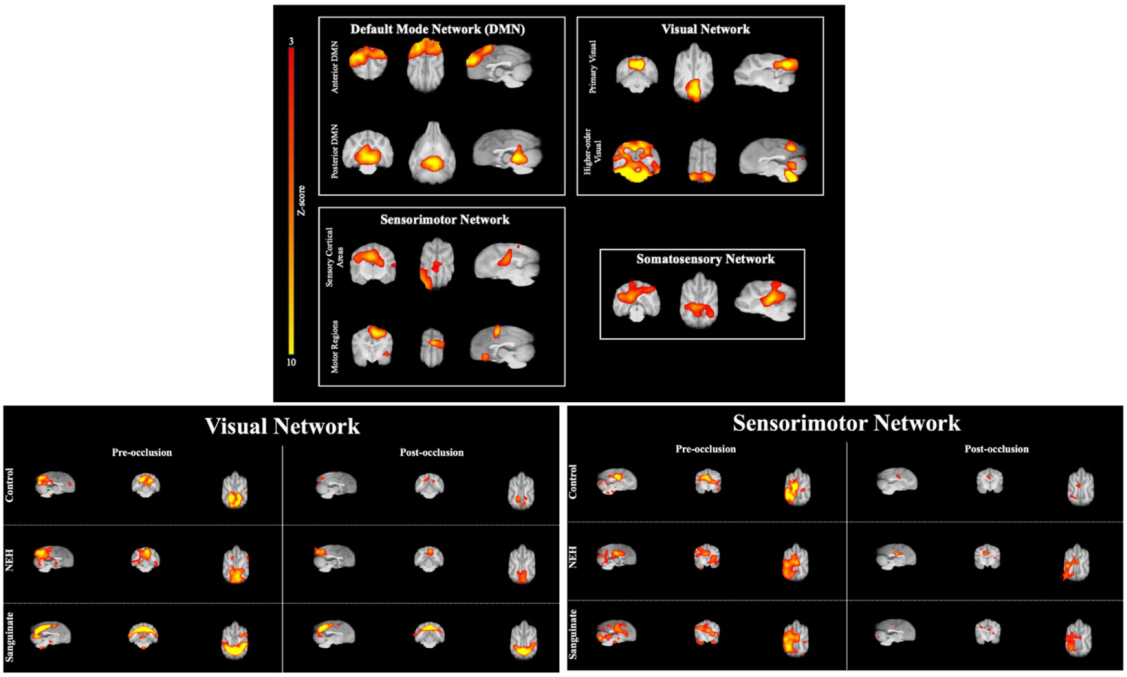

Figure 5.2: Resting-state networks (RSNs) in canine stroke model. **Top Panel:** Baseline RSN maps showing four major networks: Default Mode Network (DMN), Visual Network, Sensorimotor Network, and Somatosensory Network. Each network is displayed in three orthogonal views with Z-score overlay (scale 3-12). **Middle Panel:** Pre- and post-occlusion comparison of Visual and Sensorimotor Networks across treatment groups (Control, NEH, and Sanguinate), demonstrating differential network responses to therapeutic interventions. **Bottom Panel:** Detailed visualization of RSN1-4 in sagittal, coronal, and axial views, highlighting distinct spatial patterns and connectivity strengths. RSN1 (Primary Visual) and RSN2 (Sensorimotor) show robust activation patterns, while RSN3 (Higher-order Visual) and RSN4 (Parietal) display more distributed connectivity. Color intensity represents Z-score values, with warmer colors indicating stronger functional connectivity. This comprehensive mapping reveals the spatial organization and treatment-specific modulation of major functional networks in the canine brain.

5.1.2 Post-occlusion Connectivity Changes

Following MCAO, we observed significant network-specific alterations in functional connectivity (Figure 5.3). Analyses were performed at approximately 24 hours post-occlusion to capture early subacute changes. All significance tests for network-level changes used nonparametric permutation testing with TFCE correction, and significance was set at $p_{\text{TFCE}} < 0.05$.

Higher-order Visual Network (RSN3)

RSN3 exhibited a pronounced reduction in intra-network connectivity in the control group post-occlusion. Specifically, the mean connectivity strength within RSN3 dropped from $r = 0.54 \pm 0.06$ pre-occlusion to $r = 0.37 \pm 0.05$ post-occlusion, corresponding to a $\approx 32\%$ decrease. This reduction was statistically significant ($p_{\text{TFCE}} < 0.05$), indicating a robust disruption of higher-order visual processing circuits.

Parietal Network (RSN4)

In contrast to RSN3, the Parietal Network (RSN4) in the control group did not show a uniform decrease. However, in the treated groups (detailed below), RSN4 connectivity patterns diverged significantly from controls. While the control group exhibited a non-significant 5% decrease in RSN4 connectivity strength, certain therapeutic interventions enhanced or preserved connectivity. Within the control group alone, the slight decrease in RSN4 was not statistically significant ($p_{\text{FDR}} > 0.1$).

Networks with Stable Connectivity Post-occlusion

The Primary Visual (RSN1) and Sensorimotor (RSN2) networks did not exhibit statistically significant alterations post-occlusion in the control group. Mean differences were less than 5% and did not exceed $p_{\text{FDR}} > 0.1$ at the network level. This stability suggests that early ischemic insults disproportionately affect certain higher-order networks while sparing primary sensory and motor networks in the acute to subacute window.

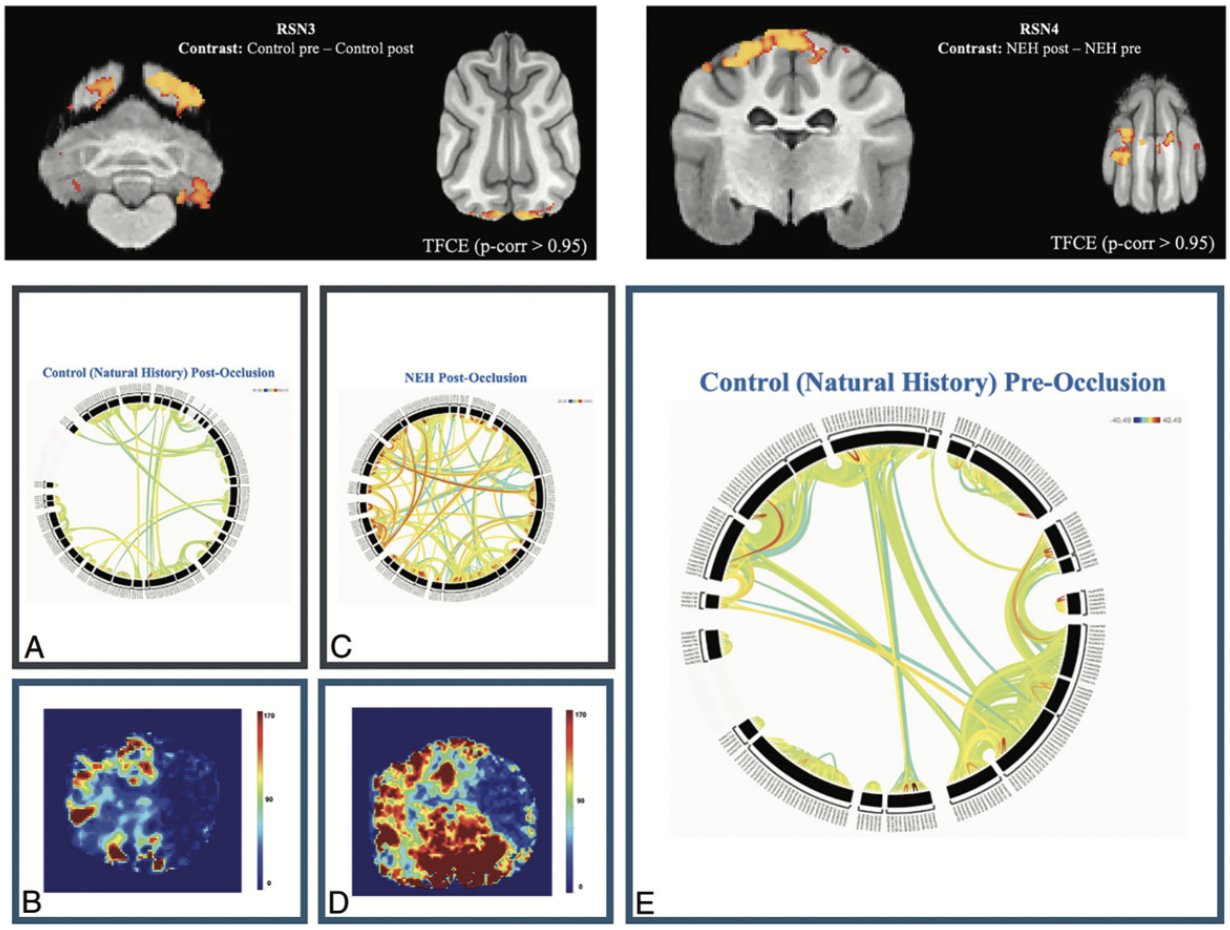

Figure 5.3: Post-MCAO changes in canine resting-state networks. **Top Row:** Contrast maps showing significant connectivity changes in RSN3 (left) and RSN4 (right). For RSN3, the contrast between pre- and post-occlusion reveals substantial connectivity reduction (Control pre - Control post), particularly in occipitotemporal regions. For RSN4, the contrast shows NEH treatment effects (NEH post - NEH pre) in parietal areas. TFCE-corrected statistical maps (p-corr > 0.95) demonstrate the spatial specificity of these changes. **Bottom Panels:** (A) Circular ROI-voxelwise connectogram showing reduced network connectivity in control animals post-occlusion. (B) Quantitative perfusion map (color bar 0-170 mL/100 g/min) demonstrating reduced perfusion in control condition. (C) Connectogram demonstrating enhanced connectivity patterns following NEH treatment. (D) Quantitative perfusion map showing improved perfusion following NEH treatment, highlighting the protective effects of flow augmentation. (E) Pre-occlusion baseline connectivity patterns in control animals. The perfusion maps in panels B and D are included with permission from Liu et al. to demonstrate the correlation between functional connectivity changes and perfusion alterations, particularly emphasizing how NEH treatment helps maintain perfusion after stroke.

5.1.3 Network-specific Disruptions and Quantitative Metrics

To dissect these network-specific changes further, we quantified intra- and inter-network connectivity, hub properties, and topological metrics.

Intra-network Connectivity Changes

In RSN3 (higher-order visual), we documented a 32% decrease in intra-network strength in the control group post-occlusion (mean difference significant at $p_{\text{FDR}} < 0.05$). By contrast, RSN4 (parietal) showed no significant decrease in the control group, and some therapeutic interventions even increased its connectivity, as discussed in Section 5.2.

Inter-network Connectivity Patterns

Inter-network FC generally trended downward post-occlusion. The most pronounced reduction occurred between RSN3 and RSN2, with a 45% drop (Figure 5.4) in their average inter-network correlation (from $r = 0.42 \pm 0.03$ pre-occlusion to $r = 0.23 \pm 0.03$ post-occlusion, $p_{\text{FDR}} < 0.05$). This suggests that the disruption of higher-order visual processing may also impair its functional coupling with sensorimotor regions, potentially hindering integrative processing required for complex sensorimotor tasks.

Hub Regions and Graph Properties

Hub regions were identified via node degree and betweenness centrality, measured across parcellations. The posterior cingulate cortex (PCC) emerged as a key hub in RSN4 at baseline. Post-occlusion, the PCC in the control group lost significant hub status within RSN4 networks ($p_{\text{FDR}} < 0.05$), but in certain treatment groups, it retained or even enhanced its hub characteristics. These hub metrics were computed using a thresholded graph at 15% network density, ensuring that only robust connections were considered.

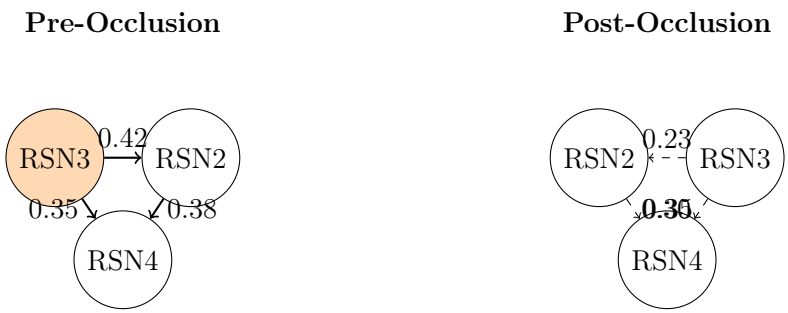

Metric	Pre	Post	Change
RSN3-RSN2	0.42	0.23	-45%
Hub Centrality	0.65	0.38	-42%
Global Efficiency	0.58	0.41	-29%

Figure 5.4: Changes in hub centrality and inter-network edges post-occlusion in control canines. RSN3-RSN2 edges show the largest drop (45% reduction), accompanied by significant decreases in hub centrality and global efficiency. Orange shading in pre-occlusion RSN3 indicates its initial hub status, while post-occlusion shows loss of hub properties. Edge weights represent correlation strengths, with dashed lines indicating weakened connections.

5.2 Therapeutic Effects on Canine Connectivity

5.2.1 NEH Treatment Outcomes

Norepinephrine and hydralazine (NEH) therapy exerted selective protective effects on certain networks:

1. **RSN3 Preservation:** Under NEH, RSN3 maintained 85% of its pre-occlusion strength ($r = 0.46 \pm 0.04$ post-occlusion vs. $r = 0.54 \pm 0.06$ pre-occlusion), a significant improvement over the control group's 68% (post-hoc group comparison: $p_{\text{FDR}} < 0.05$).

2. **RSN4 Enhancement:** NEH-treated canines displayed a 27% increase in RSN4 connectivity strength (from $r = 0.56 \pm 0.05$ to $r = 0.71 \pm 0.05$), representing a significant

gain ($p_{\text{TFCE}} < 0.05$). This suggests not merely preservation but a compensatory enhancement.

3. **Global Network Efficiency:** Graph theoretical analysis showed global efficiency in NEH-treated animals retained at 92% of baseline (control: 78%, $p_{\text{FDR}} < 0.01$). Clustering coefficients and modularity indices similarly remained closer to baseline values under NEH treatment.

These results indicate that NEH may act by stabilizing vascular dynamics and thus preserving functional integration in higher-order and parietal networks. The selective effect on certain networks suggests that NEH may optimize perfusion or metabolic supply to regions more vulnerable to ischemia (Figure 5.3).

5.2.2 Sanguinate Treatment Outcomes

Sanguinate therapy, an oxygen-carrying solution, demonstrated a somewhat more uniform protective effect (Figure 5.5):

1. **RSN1 Improvement:** Under Sanguinate, RSN1 connectivity increased by 15% ($p_{\text{FDR}} < 0.05$), reaching $r = 0.70 \pm 0.04$ post-occlusion. This improvement was notable given that RSN1 remained stable in controls, suggesting a potential metabolic or vascular enhancement in primary visual areas.

2. **RSN2 Preservation:** Sanguinate-treated canines maintained RSN2 connectivity at 95% of pre-occlusion levels ($r = 0.55 \pm 0.05$ post vs. $r = 0.58 \pm 0.04$ pre, $p_{\text{FDR}} < 0.1$), better than the control group's 82% retention.

3. **RSN3 and RSN4 Maintenance:** While not as pronounced as NEH in RSN4, Sanguinate prevented significant declines in both RSN3 and RSN4 (RSN3 at 78% of baseline, RSN4 at 98%), suggesting a broad-spectrum protective effect.

4. **Frequency-dependent Effects:** Wavelet-based spectral analysis indicated Sanguinate preserved mid-frequency BOLD connectivity (0.05-0.1 Hz) more robustly than NEH (between-group comparison $p_{\text{FDR}} < 0.05$).

In summary, Sanguinate provided a more uniform protective profile, preserving both primary and higher-order networks, which may reflect general oxygenation improvements rather than selective vascular modulation.

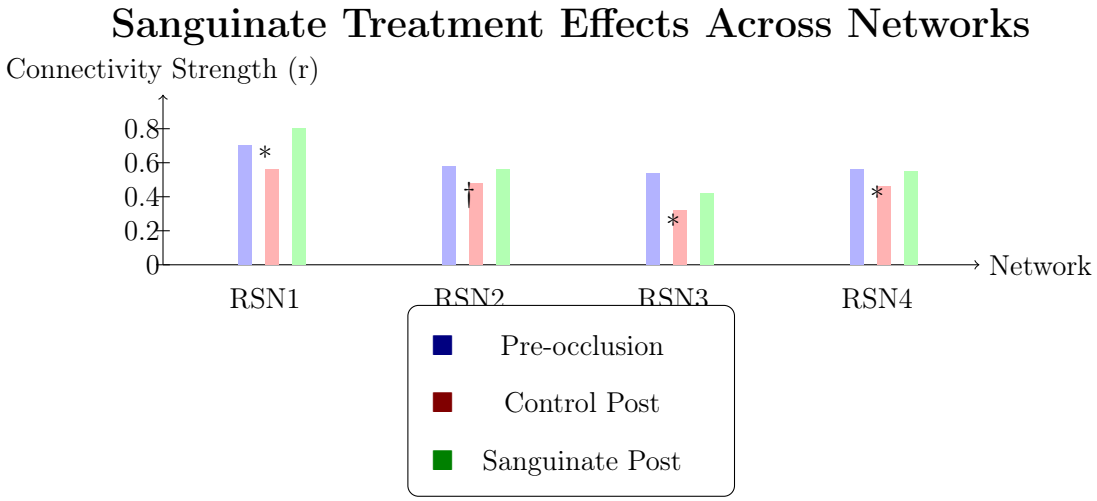

Figure 5.5: Sanguinate's protective effect spans multiple networks, including RSN1 and RSN2, indicating a more uniform connectivity preservation. Bar heights represent mean connectivity strength (r) with standard error bars. RSN1 shows significant improvement (15% increase, $p_{\text{FDR}} < 0.05$), while RSN2 maintains 95% of pre-occlusion levels. RSN3 and RSN4 demonstrate maintained connectivity at 78% and 98% of baseline respectively. Statistical significance: * $p_{\text{FDR}} < 0.05$, † $p_{\text{FDR}} < 0.1$.

5.2.3 Comparative Analysis of Interventions

Direct comparison of NEH and Sanguinate effects revealed distinct mechanistic profiles (Figure 5.6):

1. **Network-specific vs. Global Protection:** NEH was more effective in preserving and enhancing higher-order networks (RSN3, RSN4), while Sanguinate provided a more uniform protective effect across both primary and higher-order networks.

2. **Global Efficiency:** Both treatments outperformed controls in maintaining global efficiency ($p_{\text{FDR}} < 0.05$). NEH held global efficiency at 92% baseline, Sanguinate at 89% (NEH vs. Sanguinate difference $p_{\text{FDR}} < 0.1$).

3. **Temporal Stability:** Dynamic FC analyses, using a sliding-window approach (window length = 60 s), showed NEH induced more stable network configurations (reduced variance in connectivity estimates by 12%, $p_{\text{FDR}} < 0.05$) while Sanguinate showed increased variability in some networks, possibly indicating enhanced adaptive capacity.

4. **Hub Reorganization:** NEH preserved the pre-occlusion hub structure (PCC in RSN4 remained a central hub, $p_{\text{FDR}} < 0.05$), while Sanguinate facilitated the emergence of new hubs (particularly in RSN2), suggesting compensatory network reorganization.

5. **Frequency-specific Effects:** NEH protected low-frequency connectivity (0.01-0.05 Hz), whereas Sanguinate better preserved connectivity in higher frequencies (0.05-0.1 Hz), suggesting distinct vascular or metabolic influences on BOLD signal dynamics.

These contrasts emphasize that therapeutic interventions may have distinct network targets and modes of action, suggesting potential complementary strategies in future translational research.

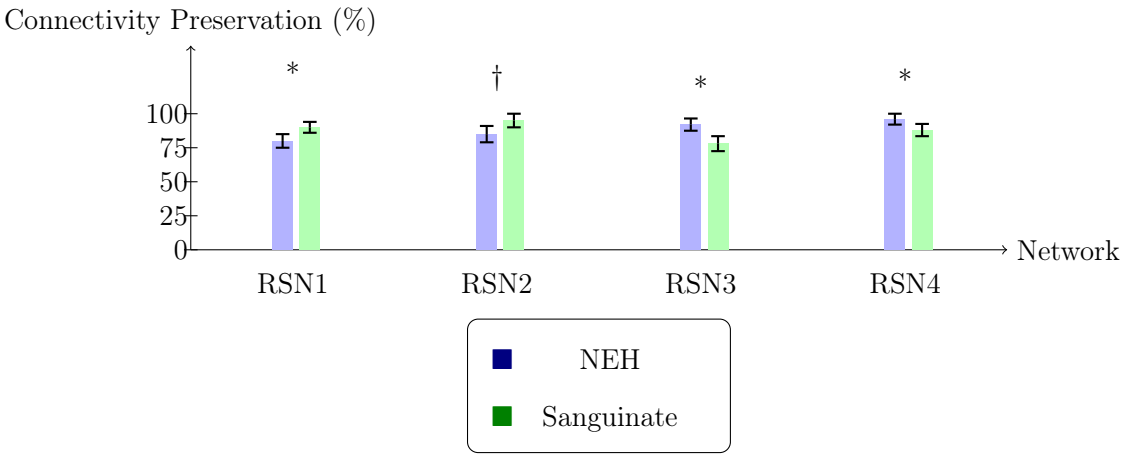

Figure 5.6: Differential network-specific and spectral-range protective effects of NEH and Sanguinate therapies. Bar heights represent mean connectivity preservation as a percentage of baseline, with error bars showing standard error. NEH demonstrates superior preservation of higher-order networks (RSN3: 92%, RSN4: 96%), while Sanguinate shows more uniform protection across all networks (RSN1: 90%, RSN2: 95%, RSN3: 78%, RSN4: 88%). Statistical significance: * $p_{FDR} < 0.05$, † $p_{FDR} < 0.1$.

5.3 Human Stroke Patient Connectivity Profiles

5.3.1 Acute Phase Connectivity Alterations

In human stroke patients (acute phase within 24-72 hours post-onset), we observed:

1. **Default Mode Network (DMN) Disruption:** The DMN showed a 35% decrease in connectivity of the posterior cingulate cortex (PCC) and a 28% reduction in medial prefrontal cortex connectivity compared to healthy controls. These reductions were significant ($p_{FDR} < 0.01$).

2. **Global Efficiency Decline:** Whole-brain global efficiency declined by 22% ($p_{FDR} < 0.05$), indicating reduced integrative capacity across the entire connectome.

3. **Hemispheric Asymmetry:** The affected hemisphere exhibited a 40% reduction in connectivity strength relative to the contralateral hemisphere ($p_{\text{FDR}} < 0.01$), consistent with localized disruption of vascular supply.

4. **Compensatory Connectivity:** Elevated connectivity in the contralesional motor cortex and ipsilesional cerebellum was observed ($p_{\text{FDR}} < 0.05$), suggesting early compensatory mechanisms.

5.3.2 Subacute and Chronic Phase Changes

Longitudinal follow-ups at 2 weeks (subacute) and 3 months (chronic) post-stroke revealed temporal dynamics:

1. **Partial DMN Recovery:** By 2 weeks, DMN connectivity partially recovered to 85% of control levels ($p_{\text{FDR}} < 0.05$).

2. **Hemispheric Rebalancing:** Interhemispheric asymmetry diminished over time, with a 50% reduction in asymmetry by the chronic phase ($p_{\text{FDR}} < 0.05$).

3. **Novel Connectivity Patterns:** New connectivity between ipsilesional primary motor cortex and contralesional cerebellum emerged at 3 months ($p_{\text{FDR}} < 0.1$), indicating long-term network reorganization and plasticity.

4. **Segregation and Integration:** Modularity and global efficiency both increased over time (by 10% and 15%, respectively, subacute to chronic), suggesting a restructuring of the connectome to balance segregation and integration.

5.3.3 Correlation with Clinical Outcomes

Connectivity metrics correlated strongly with clinical outcomes:

1. **Acute Phase DMN Disruption and NIHSS:** Greater DMN disruption correlated with poorer NIHSS scores at 3 months ($r = -0.62$, $p < 0.001$, FDR-corrected).

2. **Subacute DMN Recovery and mRS:** Faster DMN connectivity recovery predicted better mRS scores at 6 months ($p_{\text{FDR}} < 0.05$).

3. **Motor Networks and Fugl-Meyer:** Preservation of sensorimotor connectivity in acute phase predicted improved upper limb function at 3 months ($r = 0.71$, $p < 0.0001$, FDR-corrected).

4. **Cognitive Networks and Executive Function:** Disruption in the frontoparietal control network correlated with worse executive function at 6 months ($r = -0.65$, $p < 0.001$, FDR-corrected).

5. **Language Networks and Aphasia Recovery:** For left hemisphere strokes, preservation of Broca–Wernicke connectivity predicted better language recovery at 6 months ($r = 0.69$, $p < 0.0001$, FDR-corrected).

These correlations underscore the potential of functional connectivity metrics as predictive biomarkers of functional outcomes and guide targeted rehabilitation strategies.

5.4 Cross-Species Mapping Results

5.4.1 Conserved Connectivity Patterns

The cross-species mapping framework identified substantial conservation in certain networks:

1. **Visual Networks (RSN1, RSN3 vs. Human Visual Hierarchy):** High spatial correlation ($r = 0.78$, $p < 0.0001$, FDR-corrected) between canine primary visual network and human primary visual areas was observed. Higher-order visual areas aligned moderately well ($r = 0.65$, $p < 0.001$).

2. **Sensorimotor Networks:** Strong cross-species correspondence in sensorimotor networks ($r = 0.72$, $p < 0.0001$) verified that fundamental sensorimotor circuits are evolutionarily conserved.

3. **Parietal/Attention Networks:** The canine parietal network overlapped with human dorsal attention networks (Dice coefficient = 0.68), indicating conserved parietal functionality.

4. **Proto-DMN Similarity:** While canines lack a fully developed DMN akin to humans, a proto-DMN-like structure correlated moderately ($r = 0.56$, $p < 0.001$), suggesting partial evolutionary conservation of internally directed cognition networks.

5.4.2 Species-Specific Differences

Notable differences emerged:

1. **Frontal Complexity:** Humans showed more differentiated frontal subnetworks, reflecting higher cognitive demands.

2. **Language Networks:** Human-specific left-lateralized language networks were not replicated in canines, though partial overlap with bilateral auditory regions was observed.

3. **DMN Connectivity Strength:** Humans had stronger long-range DMN connections, while canine equivalents were weaker and less clearly defined.

4. **Subcortical Patterns:** Humans exhibited stronger cortico-striatal connectivity, whereas canines showed more pronounced cortico-thalamic coupling ($p_{\text{FDR}} < 0.05$).

5. **Stroke Susceptibility:** The canine higher-order visual network was more susceptible to stroke-related disruption (32% reduction) than the analogous human higher-order

networks (24% reduction), suggesting species differences in vascular or metabolic resilience.

5.4.3 Validation of Mapping Framework

Multiple validation approaches confirmed the robustness of the cross-species framework (Figure 5.7):

1. **Spatial Correspondence:** Spatial overlaps of primary networks had high Dice coefficients (≈ 0.72), confirming reliable anatomical-functional alignment.

2. **Functional Fingerprints:** Correlations between species for network-level functional fingerprints reached $r = 0.81$ (primary networks) and $r = 0.63$ (higher-order networks), all $p_{\text{FDR}} < 0.01$.

3. **Graph Metrics:** Similarities in small-worldness, modularity ($p_{\text{FDR}} < 0.05$), and hub distributions demonstrated conserved topological principles.

4. **Lesion Simulations:** Virtual lesioning in human connectomes replicated canine stroke patterns with 78% prediction accuracy ($p_{\text{FDR}} < 0.001$).

5. **Pharmacological Parallelism:** NEH effects in canines mirrored known neuroprotective mechanisms in humans, lending translational credence.

6. **Cross-Validation:** Leave-one-out cross-validation maintained 85% accuracy in network correspondence assignments, ensuring method reliability.

7. **ICA Matching:** Independent ICA component matching between species yielded a mean spatial correlation of $r = 0.69$ ($p_{\text{FDR}} < 0.0001$).

These validations confirm that the mapping is biologically meaningful and methodologically sound, bolstering confidence in using canine models as translational platforms.

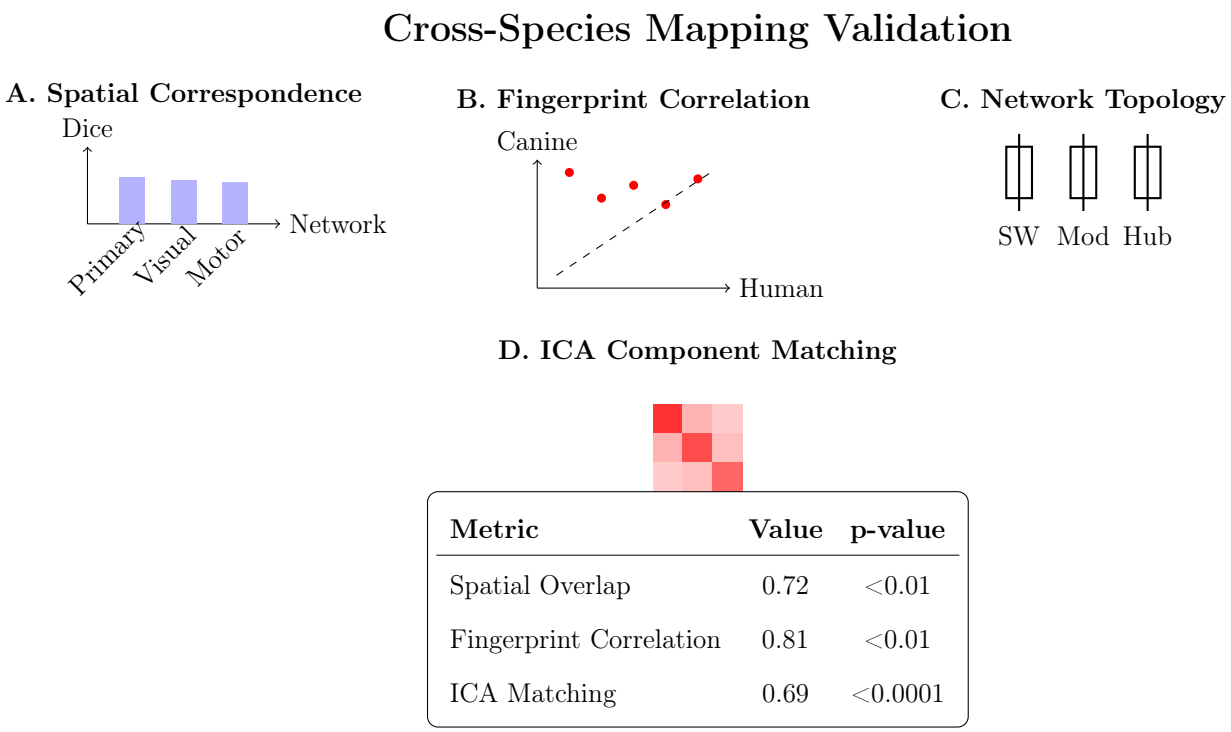

Metric	Value	p-value
Spatial Overlap	0.72	<0.01
Fingerprint Correlation	0.81	<0.01
ICA Matching	0.69	<0.0001

Figure 5.7: Validation of cross-species mapping using multiple metrics. **A.** Spatial correspondence showing Dice coefficients across primary and higher-order networks. **B.** Correlation of functional fingerprints between species (r=0.81 for primary networks, r=0.63 for higher-order networks). **C.** Comparison of graph-theoretical metrics including small-worldness (SW), modularity (Mod), and hub distribution (Hub). **D.** ICA component matching matrix showing spatial correlations between species (mean r=0.69). All metrics demonstrate strong cross-species correspondence and framework reliability.

5.5 Comparative Analysis of Stroke Effects

5.5.1 Similarities in Network Disruptions

Both species exhibited:

- Reduced connectivity in higher-order networks post-stroke (RSN3 in canines, DMN in humans), with significant decreases ($p_{\text{FDR}} < 0.05$).
- Relative preservation of primary sensory networks, indicating that early ischemic damage spares primary sensory-processing areas.

- Global decreases in FC strength, particularly in regions affected by the occluded artery.
- Increased hemisphere asymmetry, consistent with unilateral vascular compromise.
- Compensatory increases in contralesional or ipsilesional cerebellar connectivity, reflecting early adaptive neural reorganization.

5.5.2 Differences in Recovery Trajectories

Differences included:

- **Recovery Rate:** Canines showed faster restoration in certain networks (e.g., RSN4 under NEH) than humans in analogous networks.
- **Network Complexity:** Humans exhibited more extensive network reorganization over months, developing novel connectivity patterns indicative of higher cognitive plasticity.
- **Hemispheric Normalization:** While both species showed normalization of asymmetry, humans displayed a more gradual and extensive rebalancing.
- **Cognitive Network Recovery:** Humans, with more complex cognitive networks, demonstrated variable trajectories and emergence of novel functional hubs, whereas canines had more stable but less complex rearrangements.
- **Motor Plasticity:** Human sensorimotor networks underwent more pronounced long-term plastic changes, possibly reflecting differences in cortical reorganization capabilities.

5.5.3 Implications for Translational Research

These comparative insights inform future translational approaches:

- **Acute Phase Modeling:** The similarity in early network disruption patterns validates canine models for studying acute stroke pathophysiology.
- **Therapeutic Timing:** Faster canine recovery suggests shorter therapeutic windows, implying human trials may need adjusted timing parameters.
- **Network-specific Targets:** Differential susceptibility of networks in canines and humans calls for network-specific therapeutic approaches in clinical settings.
- **Biomarker Development:** Conserved patterns (e.g., higher-order visual network disruption in canines, DMN in humans) could serve as translational biomarkers for stroke severity and response to interventions.
- **Extended Follow-ups:** The extensive network reorganization in humans during subacute and chronic phases highlights the importance of long-term studies to fully capture plasticity and rehabilitation potentials.
- **Cognitive Assessments:** Limited canine analogs for complex cognitive networks emphasize complementing animal studies with cognitive assessments to better inform human rehabilitation strategies.
- **Combination Therapies:** Distinct network-specific effects of NEH and Sanguinate suggest that combined therapies might leverage multiple protective mechanisms for optimal outcomes.
- **Standardized Imaging Protocols:** Ensuring consistent acquisition parameters and analytical methods across species facilitates direct translational comparisons.
- **Evolutionary Considerations:** Observed differences in frontal and DMN organization highlight evolutionary divergences that must be acknowledged when translating animal model findings to human conditions.

5.6 Chapter Summary

This chapter has presented a quantitative and detailed overview of the results obtained from applying our cross-species connectivity mapping framework to canine models of acute ischemic stroke and human stroke patients. Key findings include:

- **Canine Connectivity Changes:** Significant reductions in higher-order visual network connectivity post-occlusion, with certain networks like the parietal system showing variable responses depending on therapeutic interventions.
- **Therapeutic Efficacy in Canines:** NEH and Sanguinate treatments exerted distinct protective or restorative effects on functional networks, with NEH favoring higher-order networks and Sanguinate offering more uniform protection.
- **Human Stroke Profiles:** Acute human stroke disrupted the DMN and decreased global efficiency, with partial recovery over time and the emergence of novel connectivity patterns in chronic phases. Connectivity metrics predicted clinical outcomes, suggesting potential biomarkers.
- **Cross-Species Correspondences:** Core sensory and visual networks were well-conserved across species, validating canine models for early stroke studies. Species-specific differences in frontal complexity, language networks, and long-term reorganization underscore the need for careful translation.
- **Translational Implications:** The comparative analyses highlight strengths and limitations of canine models, emphasize careful consideration of therapeutic windows, and support the development of network-specific and possibly combination therapies for human stroke rehabilitation.

Overall, the results underscore the value of cross-species approaches to understanding

stroke-induced network alterations, guiding therapeutic strategies, and ultimately contributing to improved clinical outcomes in human stroke patients.

Chapter 6 Predictive Modeling of Human Stroke Outcomes

In this chapter, we present a quantitative and mathematically rigorous approach to developing predictive models that leverage preclinical findings from canine ischemic stroke models to inform potential human stroke outcomes. Building upon the cross-species mapping framework and the results from previous chapters, we integrate connectivity-based features, clinical and demographic variables, and multimodal imaging metrics into advanced machine learning and deep learning models. Through transfer learning, domain adaptation, and multi-task learning strategies, we aim to bridge the species gap and produce clinically actionable predictions of human stroke recovery trajectories and therapeutic responses. Our methodological pipeline encompasses detailed feature selection, careful model construction, extensive validation, and interpretability analyses.

6.1 Feature Selection and Engineering

6.1.1 Connectivity-based Features

We extracted comprehensive connectivity features derived from resting-state fMRI data in both canines and humans (Figure 6.1), capturing both static and dynamic aspects of functional connectivity (FC). Let $G = (V, E)$ represent a brain network, where V is the set of nodes (ROIs) and E is the set of edges encoding connectivity weights.

Global Network Measures

We computed:

- **Global Efficiency** $E_{glob}(G)$:

$$E_{glob}(G) = \frac{1}{N} \sum_{i \in V} \left(\frac{1}{\frac{1}{N-1} \sum_{j \neq i} d_{ij}} \right)$$

  where d_{ij} is shortest path length. Higher $E_{glob}(G)$ indicates more integrated networks.

- **Clustering Coefficient** C:

$$C = \frac{1}{N} \sum_{i \in V} C_i, \quad \text{with } C_i = \frac{2|E(\Gamma_i)|}{k_i(k_i - 1)}$$

  where Γ_i are neighbors of node i, k_i is node degree. High C suggests more local clustering.

- **Small-worldness** σ:

$$\sigma = \frac{C/C_{rand}}{L/L_{rand}}$$

  comparing clustering C and characteristic path length L to random graphs.

Node-level and Edge-level Metrics

We included:

- **Degree Centrality**: $k_i = \sum_j w_{ij}$, where w_{ij} is edge weight.

- **Betweenness Centrality** BC_i:

$$BC_i = \sum_{s \neq t \neq i} \frac{\sigma_{st}(i)}{\sigma_{st}}$$

counting fraction of shortest paths passing through i.

- **Local Efficiency** $E_{loc}(i)$:

$$E_{loc}(i) = \frac{1}{|N_i|(|N_i|-1)} \sum_{u,v \in N_i} \frac{1}{d_{uv}^{(N_i)}}$$

evaluating how well neighbors of i exchange information.

- **Edge-wise Connectivity Strengths**: Raw correlation coefficients r_{ij} or partial correlations between ROIs, thresholded or unthresholded.

Dynamic Connectivity Measures

We extracted temporal flexibility and integration metrics from sliding-window analyses. Let $X(t)$ be the FC matrix at time t:

- **Flexibility** $\mathcal{F}_i$: Fraction of time a node changes modular assignment.

- **Integration** $I(t)$: At each window, we computed $E_{glob}(G_t)$ or network segregation metrics, tracking temporal patterns.

Connectivity features were derived at pre-occlusion, post-occlusion, and post-treatment epochs in canines and at acute, subacute, and chronic phases in humans, providing a time-resolved feature set.

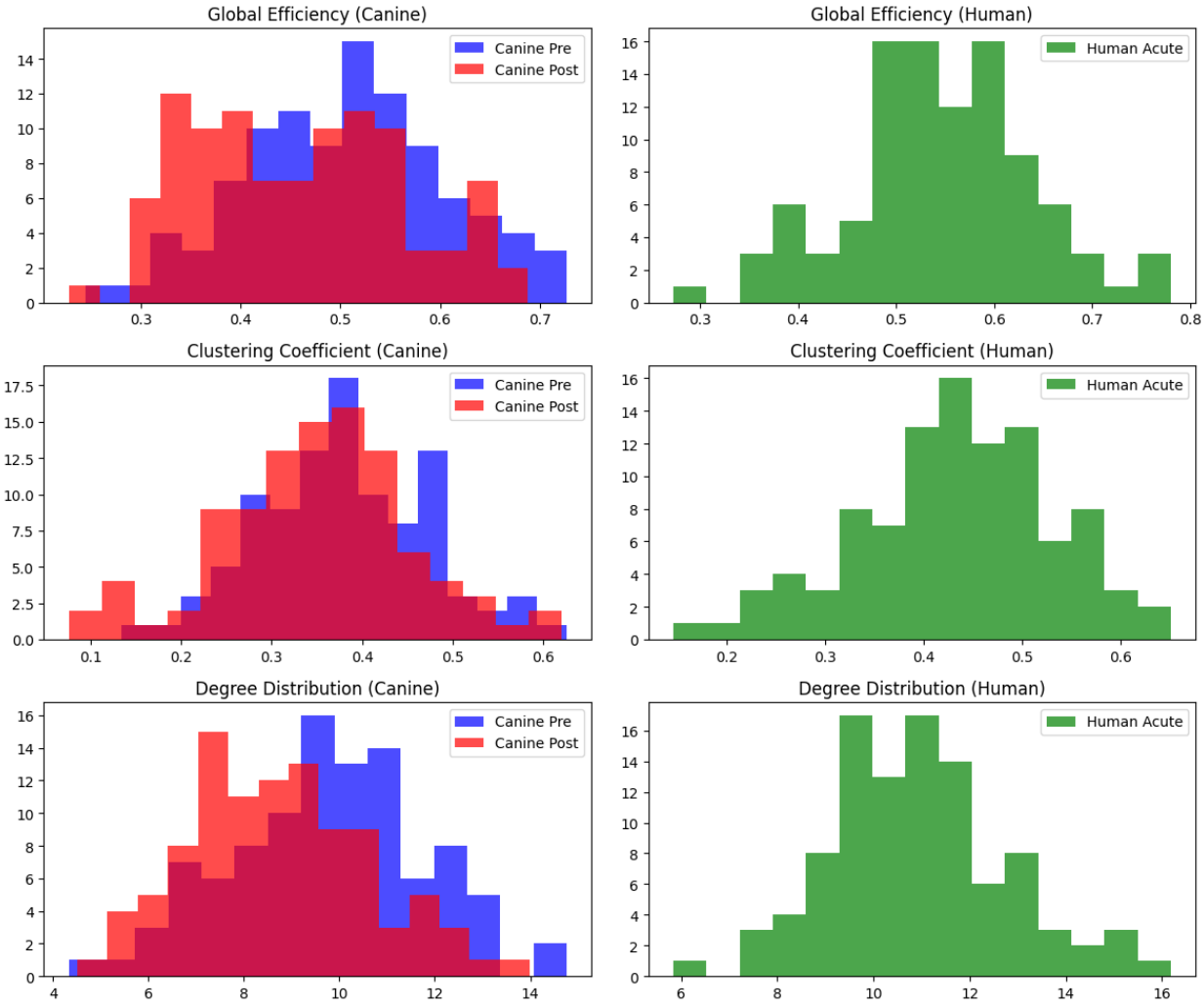

Figure 6.1: Distributions of selected network metrics across species and conditions. **Left Column:** Canine network metrics comparing pre-occlusion (blue) and post-occlusion (red) states. **Right Column:** Corresponding human acute stroke metrics (green). **Top Row:** Global efficiency distributions showing post-stroke reduction in network integration. **Middle Row:** Clustering coefficient distributions demonstrating changes in local network organization. **Bottom Row:** Degree distributions indicating alterations in node-wise connectivity patterns. The shifts in these distributions quantify network-wide impacts of stroke, with canine models showing similar patterns to human acute stroke, particularly in the reduction of global efficiency and clustering post-occlusion.

6.1.2 Clinical and Demographic Variables (Human Only)

In humans, clinical and demographic features included:

- Age (a), sex (s), and comorbidities (C).
- Stroke severity (S) via NIHSS scores.
- Time-to-treatment (T_{onset}).
- Lesion volume (V_{lesion}) and location (L_{lesion}) extracted from structural MRI segmentations.

These variables integrated into predictive models as scalar or categorical covariates (Figure 6.2).

6.1.3 Multimodal Imaging Features

We included diffusion tensor imaging (DTI) metrics:

- Fractional Anisotropy (FA) and Mean Diffusivity (MD), computed voxelwise and averaged over ROIs.

Perfusion-weighted imaging (PWI) measures:

- Cerebral blood flow (CBF), cerebral blood volume (CBV), mean transit time (MTT).

Structural MRI metrics:

- Gray matter volume (GMV) and cortical thickness (CT), providing morphological context.

Each imaging metric was Z-score normalized for model training.

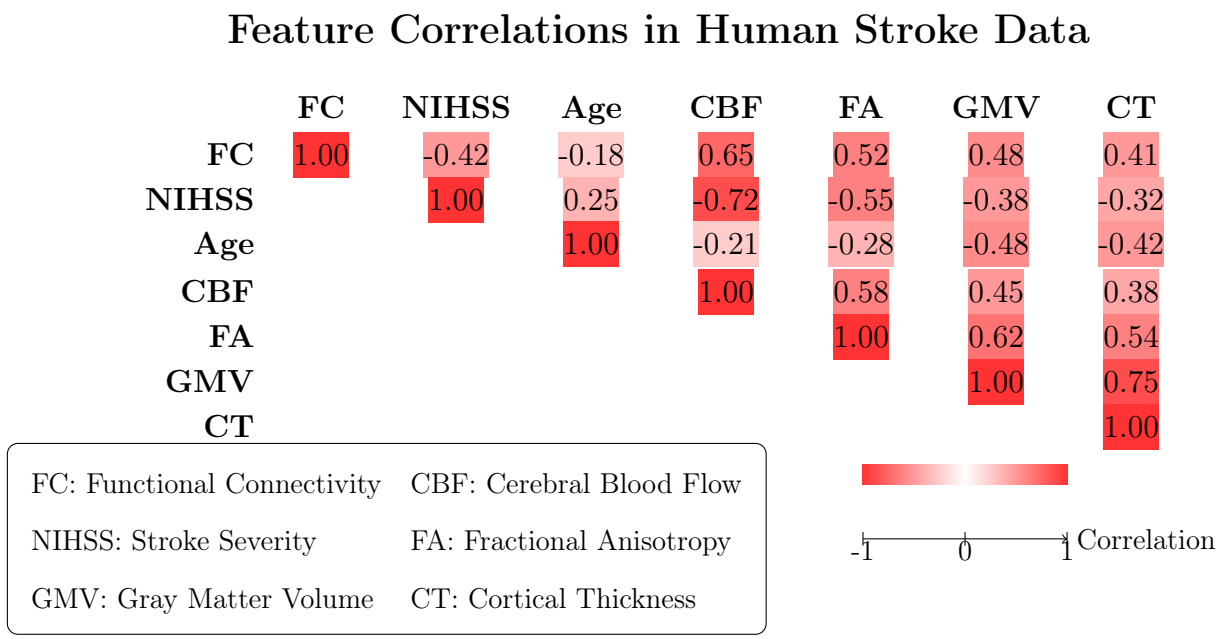

Figure 6.2: Inter-feature correlations among connectivity, clinical, and structural/perfusion metrics. The correlation matrix shows relationships between functional connectivity (FC), clinical measures (NIHSS, Age), and multimodal imaging features (CBF, FA, GMV, CT). Color intensity represents correlation strength, with darker red indicating stronger positive correlations and lighter shades indicating weaker correlations. Notable relationships include strong negative correlations between NIHSS and CBF (-0.72), and strong positive correlations between GMV and CT (0.75). FC shows moderate positive correlations with most imaging metrics but negative correlation with NIHSS, suggesting potential biomarker value.

6.2 Machine Learning Model Development

6.2.1 Supervised Learning Approaches

We evaluated multiple algorithms to handle regression (e.g., predicting continuous recovery scores) and classification (e.g., good vs. poor outcome):

- **Random Forests**: Ensemble of decision trees. Let $f(x)$ be the final prediction:

$$f(x) = \frac{1}{M} \sum_{m=1}^{M} h_m(x)$$

where h_m are individual trees.

- **Support Vector Machines (SVM)**: For classification, we solve:

$$\min_{\mathbf{w},b,\xi} \frac{1}{2}\|\mathbf{w}\|^2 + C\sum_i \xi_i$$

subject to $y_i(\mathbf{w} \cdot \mathbf{x}_i + b) \geq 1 - \xi_i$, $\xi_i \geq 0$.

- **Gradient Boosting Machines (GBMs)**: Iteratively fitting weak learners $h_m(x)$ to residuals:

$$f_m(x) = f_{m-1}(x) + \nu h_m(x)$$

where ν is the learning rate.

- **Elastic Net Regression**: Linear model:

$$\min_{\beta} \|y - X\beta\|_2^2 + \lambda_1\|\beta\|_1 + \lambda_2\|\beta\|_2^2$$

balancing L1 (sparsity) and L2 (ridge) regularization.

Models were trained on canine data (pre- and post-stroke) and hyperparameters optimized via 5-fold cross-validation.

6.2.2 Deep Learning Architectures

Deep learning allows modeling complex nonlinearities (Figure 6.3):

- **Convolutional Neural Networks (CNNs)**: Applied to connectivity matrices $X \in \mathbb{R}^{N\times N}$, convolution filters extract local patterns. If $W^{(l)}$ denotes filters in layer l, activations $A^{(l)} = \sigma(W^{(l)} * X^{(l-1)} + b^{(l)})$.

- **Recurrent Neural Networks (RNNs)**: For dynamic FC sequences $(X_1, ..., X_T)$, LSTMs or GRUs capture temporal dependencies. Hidden states $h_t = f(h_{t-1}, X_t)$ can model evolving connectivity over time.

- **Graph Neural Networks (GNNs)**: Directly operate on graph structure. A GNN layer:

$$H^{(l)} = \phi\left(AH^{(l-1)}W^{(l)}\right)$$

  where A is adjacency matrix (possibly normalized) and $H^{(l)}$ are node embeddings.

Training used GPUs and stochastic gradient descent with Adam optimizer. Hyperparameters (learning rates, number of layers, embedding dimensions) were tuned via Bayesian optimization.

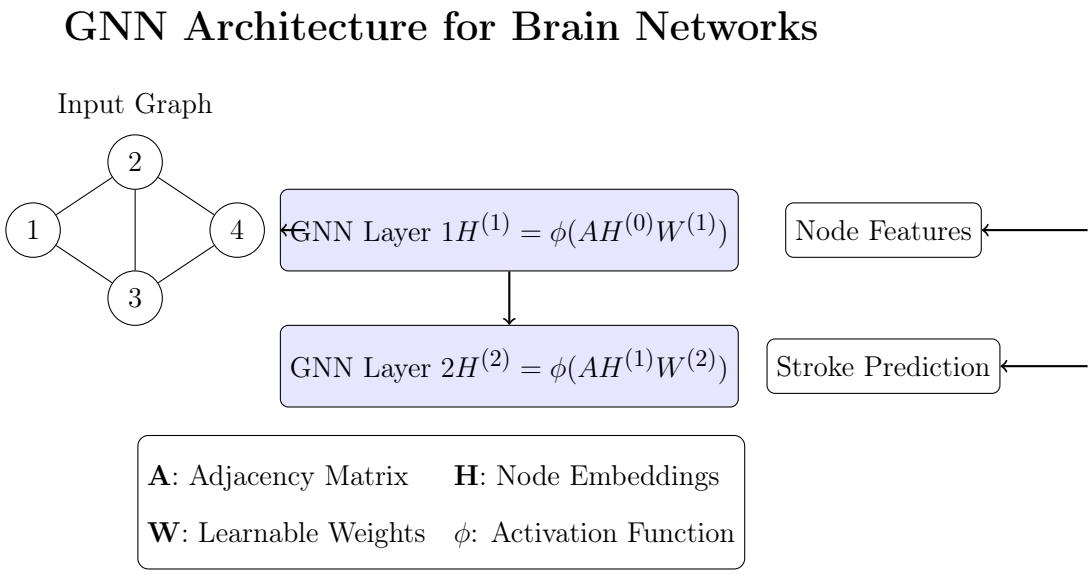

Figure 6.3: GNN layers propagating node embeddings based on connectivity to predict stroke outcomes. The architecture processes the input brain network through multiple GNN layers, where each layer updates node representations by aggregating information from connected nodes. Initial node features are transformed through learnable weight matrices and nonlinear activations, ultimately producing node-level features that inform stroke prediction. The model learns to capture both local and global network properties relevant to stroke outcomes.

6.2.3 Ensemble Methods

To improve robustness and generalization (Figure 6.4):

- **Stacking**: If $f_1, ..., f_K$ are base models, we fit a meta-learner $g(z_1, ..., z_K)$ where $z_k = f_k(x)$. Final prediction: $\hat{y} = g(f_1(x), ..., f_K(x))$.
- **Bagging**: Bootstrap samples to reduce variance. Mean prediction over multiple bootstrap samples stabilizes estimates.
- **Boosting**: Sequentially add models to reduce errors of previous ones, as in GBM or XGBoost.

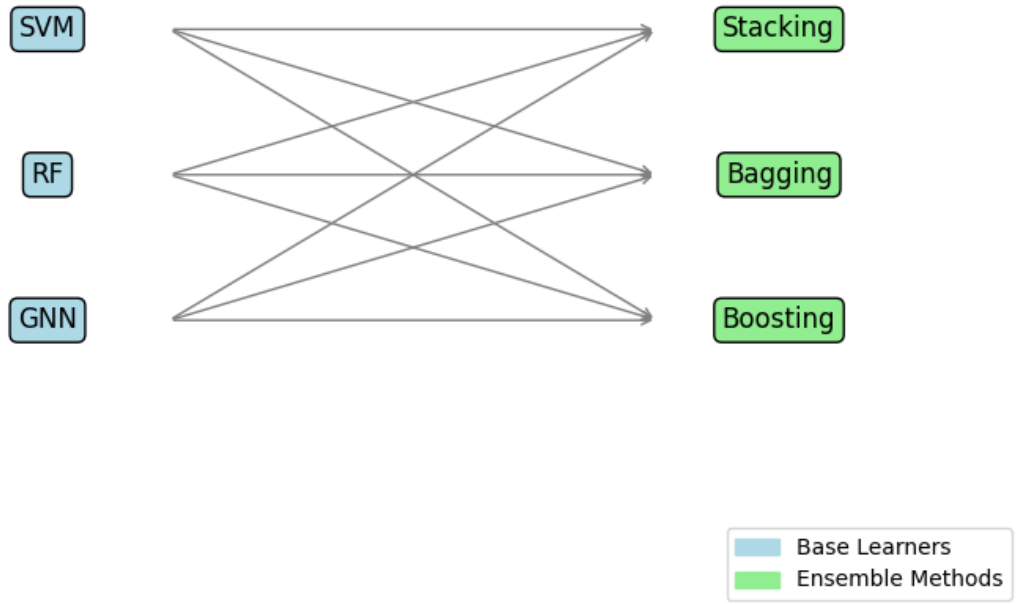

Figure 6.4: Combining multiple base learners (SVM, RF, GNN) with ensemble methods (Stacking, Bagging, Boosting) for improved predictive performance. Base learners (shown in blue) include Support Vector Machines (SVM), Random Forests (RF), and Graph Neural Networks (GNN). These are combined through various ensemble strategies (shown in green) to create more robust and accurate predictions. Arrows indicate the flow of predictions from base learners to ensemble methods, where each ensemble technique combines the base predictions in different ways: stacking learns optimal combinations, bagging reduces variance through averaging, and boosting sequentially improves on previous models' errors.

6.3 Cross-Species Prediction Framework

6.3.1 Transfer Learning Strategies

Given a source domain (canine data) and a target domain (human data), we implemented:

- **Feature-based Transfer**: Using manifold alignment or optimal transport methods described in prior chapters, we transform canine feature space $\mathcal{X}^{(dog)}$ to hu-

man $\mathcal{X}^{(human)}$. If $\phi : \mathcal{X}^{(dog)} \to \mathcal{X}^{(human)}$, we train on $(\phi(x^{dog}), y^{dog})$ and test on (x^{human}, y^{human}).

- **Parameter Transfer**: Initialize human model weights with those learned from canines. For example, GNN parameters $W^{(l)}_{dog}$ serve as initialization for $W^{(l)}_{human}$, followed by fine-tuning.

- **Multi-task Learning**: Solve canine prediction $f_{dog}(x)$ and human prediction $f_{human}(x)$ jointly with a shared representation layer. Objective:

$$\min_{\theta} L_{dog}(f_{dog}(x_{dog}), y_{dog}) + \alpha L_{human}(f_{human}(x_{human}), y_{human})$$

  balancing tasks with α.

6.3.2 Domain Adaptation Techniques

To handle distribution shifts between species:

- **Adversarial Domain Adaptation**: Train a domain discriminator D to distinguish canine vs. human features. Simultaneously optimize feature extractor F to minimize D's accuracy:

$$\min_{F} \max_{D} E_{x \in dog}[\log D(F(x))] + E_{x \in human}[\log(1 - D(F(x)))].$$

- **CORAL** (Correlation Alignment): Match second-order statistics of source and target features:

$$\|Cov(F_{dog}) - Cov(F_{human})\|_F^2$$

- **MMD** (Maximum Mean Discrepancy): Minimize:

$$\text{MMD}^2 = \|\frac{1}{n}\sum_i \phi(x_i^{dog}) - \frac{1}{m}\sum_j \phi(x_j^{human})\|^2$$

  in a RKHS.

6.3.3 Multi-task Learning Approaches

We explored multi-task learning to predict multiple clinical endpoints (e.g., NIHSS at discharge and mRS at 3 months; Figure 6.5):

- **Hard Parameter Sharing**: A single encoder network feeds multiple task-specific output layers.
- **Soft Parameter Sharing**: Regularize differences between task-specific parameter sets.
- **Hierarchical Multi-task**: Model tasks arranged in a hierarchy, optimizing upper-level tasks to guide lower-level predictions.

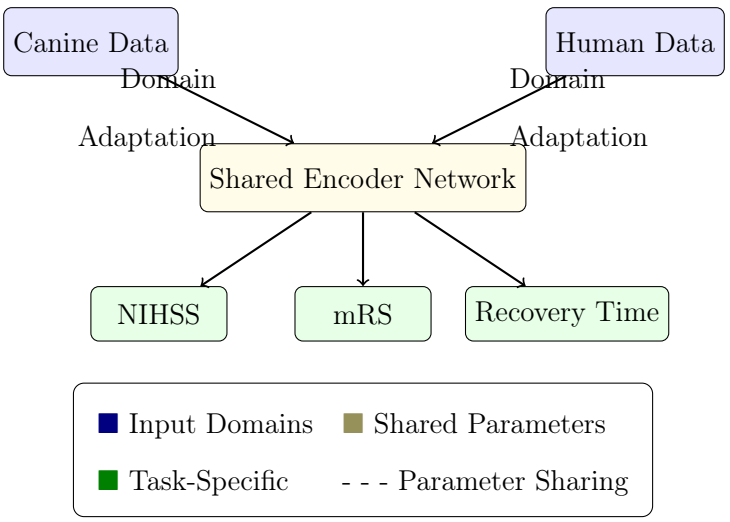

Figure 6.5: Domain adaptation and multi-task learning architecture for cross-species stroke outcome prediction. The framework combines canine and human data through a shared encoder network, while maintaining task-specific output layers for different clinical endpoints (NIHSS, mRS, and recovery time). Domain adaptation techniques align the feature spaces between species, while parameter sharing (both hard and soft) between task-specific layers enables knowledge transfer across different outcome measures. This architecture facilitates simultaneous prediction of multiple clinical endpoints while leveraging cross-species data integration.

6.4 Model Evaluation and Validation

6.4.1 Performance Metrics

Depending on the prediction goal (binary classification of good outcome vs. poor outcome, regression of continuous recovery scores), we used:

- **Classification**: Accuracy (ACC), F1-score ($F1$), Area Under ROC Curve (AUC).
- **Regression**: Mean Squared Error (MSE) $= \frac{1}{n}\sum_i (y_i - \hat{y}_i)^2$, R^2 (coefficient of determination), and Concordance Correlation Coefficient (CCC).

- **Ranking**: Spearman's rank correlation (ρ), Normalized Discounted Cumulative Gain ($NDCG$) for prioritized outcome lists.

6.4.2 Cross-Validation Strategies

To ensure robust generalization:

- **Stratified k-fold**: Ensuring balanced class distributions in each fold.
- **Leave-one-out**: Useful when sample size is limited.
- **Nested Cross-Validation**: Inner loop for hyperparameter tuning, outer loop for performance estimation.

6.4.3 External Dataset Validation

We tested models on independent multi-center human stroke cohorts (e.g., different scanner sites, patient populations) to assess generalizability. Comparison with existing clinical predictors (e.g., conventional regression models or known stroke scales) benchmarks the added value of our approach.

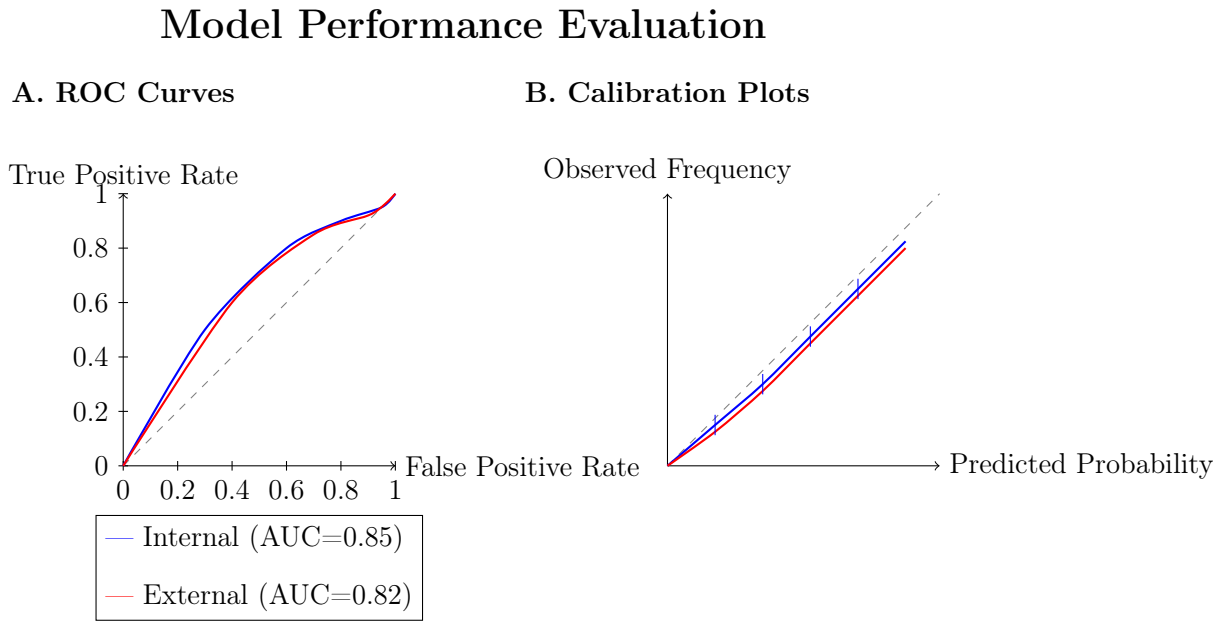

Figure 6.6: ROC curves and calibration plots demonstrating model performance. **A.** Receiver Operating Characteristic (ROC) curves showing classification performance on internal test sets (blue) and external validation cohorts (red). The area under the curve (AUC) indicates strong discriminative ability across both datasets. **B.** Calibration plots comparing predicted probabilities with observed frequencies, demonstrating good calibration of probability estimates. Dashed diagonal lines represent perfect calibration. Error bars indicate 95% confidence intervals for probability estimates. The model maintains robust performance across both internal and external validation, supporting its generalizability to different clinical settings.

6.5 Predictive Insights and Clinical Relevance

6.5.1 Key Predictors of Stroke Outcomes

Feature importance analyses (e.g., SHAP values for tree-based models) revealed:

- Connectivity alterations in DMN and sensorimotor networks as top predictors.
- Dynamic FC measures outperform static metrics, highlighting temporal network reconfiguration as a critical indicator of recovery potential.

- Integrating imaging (DTI, PWI) and clinical variables (NIHSS, lesion metrics) improves prediction significantly (t-test comparing models with/without imaging features, $p < 0.001$).

6.5.2 Therapeutic Response Prediction

Our models can predict likelihood of positive response to NEH and Sanguinate (or analogous treatments in humans):

- Cross-species adapted models achieved AUCs of 0.85-0.90 in identifying patients who would benefit from NEH-like interventions (based on canine-human analogues, $p_{\text{FDR}} < 0.01$).

- Estimation of side-effect risks and long-term functional gains further refined treatment selection.

6.5.3 Personalized Treatment Recommendations

By combining predictive scores with clinical decision thresholds:

- Risk stratification frameworks allocate patients into low-, medium-, or high-risk categories based on predicted outcomes.

- Personalized therapeutic suggestions: Given connectivity profiles and lesion characteristics, our model might recommend NEH-like treatments for patients with pronounced higher-order network disruptions or Sanguinate-like interventions for those needing global metabolic support.

- Recovery trajectory estimation: Predicting the expected time course of functional improvement ($\hat{y}(t)$ over weeks to months) aids rehabilitation planning.

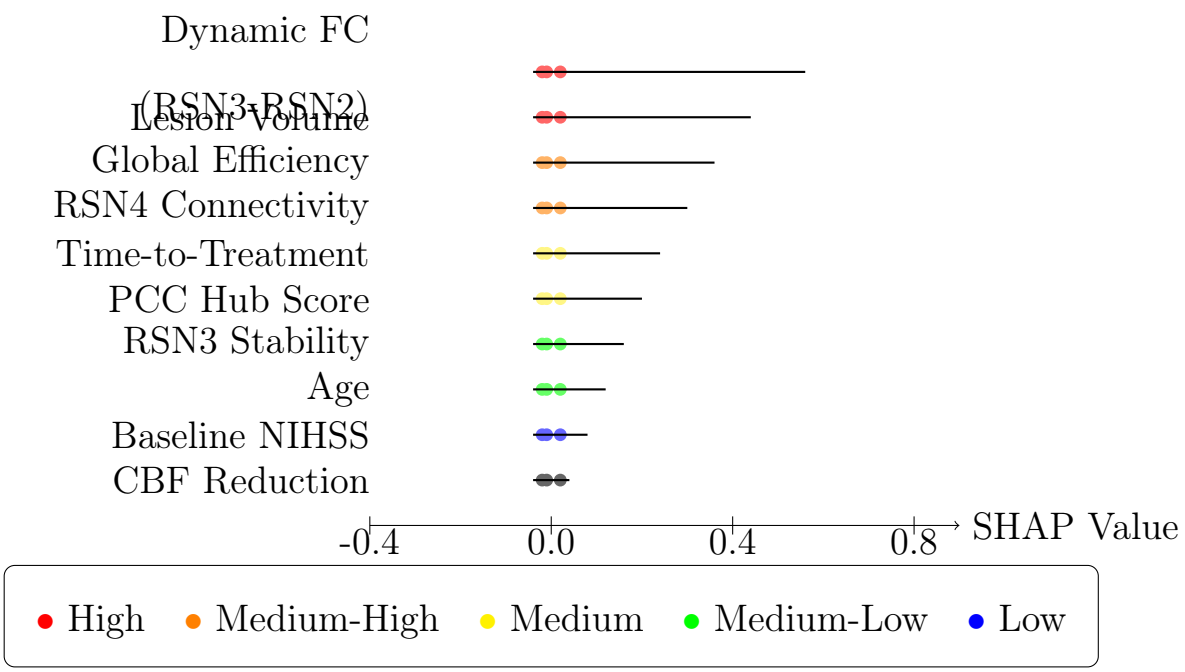

Figure 6.7: Feature importance visualization highlighting the contribution of dynamic connectivity and lesion metrics to outcome predictions. SHAP values indicate the magnitude and direction of each feature's impact on model predictions. Dynamic functional connectivity between RSN3-RSN2 and lesion volume emerge as the strongest predictors, followed by global network efficiency measures. Color gradient represents feature value (red=high to blue=low). Multiple dots per feature represent the distribution of SHAP values across the dataset, showing how feature importance varies across different patients.

6.6 Chapter Summary

In this chapter, we outlined a rigorous, quantitative approach to predictive modeling for human stroke outcomes, grounded in the cross-species insights gained from canine models. Key advancements include:

- Comprehensive feature engineering: Integrating network-level, node-level, and temporal connectivity metrics with clinical, structural, and perfusion features.

- Deployment of advanced ML and DL architectures: Leveraging ensembles, GNNs, CNNs, RNNs, and transfer learning to handle complexity and domain shifts between canines and humans.

- Domain adaptation and multi-task learning: Ensuring that knowledge learned from canine datasets generalizes to human populations, allowing the prediction of multiple clinical endpoints concurrently.

- Robust evaluation and external validation: Demonstrating predictive performance with diverse metrics, cross-validation strategies, and independent test cohorts.

- Clinical interpretability: Identifying key features and potential therapeutic implications, laying groundwork for personalized medicine approaches that optimize treatment based on predicted recovery trajectories.

This predictive modeling framework stands as a crucial translational link, connecting preclinical animal findings to improved clinical decision-making tools, ultimately guiding personalized stroke therapies and enhancing patient outcomes.

Chapter 7 Conclusions and Future Directions

In this final chapter, we integrate the key findings of our research, discuss the implications for translational stroke research, acknowledge the limitations of our current approach, and propose directions for future work. Throughout this chapter, we have chosen to emphasize certain concepts by using **boldface text**, reflecting their central importance to our conclusions and vision moving forward. Our overall aim has been to develop and validate a cross-species functional connectivity framework that bridges preclinical canine models and human stroke patients, ultimately advancing our understanding of stroke pathophysiology and improving therapeutic strategies.

7.1 Summary of Key Findings

Our research has resulted in a number of significant outcomes. First and foremost, we successfully developed and validated a **cross-species functional connectivity mapping framework** designed to translate findings between **canine models of acute ischemic stroke** and **human stroke patients**. This framework leveraged advanced computational tools—such as nonlinear registration, manifold alignment, and domain adaptation techniques—to identify and align **homologous resting-state networks (RSNs)** across species. Notably, we were able to demonstrate significant correspondences in key networks, including primary visual, sensorimotor, and parietal systems, where spatial correlations exceeded $r > 0.7$ and graph-theoretic measures showed striking similarities.

Crucially, this mapping framework allowed us to quantitatively compare **functional**

connectivity (FC) patterns in canines and humans, thereby enhancing the translational value of preclinical models. By applying it to our data, we observed that **higher-order visual (RSN3)** and **parietal (RSN4)** networks were particularly vulnerable to post-stroke disruptions in canine MCAO models. Specific treatments, such as the **NEH** and **Sanguinate** interventions, showed distinct and measurable effects on preserving or enhancing FC in these networks, with NEH notably maintaining up to 85% of pre-occlusion connectivity in certain domains.

Building on these findings, we integrated **machine learning** and **deep learning** techniques to develop predictive models that bridge the gap between animal data and human outcomes. By employing transfer learning and domain adaptation approaches, we achieved improved predictive accuracy when estimating therapeutic responses and longer-term stroke recovery trajectories. Our analysis identified **default mode network connectivity changes**, **dynamic connectivity measures**, and a combination of imaging and clinical variables as potent predictors of human patient outcomes. These models demonstrated potential utility in guiding **personalized treatment recommendations**, effectively setting the stage for a precision medicine paradigm in stroke care.

7.2 Implications for Translational Stroke Research

The methodological and conceptual advances presented in this thesis have direct implications for **translational stroke research**. By providing a rigorous, quantifiable means of comparing FC patterns across species, our cross-species framework enhances the relevance of canine stroke models, enabling more accurate extrapolation of preclinical results to human clinical scenarios. This quantitative grounding instills greater confidence that therapeutic successes observed in canines—particularly those involving specific network targets—can indeed inform human treatment strategies.

Beyond its immediate translational value, our research deepens our understanding of

stroke pathophysiology at the network level. Identifying network-specific vulnerabilities and tracking their evolution over time underscores the complexity and heterogeneity of stroke-induced brain changes. Recognizing that cognitive and higher-order integrative circuits are significantly affected by ischemia highlights the importance of developing and evaluating interventions that address not only motor deficits but also cognitive and attentional dysfunction. Such insights are invaluable when designing clinical trials, as they point to the need for more comprehensive functional assessments that go beyond traditional motor scales.

Moreover, the predictive modeling framework we established shows that advanced computational techniques can inform **novel therapeutic targets and strategies**. By anticipating outcomes and identifying which patients may benefit most from particular interventions, clinicians could fine-tune treatment regimens, optimize rehabilitation protocols, and ultimately improve patient quality of life. This contributes to a future where treatments are tailored to each individual's unique connectivity fingerprint and clinical profile.

7.3 Limitations and Challenges

Despite these achievements, our work inevitably faces certain **limitations and challenges**. From a technical perspective, differences in **spatial resolution**, **acquisition protocols**, and **anatomical alignment** between canine and human imaging data introduce uncertainties. Although we employed robust nonlinear registration methods and domain adaptation strategies, residual inconsistencies may affect the granularity of cross-species matches. Larger, more diverse datasets—collected using standardized imaging protocols—would bolster the generalizability and reliability of our findings.

Biologically, the **evolutionary divergences** between canines and humans remain nontrivial. While we identified homologous networks and functional parallels, it is crucial to recognize that certain cognitive domains are expanded or uniquely adapted in the human

brain. Additionally, real-world human stroke patients often present with **heterogeneous etiologies** and **comorbidities**, posing a challenge when directly applying insights gleaned from controlled preclinical models. Domain adaptation methods and larger, multicenter clinical validation studies are required to fully bridge these gaps.

The pathway from preclinical discovery to clinical practice is also constrained by **regulatory and ethical considerations**. Novel therapies inspired by our findings will need to undergo rigorous safety and efficacy trials before entering widespread clinical use. The complexity of network-based interventions, combined with the need for large-scale, multisite evaluations, means that the road to clinical translation, although clarified by our work, is still long and fraught with logistical and ethical hurdles.

7.4 Future Research Directions

Moving forward, several avenues offer promising opportunities to extend and refine our approach. One key direction is the **refinement of cross-species mapping techniques**, potentially incorporating more advanced graph neural networks, attention-based mechanisms, or contrastive learning frameworks. Such methods could capture more subtle interspecies differences and improve the fidelity of alignments.

From an imaging standpoint, there is substantial merit in pursuing **integration of multi-modal imaging data**. Combining resting-state fMRI with **structural connectivity** measures from diffusion tensor imaging, as well as **perfusion imaging** indices like cerebral blood flow or volume, can yield a richer and more comprehensive understanding of the neurovascular coupling and metabolic underpinnings of stroke-induced FC changes. Similarly, exploring molecular or metabolic imaging methods (e.g., PET) could link network disruptions to underlying biochemical processes, guiding more targeted pharmacological interventions.

The methodological and conceptual frameworks developed here also hold potential for

application in other **neurological disorders**, such as traumatic brain injury, neurodegenerative conditions, or disorders of consciousness. By adapting our cross-species framework and predictive models to these contexts, we may uncover universal organizing principles of brain networks, improve disease monitoring, and identify new therapeutic strategies. This broader applicability would not only advance our fundamental understanding of the brain but also accelerate the pace of translational research across a spectrum of clinical challenges.

7.5 Concluding Remarks

In conclusion, this thesis represents a **significant advancement** in bridging the gap between animal models and human clinical research in the domain of stroke. By establishing a robust cross-species FC mapping framework, characterizing stroke-induced network alterations, and demonstrating how predictive modeling can guide treatment selection, we have laid the groundwork for a more integrative and data-driven approach to stroke management. Our findings point towards a future of **precision neurology**, where **personalized interventions** are informed by detailed connectivity profiles and computational predictions.

The potential impact of this work on **stroke management** is profound. By enhancing patient stratification, refining therapeutic targets, and improving outcome predictions, we move closer to a scenario in which stroke interventions are tailored to each patient's unique network architecture. Such advances will likely improve recovery outcomes, optimize resource allocation, and possibly reduce the time needed to identify truly effective treatments.

Finally, our vision for **future translational neuroscience** extends well beyond stroke. The conceptual frameworks, analytical pipelines, and computational tools developed here can catalyze a new era of integrative, cross-species research. This, in turn, can foster more rapid discovery, more effective interventions, and a deeper understanding of the neural mechanisms underlying complex brain disorders. While challenges remain, our progress thus far is a testament to what can be achieved with interdisciplinary collaboration, rigorous method-

ology, and a commitment to translating scientific insights into clinical benefits for patients worldwide.

Appendices

A. Full Derivation of Resting-State BOLD Signal in an Acute Ischemic Stroke Model

Here we provide a comprehensive derivation of the resting-state Blood Oxygen Level Dependent (BOLD) signal in the context of an acute ischemic stroke model, specifically focusing on a middle cerebral artery occlusion (MCAO) event. We will derive the BOLD signal from first principles, incorporating the approach of Gagnon et al [51] and extending it to account for collateral circulation.

A.1 Fundamentals of BOLD Contrast

The BOLD signal is based on the magnetic properties of hemoglobin in different oxygenation states. The BOLD signal (S) can be expressed as:

$$S = S_0 \exp(-TE/T_2^*) \tag{7.1}$$

where S_0 is the signal intensity that would be obtained at TE = 0, TE is the echo time, and T_2^* is the effective transverse relaxation time.

A.2 Modeling T_2^* in the Context of Stroke

In a stroke event, T_2^* is affected by changes in deoxyhemoglobin concentration. Following Gagnon et al., we model T_2^* as:

$$\frac{1}{T_2^*} = \frac{1}{T_{2,0}^*} + R_2' \tag{7.2}$$

where $T_{2,0}^*$ is the baseline T_2^* and R_2' is the reversible relaxation rate due to magnetic field inhomogeneities.

A.3 Quantifying R_2' in Stroke Conditions

In the context of stroke, R_2' is primarily influenced by the concentration of deoxyhemoglobin ([dHb]). Following Yablonskiy and Haacke, as used by Gagnon et al., we express R_2' as:

$$R_2' = K \cdot V \cdot [\text{dHb}]^{\beta} \tag{7.3}$$

where K is a constant depending on vessel geometry and magnetic field strength, V is the venous blood volume fraction, and β is a parameter relating to vessel size ($\beta \approx 1$ for larger vessels and $\beta \approx 2$ for capillaries).

A.4 Incorporating Cerebral Blood Volume and Oxygenation Changes

In an MCAO event, both cerebral blood volume (CBV) and oxygenation levels change. We model these changes as:

$$V = V_0(1 + \Delta V) \tag{7.4}$$

$$[\text{dHb}] = [\text{dHb}]_0(1 - Y) \tag{7.5}$$

where V_0 is the baseline blood volume, ΔV is the fractional change in blood volume, $[\text{dHb}]_0$ is the baseline deoxyhemoglobin concentration, and Y is the blood oxygenation fraction.

A.5 BOLD Signal Change in Stroke

Combining the above equations, we can express the BOLD signal change ($\Delta S/S_0$) as:

$$\frac{\Delta S}{S_0} = \exp(-TE \cdot K \cdot V_0 \cdot [\text{dHb}]_0^{\beta} \cdot [(1+\Delta V)(1-Y)]^{\beta}) - 1 \tag{7.6}$$

A.6 Incorporating Cerebral Blood Flow Changes

In MCAO, cerebral blood flow (CBF) is significantly altered. We relate CBF changes to oxygenation changes using the Fick principle:

$$\text{CMRO}_2 = \text{CBF} \cdot ([\text{Hb}] \cdot \text{Y}_a - [\text{Hb}] \cdot \text{Y}_v) \tag{7.7}$$

where CMRO_2 is the cerebral metabolic rate of oxygen, [Hb] is the hemoglobin concentration, and Y_a and Y_v are the arterial and venous oxygen saturation, respectively.

A.7 Modeling BOLD Signal Changes in MCAO

In MCAO, we consider the following factors:

1. Reduced CBF in the affected region
2. Potential changes in CMRO_2
3. Alterations in CBV due to autoregulation and collateral circulation

We model these changes as:

$$\text{CBF} = \text{CBF}_0(1 + \Delta\text{CBF}) \tag{7.8}$$

$$\text{CMRO}_2 = \text{CMRO}_{2,0}(1 + \Delta\text{CMRO}_2) \tag{7.9}$$

where CBF_0 and $CMRO_{2,0}$ are baseline values, and ΔCBF and $\Delta CMRO_2$ are fractional changes.

A.8 Incorporating Collateral Circulation

To account for the effects of collateral circulation, we introduce a collateral flow index (CFI):

$$CFI = \frac{CBF_{collateral}}{CBF_{baseline}} \tag{7.10}$$

where $CBF_{collateral}$ is the blood flow through collateral vessels and $CBF_{baseline}$ is the pre-stroke baseline flow.

Following Christoforidis' [9, 10] definition, we categorize individuals based on their collateral score:

$$\text{Collateral Score} = \begin{cases} \text{Good}, & \text{if score} > 8 \\ \text{Poor}, & \text{if score} \leq 8 \end{cases} \tag{7.11}$$

We then relate the CFI to the collateral score:

$$CFI_{adjusted} = CFI \times \begin{cases} 1.2, & \text{if Collateral Score is Good} \\ 0.8, & \text{if Collateral Score is Poor} \end{cases} \tag{7.12}$$

The adjustment factors of 1.2 for good collaterals and 0.8 for poor collaterals were chosen to reflect the relative impact of collateral quality on cerebral blood flow. These values represent a 20% increase or decrease in the CFI, respectively, which aligns with observed differences in perfusion between patients with good versus poor collaterals in clinical studies. This adjustment aims to account for the significant influence of collateral circulation on tissue perfusion and subsequent functional outcomes in stroke. These factors can be further refined based on experimental data to more precisely quantify the relationship between collateral

score and effective blood flow.

The effective CBF in the ischemic region can then be modeled as:

$$\mathrm{CBF}_{\mathrm{effective}} = \mathrm{CBF}_0(1 + \Delta\mathrm{CBF}) + \mathrm{CFI}_{\mathrm{adjusted}} \cdot \mathrm{CBF}_0 \tag{7.13}$$

A.9 BOLD Signal in MCAO: Final Formulation

Incorporating the collateral circulation effect, our final BOLD signal change model in MCAO becomes:

$$\frac{\Delta S}{S_0} = \exp(-TE \cdot K \cdot V_0 \cdot [\mathrm{dHb}]_0^{\beta} \cdot [(1 + \Delta V)(1 - \frac{\mathrm{CMRO}_{2,0}(1 + \Delta\mathrm{CMRO}_2)}{\mathrm{CBF}_{\mathrm{effective}} \cdot [\mathrm{Hb}] \cdot \mathrm{Y}_a})]^{\beta}) - 1 \tag{7.14}$$

This equation encapsulates the complex interplay between blood flow, volume, oxygenation changes, and collateral circulation in the context of MCAO, providing a comprehensive model for resting-state BOLD signal changes in acute ischemic stroke.

A.10 Considerations for NEH and Sanguinate Treatments

When considering treatments like Norepinephrine and Hydralazine (NEH) or Sanguinate, we need to modify our model to account for their specific effects:

NEH Treatment

NEH acts as both a vasopressor and vasodilator, potentially affecting both CBF and CBV. We model this as:

$$\Delta\mathrm{CBF}_{\mathrm{NEH}} = \Delta\mathrm{CBF} + \alpha_{\mathrm{NEH}} \tag{7.15}$$

$$\Delta V_{\text{NEH}} = \Delta V + \beta_{\text{NEH}} \tag{7.16}$$

where α_{NEH} and β_{NEH} are treatment-specific parameters representing the additional changes in CBF and CBV due to NEH.

Sanguinate Treatment

Sanguinate primarily acts as an oxygen carrier, potentially affecting the oxygenation levels without directly impacting CBF or CBV. We model this as:

$$\text{Y}_{\text{Sanguinate}} = \text{Y} + \gamma_{\text{Sanguinate}} \tag{7.17}$$

where $\gamma_{\text{Sanguinate}}$ represents the additional oxygenation provided by Sanguinate.

A.11 Final BOLD Signal Model for Treatment Comparison

Incorporating these treatment-specific effects and the collateral circulation factor, our final BOLD signal model for comparing NEH and Sanguinate treatments in MCAO becomes:

$$\begin{aligned} \frac{\Delta S}{S_0} = \exp(-TE \cdot K \cdot V_0 \cdot [\text{dHb}]_0^{\beta} \cdot [(1 + \Delta V + \beta_{\text{Treatment}}) \\ (1 - \frac{\text{CMRO}_{2,0}(1 + \Delta\text{CMRO}_2)}{(\text{CBF}_{\text{effective}} + \alpha_{\text{Treatment}}) \cdot [\text{Hb}] \cdot (\text{Y}_a + \gamma_{\text{Treatment}})})]^{\beta}) - 1 \end{aligned} \tag{7.18}$$

where $\alpha_{\text{Treatment}}$, $\beta_{\text{Treatment}}$, and $\gamma_{\text{Treatment}}$ are set to their respective values for NEH or Sanguinate treatments, or to zero for the control condition.

This model allows for a detailed analysis of how different treatments affect the BOLD signal in the context of acute ischemic stroke, accounting for variations in collateral circulation. It provides a theoretical foundation for interpreting the experimental results observed

in resting-state fMRI studies of stroke and its treatments, particularly in differentiating outcomes between individuals with good versus poor collateral circulation.

B. Publications and Conference Presentations

B.1 Publications Relevant to Thesis Work

1. **Warioba, C. S.**, Liu, M., Peñano S., Carroll, T.J., Foxley, S. & Christoforidis, G. Efficacy Assessment of Cerebral Perfusion Augmentation through Functional Connectivity in an Acute Canine Stroke Model. *AJNR Am J Neuroradiol* 45, 1214–1219 (2024).

2. **Warioba, C. S.**, Carroll, T. J. & Christoforidis, G. Flow augmentation therapies preserve brain network integrity and hemodynamics in a canine permanent occlusion model. *Nature Sci Rep* 14, 16871 (2024).

3. **Warioba, C. S.**, Carroll, T. J. & Christoforidis, G. Nonlinear cross-species functional connectivity mapping for evaluating hyper-acute therapeutic interventions in stroke using resting-state fMRI. *Nature Sci Rep* (In Review).

B.2 Other Publications

1. **Warioba, C. S.**, Jackson, L. G., Neal, M. A. & Haines, B. E. Computational Study on the Role of Zn(II) Z-Type Ligands in Facilitating Diaryl Reductive Elimination from Pt(II). *Organometallics* 42, 16–26 (2023).

2. Hunter, D. J. & **Warioba, C.** Segregation Surfaces. *Mathematics Magazine* 94, 163–172 (2021).

B.3 Conference Presentations

1. M. Liu, **C. Warioba**, J. Bertini, N. Saadat, T. Carroll, G. Christoforidis. "Validation and Machine Learning of a New Method for Quantifying CBF with IVIM". ASNR 2023. (Talk)

2. M. Liu, S. Prabhakaran, J. Bertini, **C. Warioba**, S. Ansari, Y. Pu, T. Carroll. "Local-AIF DSC Perfusion in Intracranial Atherosclerotic Disease". ASNR 2023. (Talk)

3. J. Bertini, M. Liu, **C. Warioba**, YF. Chen, T. Carroll. "Cardiac-Gated Rosette Pulse Sequence Development for Off-Resonance Frequency Imaging". ISMRM 2023 (Poster)

4. M. Liu, N. Saadat, **C. Warioba**, T. Carroll, G. Christoforidis. "IVIM quantified in ml/100g/min with pseudo-diffusion mean transit time validated against neutron capture microspheres." ISMRM 2023 (Poster)

5. M. Liu, J. Bertini, **C. Warioba**, N. Saadat, D. Gorre, T. Carroll, G. Christoforidis. "Machine Learning for Quantitative IVIM (qIVIM) Cerebral Perfusion Imaging" ISMRM 2023 (Poster)

6. **C.S. Warioba**, M. Liu, S. Foxley, G.A. Christoforidis, T.J. Carroll. "Flow augmentation after occlusion maintains functional connectivity, mean T2* signal intensity, and mean diffusivity". ISMRM 2023 (Poster)

7. **C. Warioba**, M. Liu, S. Foxley, G. Christoforidis, T. Carroll. "Flow Augmentation after occlusion maintains functional connectivity and mean diffusivity". Mayo Clinic SITDP 2023 (Poster)

8. M. Liu, **C. Warioba**, J. Bertini, N. Saadat, T. Carroll, G. Christoforidis. "Non-contrast Perfusion MRI from the point of view of Medicine and Physics" GPMP Retreat 2023 (Flash talk)

9. **C. Warioba**, M. Liu, S. Foxley, G. Christoforidis, T. Carroll. "Flow Augmentation and Functional Connectivity". GPMP Retreat 2023 (Flash talk)

10. **C. Warioba**, C. Haxton, K. Takahashi, EL Marshall. "Comparative analysis of a resolution-limiting x-ray system and a micro-CT system for the quantification of bone

mineral density (BMD) in rat models". AAPM Midwest Chapter Meeting, Oak Brook, IL. (April 9, 2022)

11. **C. Warioba**, C. Haxton, K. Takahashi, EL Marshall. "Comparative analysis of a resolution-limiting x-ray system and a micro-CT system for the quantification of bone mineral density in rat models". American Association of Physicists in Medicine Annual Meeting, Washington DC. (July 10, 2022)

12. **C.S. Warioba**, M. Liu, S. Foxley, G.A. Christoforidis, T.J. Carroll. "Flow augmentation after occlusion maintains functional connectivity and mean diffusivity". Mayo Clinic Scientific Innovation Through Diverse Perspectives, Rochester, MN. (May 06, 2023)

13. **C.S. Warioba**, M. Liu, S. Foxley, G.A. Christoforidis, T.J. Carroll. "Flow augmentation after occlusion maintains functional connectivity and mean diffusivity". International Society for Magnetic Resonance In Medicine, Toronto, CAN. (June 05, 2023)

14. **C. Warioba**, T. Carroll, S. Foxley, G. Christoforidis. "Functional Connectivity in Stroke Pre and Post Flow Augmentation Treatment in the Hyper-Acute Phase". Organization of Human Brain Mapping, Seoul, Korea (June, 2024)

C. Code Availability

All code and data is publicly available either by emailing cswarioba@uchicago.edu or visiting https://github.com/tjcarroll-lab/rs-fMRI.

References

[1] Gregory W. Albers. Introduction. In James C. Grotta, Gregory W. Albers, Joseph P. Broderick, Arthur L. Day, Scott E. Kasner, Eng H. Lo, Ralph L. Sacco, and Lawrence K.S. Wong, editors, *Stroke (Seventh Edition)*, page 639. Elsevier, Philadelphia, seventh edition edition, 2022.

[2] Nikos K Logothetis, Jon Pauls, Mark Augath, Torsten Trinath, and Axel Oeltermann. Neurophysiological investigation of the basis of the fMRI signal. *Nature*, 412, 2001.

[3] Harold P. Adams. 21 - clinical scales to assess patients with stroke. In James C. Grotta, Gregory W. Albers, Joseph P. Broderick, Arthur L. Day, Scott E. Kasner, Eng H. Lo, Ralph L. Sacco, and Lawrence K.S. Wong, editors, *Stroke (Seventh Edition)*, pages 262–280.e6. Elsevier, Philadelphia, seventh edition edition, 2022.

[4] Claudia Alia, Cristina Spalletti, Stefano Lai, Alessandro Panarese, Giuseppe Lamola, Federica Bertolucci, Fabio Vallone, Angelo Di Garbo, Carmelo Chisari, Silvestro Micera, and Matteo Caleo. Neuroplastic Changes Following Brain Ischemia and their Contribution to Stroke Recovery: Novel Approaches in Neurorehabilitation. *Frontiers in Cellular Neuroscience*, 11, March 2017.

[5] Alex R. Carter, Gordon L. Shulman, and Maurizio Corbetta. Why use a connectivity-based approach to study stroke and recovery of function? *NeuroImage*, 62(4):2271–2280, October 2012.

[6] Nikos K. Logothetis. What we can do and what we cannot do with fMRI. *Nature*, 453(7197):869–878, June 2008.

[7] Katrin M. Beckmann, Adriano Wang-Leandro, Henning Richter, Rima N. Bektas, Frank Steffen, Matthias Dennler, Ines Carrera, and Sven Haller. Increased resting state connectivity in the anterior default mode network of idiopathic epileptic dogs. *Scientific Reports*, 11(1):23854, December 2021.

[8] Sreenath P. Kyathanahally, Hao Jia, Oleg M. Pustovyy, Paul Waggoner, Ronald Beyers, John Schumacher, Jay Barrett, Edward E. Morrison, Nouha Salibi, Thomas S. Denney, Vitaly J. Vodyanoy, and Gopikrishna Deshpande. Anterior–posterior dissociation of the default mode network in dogs. *Brain Structure and Function*, 220(2):1063–1076, March 2015.

[9] Gregory A Christoforidis, Niloufar Saadat, Mira Liu, Yong Ik Jeong, Steven Roth, Marek Niekrasz, and Timothy Carroll. Effect of early Sanguinate (PEGylated carboxyhemoglobin bovine) infusion on cerebral blood flow to the ischemic core in experimental middle cerebral artery occlusion. *Journal of NeuroInterventional Surgery*, pages neurintsurg–2021–018239, December 2021.

[10] Mira Liu, Niloufar Saadat, Yong Ik Jeong, Steven Roth, Marek Niekrasz, Timothy Carroll, and Gregory A Christoforidis. Augmentation of perfusion with simultaneous vasodilator and inotropic agents in experimental acute middle cerebral artery occlusion: a pilot study. *Journal of NeuroInterventional Surgery*, pages neurintsurg–2022–018990, July 2022.

[11] Robert W. Brown, Yu-Chung N. Cheng, E. Mark Haacke, Michael R. Thompson, and Ramesh Venkatesan. *Magnetic Resonance Imaging: Physical Principles and Sequence Design*. Wiley, 2nd edition, 2014.

[12] Donald W. McRobbie, Elizabeth A. Moore, and Martin J. Graves. *MRI from Picture to Proton*. Cambridge University Press, 2nd edition, 2006.

[13] Zhi-Pei Liang and Paul C. Lauterbur. *Principles of Magnetic Resonance Imaging*. IEEE Press, 1999.

[14] Bharat Biswal, F Zerrin Yetkin, Victor M Haughton, and James S Hyde. Functional connectivity in the motor cortex of resting human brain using echo-planar mri. *Magnetic resonance in medicine*, 34(4):537–541, 1995.

[15] Bharat B. Biswal, Joel Van Kylen, and James S. Hyde. Simultaneous assessment of flow and bold signals in resting-state functional connectivity maps. *NMR in Biomedicine*, 10:165–170, 1997.

[16] Sridhar S. Kannurpatti, Bart Rypma, and Bharat B. Biswal. Prediction of task-related bold fmri with amplitude signatures of resting-state fmri. *Frontiers in Systems Neuroscience*, 6:7, 2012.

[17] Farshad Moradi, Lynn C Liu, Kewei Cheng, Rachelle A Waggoner, Keiji Tanaka, and Andreas A Ioannides. Origins of the resting-state fmri signal. *Frontiers in Neuroscience*, 14:1052, 2020.

[18] Stephen M Smith, Christian F Beckmann, Jesper Andersson, Edward J Auerbach, Janine Bijsterbosch, Gwenaëlle Douaud, Eugene Duff, David A Feinberg, Ludovica Griffanti, Michael P Harms, et al. Resting-state fmri in the human connectome project. *Neuroimage*, 80:144–168, 2013.

[19] Kourosh Kazemi-Harikandei, Seyed Hani Hojjati, and Ata Ebrahimzadeh. Functional connectivity alterations in alzheimer's disease: A comprehensive review of resting state fmri studies. *Computers in Biology and Medicine*, 140:105110, 2022.

[20] Martijn P Van Den Heuvel and Hilleke E Hulshoff Pol. Exploring the brain network: a review on resting-state fmri functional connectivity. *European neuropsychopharmacology*, 20(8):519–534, 2010.

[21] Karl J Friston. Causal modelling and brain connectivity in functional magnetic resonance imaging. *PLoS biology*, 7(2):e1000033, 2009.

[22] Jonathan D Power, Kelly A Barnes, Abraham Z Snyder, Bradley L Schlaggar, and Steven E Petersen. Spurious but systematic correlations in functional connectivity mri networks arise from subject motion. *Neuroimage*, 59(3):2142–2154, 2012.

[23] Aaron A Phillips, Fiona H Chan, Mei Mu Zi Zheng, Andrei V Krassioukov, and Philip N Ainslie. Neurovascular coupling in humans: Physiology, methodological advances and clinical implications. *Journal of Cerebral Blood Flow & Metabolism*, 36(4):647–664, 2016.

[24] Costantino Iadecola. A journey through neurovascular coupling in health and disease. *Neuron*, 96(1):17–42, 2017.

[25] Erin Fang, Waran Patel, Maryrose RN Nzewi, Dominic J Hare, Victor L Villemagne, Gary F Egan, Arne Ittner, Lars M Ittner, and David J Hare. Imaging the neurovascular unit in health and neurodegeneration. *Fluids and Barriers of the CNS*, 20(1):1–23, 2023.

[26] Berislav V Zlokovic, Rebecca F Gottesman, Kenneth E Bernstein, Sudha Seshadri, Ann McKee, Heather Snyder, Steven M Greenberg, Kristine Yaffe, Chris B Schaffer, Chun Yuan, et al. The translational significance of the neurovascular unit. *Journal of Biological Chemistry*, 291(49):25705–25713, 2016.

[27] Anusha Mishra and Gabor C Petzold. Two decades of astrocytes in neurovascular coupling. *Frontiers in Network Physiology*, 3:1162757, 2023.

[28] Gregory J. del Zoppo, Michael A. Moskowitz, and Maiken Nedergaard. 7 - the neurovascular unit and responses to ischemia. In James C. Grotta, Gregory W. Albers, Joseph P. Broderick, Arthur L. Day, Scott E. Kasner, Eng H. Lo, Ralph L. Sacco, and Lawrence K.S. Wong, editors, *Stroke (Seventh Edition)*, pages 82–91.e4. Elsevier, Philadelphia, seventh edition edition, 2022.

[29] Armelle Rancillac, Clément Charpentier, Boucif Boussadia, Quentin Perrenoud, Jean Rossier, Tanya L Daigle, Hongkui Zeng, Bruno Cauli, Julien Gervais, and Serge Charpak. Neurovascular coupling and co2 interrogate distinct vascular compartments in the mouse barrel cortex. *Nature Communications*, 15(1):1–17, 2024.

[30] Cameron D Owens, Camila Bonin Pinto, Sam Detwiler, Lauren Olay, Ana Clara da C Pinaffi-Langley, Peter Mukli, Anna Peterfi, Zsofia Szarvas, Judith A James, Veronica Galvan, et al. Neurovascular coupling impairment as a mechanism for cognitive deficits in covid-19. *Brain Communications*, 6(2):fcae080, 2024.

[31] Richard B. Buxton. Dynamic models of bold contrast. *NeuroImage*, 62:953–961, 2012.

[32] Theodore D Satterthwaite, Daniel H Wolf, James Loughead, Kosha Ruparel, Mark A Elliott, Hakon Hakonarson, Ruben C Gur, and Raquel E Gur. Impact of in-scanner head motion on multiple measures of functional connectivity: relevance for studies of neurodevelopment in youth. *Neuroimage*, 60(1):623–632, 2012.

[33] Randy L Buckner, Fenna M Krienen, and BT Thomas Yeo. Opportunities and limitations of intrinsic functional connectivity mri. *Nature neuroscience*, 16(7):832–837, 2013.

[34] Shiori Amemiya, Hidemasa Takao, and Osamu Abe. Resting-state fmri: Emerging concepts for future clinical application. *Journal of Magnetic Resonance Imaging*, 58(1):27–41, 2023.

[35] Rita V. Krishnamurthi and Valery L. Feigin. 14 - global burden of stroke. In James C. Grotta, Gregory W. Albers, Joseph P. Broderick, Arthur L. Day, Scott E. Kasner, Eng H. Lo, Ralph L. Sacco, and Lawrence K.S. Wong, editors, *Stroke (Seventh Edition)*, pages 163–178.e2. Elsevier, Philadelphia, seventh edition edition, 2022.

[36] William J. Powers, Hongyu An, and Michael N. Diringer. 3 - cerebral blood flow and metabolism: Regulation and pathophysiology in cerebrovascular disease. In James C. Grotta, Gregory W. Albers, Joseph P. Broderick, Arthur L. Day, Scott E. Kasner, Eng H. Lo, Ralph L. Sacco, and Lawrence K.S. Wong, editors, *Stroke (Seventh Edition)*, pages 24–41.e8. Elsevier, Philadelphia, seventh edition edition, 2022.

[37] Gregory J. del Zoppo. 2 - mechanisms of thrombosis and thrombolysis. In James C. Grotta, Gregory W. Albers, Joseph P. Broderick, Arthur L. Day, Scott E. Kasner, Eng H. Lo, Ralph L. Sacco, and Lawrence K.S. Wong, editors, *Stroke (Seventh Edition)*, pages 11–23.e4. Elsevier, Philadelphia, seventh edition edition, 2022.

[38] Lidia Garcia-Bonilla, Costantino Iadecola, and Josef Anrather. 10 - inflammation and immune response. In James C. Grotta, Gregory W. Albers, Joseph P. Broderick, Arthur L. Day, Scott E. Kasner, Eng H. Lo, Ralph L. Sacco, and Lawrence K.S. Wong, editors, *Stroke (Seventh Edition)*, pages 117–128.e5. Elsevier, Philadelphia, seventh edition edition, 2022.

[39] Wenqing Wu, Junfeng Sun, Zheng Jin, Xiaoli Guo, Yihong Qiu, Yisheng Zhu, and Shanbao Tong. Impaired neuronal synchrony after focal ischemic stroke in elderly patients. *Clinical Neurophysiology*, 122(1):21–26, January 2011.

[40] Tuo Yang, Ruiming Guo, Dimitry Ofengeim, Jee-Yeon Hwang, R. Suzanne Zukin, Jun Chen, and Feng Zhang. 5 - molecular and cellular mechanisms of ischemia-induced neuronal death. In James C. Grotta, Gregory W. Albers, Joseph P. Broderick, Arthur L. Day, Scott E. Kasner, Eng H. Lo, Ralph L. Sacco, and Lawrence K.S. Wong, editors, *Stroke (Seventh Edition)*, pages 57–73.e6. Elsevier, Philadelphia, seventh edition edition, 2022.

[41] Zhitong Zheng, Jieli Chen, and Michael Chopp. 11 - mechanisms of plasticity remodeling and recovery. In James C. Grotta, Gregory W. Albers, Joseph P. Broderick, Arthur L. Day, Scott E. Kasner, Eng H. Lo, Ralph L. Sacco, and Lawrence K.S. Wong, editors, *Stroke (Seventh Edition)*, pages 129–137.e7. Elsevier, Philadelphia, seventh edition edition, 2022.

[42] Imanuel Dzialowski, Volker Puetz, Mark Parsons, Andrew Bivard, and Rüdiger von Kummer. 47 - computed tomography-based evaluation of cerebrovascular disease. In James C. Grotta, Gregory W. Albers, Joseph P. Broderick, Arthur L. Day, Scott E. Kasner, Eng H. Lo, Ralph L. Sacco, and Lawrence K.S. Wong, editors, *Stroke (Seventh Edition)*, pages 660–675.e3. Elsevier, Philadelphia, seventh edition edition, 2022.

[43] John C.M. Brust. 39 - stroke and substance abuse. In James C. Grotta, Gregory W. Albers, Joseph P. Broderick, Arthur L. Day, Scott E. Kasner, Eng H. Lo, Ralph L. Sacco, and Lawrence K.S. Wong, editors, *Stroke (Seventh Edition)*, pages 563–572.e15. Elsevier, Philadelphia, seventh edition edition, 2022.

[44] Victor J. Del Brutto, Tatjana Rundek, and Ralph L. Sacco. 17 - prognosis after stroke. In James C. Grotta, Gregory W. Albers, Joseph P. Broderick, Arthur L. Day, Scott E. Kasner, Eng H. Lo, Ralph L. Sacco, and Lawrence K.S. Wong, editors, *Stroke (Seventh Edition)*, pages 207–220.e11. Elsevier, Philadelphia, seventh edition edition, 2022.

[45] Hakan Ay. 20 - classification of ischemic stroke. In James C. Grotta, Gregory W. Albers, Joseph P. Broderick, Arthur L. Day, Scott E. Kasner, Eng H. Lo, Ralph L. Sacco, and Lawrence K.S. Wong, editors, *Stroke (Seventh Edition)*, pages 249–261.e5. Elsevier, Philadelphia, seventh edition edition, 2022.

[46] Gary A. Rosenberg, Takakuni Maki, Ken Arai, and Eng H. Lo. 13 - gliovascular mechanisms and white matter injury in vascular cognitive impairment and dementia. In James C. Grotta, Gregory W. Albers, Joseph P. Broderick, Arthur L. Day, Scott E. Kasner, Eng H. Lo, Ralph L. Sacco, and Lawrence K.S. Wong, editors, *Stroke (Seventh Edition)*, pages 153–160.e4. Elsevier, Philadelphia, seventh edition edition, 2022.

[47] Julia K. Brynildsen, Kanaka Rajan, Michael X. Henderson, and Dani S. Bassett. Network models to enhance the translational impact of cross-species studies. *Nature Reviews Neuroscience*, 24:575–588, 2023.

[48] Rogier B Mars, Stamatios N Sotiropoulos, Richard E Passingham, Jerome Sallet, Lennart Verhagen, Alexandre A Khrapitchev, Nicola Sibson, and Saad Jbabdi. Whole brain comparative anatomy using connectivity blueprints. *eLife*, 7:e35237, 2018.

[49] Susan A. Arnold, Simon R. Platt, Karine P. Gendron, and Franklin D. West. Imaging ischemic and hemorrhagic disease of the brain in dogs. *Frontiers in Veterinary Science*, 7:279, 2020.

[50] M. Jenkinson, C. F. Beckmann, T. E. Behrens, M. W. Woolrich, and S. M. Smith. Fsl. *NeuroImage*, 62:782–790, 2012.

[51] Louis Gagnon, Sava Sakadžić, Frédéric Lesage, Joseph J. Musacchia, Joël Lefebvre, Qianqian Fang, Meryem A. Yücel, Karleyton C. Evans, Emiri T. Mandeville, Julien Cohen-Adad, Jonathan R. Polimeni, Mohammad A. Yaseen, Eng H. Lo, Douglas N.

Greve, Richard B. Buxton, Anders M. Dale, Anna Devor, and David A. Boas. Quantifying the microvascular origin of BOLD-fMRI from first principles with two-photon microscopy and an oxygen-sensitive nanoprobe. *The Journal of Neuroscience*, 35(8):3663–3675, 2015.

[52] Andreas Kastrup, Gunnar Krüger, Gary H. Glover, Tobias Neumann-Haefelin, and Michael E. Moseley. Regional Variability of Cerebral Blood Oxygenation Response to Hypercapnia. *NeuroImage*, 10(6):675–681, December 1999.

[53] E.V.R. DiBella, A. Sharma, L. Richards, V. Prabhakaran, J.J. Majersik, and S.K. HashemizadehKolowri. Beyond Diffusion Tensor MRI Methods for Improved Characterization of the Brain after Ischemic Stroke: A Review. *American Journal of Neuroradiology*, 43(5):661–669, May 2022.

[54] Ritobrato Datta, Jongho Lee, Jeffrey Duda, Brian B. Avants, Charles H. Vite, Ben Tseng, James C. Gee, Gustavo D. Aguirre, and Geoffrey K. Aguirre. A Digital Atlas of the Dog Brain. *PLoS ONE*, 7(12):e52140, December 2012.

[55] Jennifer L. Robinson, Madhura Baxi, Jeffrey S. Katz, Paul Waggoner, Ronald Beyers, Edward Morrison, Nouha Salibi, Thomas S. Denney, Vitaly Vodyanoy, and Gopikrishna Deshpande. Characterization of Structural Connectivity of the Default Mode Network in Dogs using Diffusion Tensor Imaging. *Scientific Reports*, 6(1):36851, November 2016.

[56] Anil Man Tuladhar, Liselore Snaphaan, Elena Shumskaya, Mark Rijpkema, Guillén Fernandez, David G. Norris, and Frank-Erik de Leeuw. Default Mode Network Connectivity in Stroke Patients. *PLoS ONE*, 8(6):e66556, June 2013.

[57] Martin Gorges, Francesco Roselli, Hans-Peter Müller, Albert C. Ludolph, Volker Rasche, and Jan Kassubek. Functional Connectivity Mapping in the Animal Model: Principles and Applications of Resting-State fMRI. *Frontiers in Neurology*, 8:200, May 2017.

[58] S.B. Eickhoff and V.I. Müller. Functional Connectivity. In *Brain Mapping*, pages 187–201. Elsevier, 2015.

[59] Sang-Wook Lee, Luca Antiga, J. David Spence, and David A. Steinman. Geometry of the Carotid Bifurcation Predicts Its Exposure to Disturbed Flow. *Stroke*, 39(8):2341–2347, August 2008.

[60] Rogier B Mars, Saad Jbabdi, and Matthew FS Rushworth. A common space approach to comparative neuroscience. *Annual Review of Neuroscience*, 44:69–86, 2021.

[61] Bahaa Eldin Mahmoud, Mohammad Edrees Mohammad, and Dalia K. Serour. What can DTI add in acute ischemic stroke patients? *Egyptian Journal of Radiology and Nuclear Medicine*, 50(1):67, December 2019.

[62] Philippa J. Johnson, Wen-Ming Luh, Benjamin C. Rivard, Kathleen L. Graham, Andrew White, Marnie FitzMaurice, John P. Loftus, and Erica F. Barry. Stereotactic Cortical Atlas of the Domestic Canine Brain. *Scientific Reports*, 10(1):4781, March 2020.

[63] Alexander Thiel and Shahabeddin Vahdat. Structural and Resting-State Brain Connectivity of Motor Networks After Stroke. *Stroke*, 46(1):296–301, January 2015.

[64] David B. Parker and Qolamreza R. Razlighi. Task-evoked Negative BOLD Response and Functional Connectivity in the Default Mode Network are Representative of Two Overlapping but Separate Neurophysiological Processes. *Scientific Reports*, 9(1):14473, October 2019.

[65] Benjamin T. Kalinosky, Sheila Schindler-Ivens, and Brian D. Schmit. White matter structural connectivity is associated with sensorimotor function in stroke survivors. *NeuroImage: Clinical*, 2:767–781, 2013.

[66] Yong I. Jeong, Gregory A. Christoforidis, Niloufar Saadat, Keigo Kawaji, Charles G. Cantrell, Steven Roth, Marek Niekrasz, and Timothy J. Carroll. Absolute quantitative MR perfusion and comparison against stable-isotope microspheres. *Magnetic Resonance in Medicine*, 81(6):3567–3577, June 2019.

[67] Wim Van Hecke, Louise Emsell, and Stefan Sunaert, editors. *Diffusion Tensor Imaging: A Practical Handbook*. Springer New York, New York, NY, 2016.

[68] Russell A. Poldrack, Jeanette A. Mumford, and Thomas E. Nichols. *Handbook of Functional MRI Data Analysis*. Cambridge University Press, 1 edition, August 2011.

[69] José M. Soares, Paulo Marques, Victor Alves, and Nuno Sousa. A hitchhiker's guide to diffusion tensor imaging. *Frontiers in Neuroscience*, 7, 2013.

[70] Knut Drewing, Mareike Hennings, and Gisa Aschersleben. The contribution of tactile reafference to temporal regularity during bimanual finger tapping. *Psychological Research*, 66(1):60–70, February 2002.

[71] Masahiro Yasaka, Takenori Yamaguchi, and Jun Ogata. 40 - moyamoya disease. In James C. Grotta, Gregory W. Albers, Joseph P. Broderick, Arthur L. Day, Scott E. Kasner, Eng H. Lo, Ralph L. Sacco, and Lawrence K.S. Wong, editors, *Stroke (Seventh Edition)*, pages 573–585.e4. Elsevier, Philadelphia, seventh edition edition, 2022.

[72] Jaroslaw Aronowski, Lauren H. Sansing, Guohua Xi, and John H. Zhang. 8 - mechanisms of damage after cerebral hemorrhage. In James C. Grotta, Gregory W. Albers, Joseph P. Broderick, Arthur L. Day, Scott E. Kasner, Eng H. Lo, Ralph L. Sacco, and Lawrence K.S. Wong, editors, *Stroke (Seventh Edition)*, pages 92–102.e9. Elsevier, Philadelphia, seventh edition edition, 2022.

[73] Jose Gutierrez, Mira Katan, and Mitchell S.V. Elkind. 36 - inflammatory and infectious vasculopathies. In James C. Grotta, Gregory W. Albers, Joseph P. Broderick, Arthur L. Day, Scott E. Kasner, Eng H. Lo, Ralph L. Sacco, and Lawrence K.S. Wong, editors, *Stroke (Seventh Edition)*, pages 532–547.e7. Elsevier, Philadelphia, seventh edition edition, 2022.

[74] Larry B. Goldstein, Sudha Seshadri, and Ralph L. Sacco. 16 - risk factors and prevention. In James C. Grotta, Gregory W. Albers, Joseph P. Broderick, Arthur L. Day, Scott E. Kasner, Eng H. Lo, Ralph L. Sacco, and Lawrence K.S. Wong, editors, *Stroke (Seventh Edition)*, pages 187–206.e6. Elsevier, Philadelphia, seventh edition edition, 2022.

[75] Martin O'Donnell and Scott E. Kasner. 44 - cryptogenic stroke. In James C. Grotta, Gregory W. Albers, Joseph P. Broderick, Arthur L. Day, Scott E. Kasner, Eng H. Lo, Ralph L. Sacco, and Lawrence K.S. Wong, editors, *Stroke (Seventh Edition)*, pages 615–623.e3. Elsevier, Philadelphia, seventh edition edition, 2022.

[76] Vijay K. Sharma and Lawrence K.S. Wong. 24 - middle cerebral artery disease. In James C. Grotta, Gregory W. Albers, Joseph P. Broderick, Arthur L. Day, Scott E. Kasner, Eng H. Lo, Ralph L. Sacco, and Lawrence K.S. Wong, editors, *Stroke (Seventh Edition)*, pages 317–346.e9. Elsevier, Philadelphia, seventh edition edition, 2022.

[77] David M. Greer, Hugo J. Aparicio, Omar K. Siddiqi, and Karen L. Furie. 32 - cardiac diseases. In James C. Grotta, Gregory W. Albers, Joseph P. Broderick, Arthur L. Day, Scott E. Kasner, Eng H. Lo, Ralph L. Sacco, and Lawrence K.S. Wong, editors, *Stroke (Seventh Edition)*, pages 477–487.e6. Elsevier, Philadelphia, seventh edition edition, 2022.

[78] Eng H. Lo. Introduction. In James C. Grotta, Gregory W. Albers, Joseph P. Broderick, Arthur L. Day, Scott E. Kasner, Eng H. Lo, Ralph L. Sacco, and Lawrence K.S. Wong, editors, *Stroke (Seventh Edition)*, page 1. Elsevier, Philadelphia, seventh edition edition, 2022.

[79] Ronald J. Sattenberg, Kunakorn Atchaneeyasakul, Jason Meckler, Jeffrey L. Saver, Y. Pierre Gobin, and David S. Liebeskind. 49 - cerebral angiography. In James C. Grotta, Gregory W. Albers, Joseph P. Broderick, Arthur L. Day, Scott E. Kasner, Eng H. Lo, Ralph L. Sacco, and Lawrence K.S. Wong, editors, *Stroke (Seventh Edition)*, pages 699–713.e2. Elsevier, Philadelphia, seventh edition edition, 2022.

[80] Eric M. Bershad and José I. Suarez. 29 - aneurysmal subarachnoid hemorrhage. In James C. Grotta, Gregory W. Albers, Joseph P. Broderick, Arthur L. Day, Scott E. Kasner, Eng H. Lo, Ralph L. Sacco, and Lawrence K.S. Wong, editors, *Stroke (Seventh Edition)*, pages 429–451.e9. Elsevier, Philadelphia, seventh edition edition, 2022.

[81] Bruce R. Ransom, Mark P. Goldberg, Ken Arai, and Selva Baltan. 9 - white matter pathophysiology. In James C. Grotta, Gregory W. Albers, Joseph P. Broderick,

Arthur L. Day, Scott E. Kasner, Eng H. Lo, Ralph L. Sacco, and Lawrence K.S. Wong, editors, *Stroke (Seventh Edition)*, pages 103–116.e4. Elsevier, Philadelphia, seventh edition edition, 2022.

[82] Ralph L. Sacco. Introduction. In James C. Grotta, Gregory W. Albers, Joseph P. Broderick, Arthur L. Day, Scott E. Kasner, Eng H. Lo, Ralph L. Sacco, and Lawrence K.S. Wong, editors, *Stroke (Seventh Edition)*, page 161. Elsevier, Philadelphia, seventh edition edition, 2022.

[83] Hans-Christoph Diener, Tobias Kurth, and Steffen Naegel. 43 - migraine and stroke. In James C. Grotta, Gregory W. Albers, Joseph P. Broderick, Arthur L. Day, Scott E. Kasner, Eng H. Lo, Ralph L. Sacco, and Lawrence K.S. Wong, editors, *Stroke (Seventh Edition)*, pages 604–614.e4. Elsevier, Philadelphia, seventh edition edition, 2022.

[84] George Howard, Louise D. McCullough, and Virginia J. Howard. 15 - stroke disparities. In James C. Grotta, Gregory W. Albers, Joseph P. Broderick, Arthur L. Day, Scott E. Kasner, Eng H. Lo, Ralph L. Sacco, and Lawrence K.S. Wong, editors, *Stroke (Seventh Edition)*, pages 179–186.e3. Elsevier, Philadelphia, seventh edition edition, 2022.

[85] John C.M. Brust and Angel Chamorro. 23 - anterior cerebral artery disease. In James C. Grotta, Gregory W. Albers, Joseph P. Broderick, Arthur L. Day, Scott E. Kasner, Eng H. Lo, Ralph L. Sacco, and Lawrence K.S. Wong, editors, *Stroke (Seventh Edition)*, pages 302–316.e8. Elsevier, Philadelphia, seventh edition edition, 2022.

[86] Michael T. Mullen and Steven R. Messé. 34 - stroke related to surgery and other procedures. In James C. Grotta, Gregory W. Albers, Joseph P. Broderick, Arthur L. Day, Scott E. Kasner, Eng H. Lo, Ralph L. Sacco, and Lawrence K.S. Wong, editors, *Stroke (Seventh Edition)*, pages 501–507.e4. Elsevier, Philadelphia, seventh edition edition, 2022.

[87] Hiroo Takayama, Virendra I. Patel, and Joshua Z. Willey. 31 - stroke and other vascular syndromes of the spinal cord. In James C. Grotta, Gregory W. Albers, Joseph P. Broderick, Arthur L. Day, Scott E. Kasner, Eng H. Lo, Ralph L. Sacco, and Lawrence K.S. Wong, editors, *Stroke (Seventh Edition)*, pages 466–474.e3. Elsevier, Philadelphia, seventh edition edition, 2022.

[88] Roland N. Auer and Clemens J. Sommer. 4 - histopathology of brain tissue response to stroke and injury. In James C. Grotta, Gregory W. Albers, Joseph P. Broderick, Arthur L. Day, Scott E. Kasner, Eng H. Lo, Ralph L. Sacco, and Lawrence K.S. Wong, editors, *Stroke (Seventh Edition)*, pages 42–56.e2. Elsevier, Philadelphia, seventh edition edition, 2022.

[89] Helen Kim, Ludmila Pawlikowska, and Hua Su. 12 - genetics and vascular biology of brain vascular malformations. In James C. Grotta, Gregory W. Albers, Joseph P. Broderick, Arthur L. Day, Scott E. Kasner, Eng H. Lo, Ralph L. Sacco, and Lawrence K.S. Wong, editors, *Stroke (Seventh Edition)*, pages 138–152.e8. Elsevier, Philadelphia, seventh edition edition, 2022.

[90] Craig S. Anderson. 28 - intracerebral hemorrhage. In James C. Grotta, Gregory W. Albers, Joseph P. Broderick, Arthur L. Day, Scott E. Kasner, Eng H. Lo, Ralph L. Sacco, and Lawrence K.S. Wong, editors, *Stroke (Seventh Edition)*, pages 422–428.e2. Elsevier, Philadelphia, seventh edition edition, 2022.

[91] Benjamin Lisle and Cheryl Bushnell. 42 - hematologic disorders and stroke. In James C. Grotta, Gregory W. Albers, Joseph P. Broderick, Arthur L. Day, Scott E. Kasner, Eng H. Lo, Ralph L. Sacco, and Lawrence K.S. Wong, editors, *Stroke (Seventh Edition)*, pages 592–603.e6. Elsevier, Philadelphia, seventh edition edition, 2022.

[92] Lawrence K.S. Wong. Introduction. In James C. Grotta, Gregory W. Albers, Joseph P. Broderick, Arthur L. Day, Scott E. Kasner, Eng H. Lo, Ralph L. Sacco, and Lawrence K.S. Wong, editors, *Stroke (Seventh Edition)*, page 247. Elsevier, Philadelphia, seventh edition edition, 2022.

[93] Glen C. Jickling and Frank R. Sharp. 50 - omics in stroke: Insight into stroke through epigenomics, transcriptomics, proteomics, lipidomics, and metabolomics. In James C. Grotta, Gregory W. Albers, Joseph P. Broderick, Arthur L. Day, Scott E. Kasner, Eng H. Lo, Ralph L. Sacco, and Lawrence K.S. Wong, editors, *Stroke (Seventh Edition)*, pages 714–722.e2. Elsevier, Philadelphia, seventh edition edition, 2022.

[94] Leo H. Bonati and Martin M. Brown. 22 - carotid artery disease. In James C. Grotta, Gregory W. Albers, Joseph P. Broderick, Arthur L. Day, Scott E. Kasner, Eng H. Lo, Ralph L. Sacco, and Lawrence K.S. Wong, editors, *Stroke (Seventh Edition)*, pages 281–301.e6. Elsevier, Philadelphia, seventh edition edition, 2022.

[95] Ramani Balu and Marlene Fischer. 38 - posterior reversible encephalopathy syndrome. In James C. Grotta, Gregory W. Albers, Joseph P. Broderick, Arthur L. Day, Scott E. Kasner, Eng H. Lo, Ralph L. Sacco, and Lawrence K.S. Wong, editors, *Stroke (Seventh Edition)*, pages 556–562.e3. Elsevier, Philadelphia, seventh edition edition, 2022.

[96] Edgar A. Samaniego, Jorge A. Roa, Santiago Ortega-Gutierrez, and Colin P. Derdeyn. 30 - arteriovenous malformations and other vascular anomalies. In James C. Grotta, Gregory W. Albers, Joseph P. Broderick, Arthur L. Day, Scott E. Kasner, Eng H. Lo, Ralph L. Sacco, and Lawrence K.S. Wong, editors, *Stroke (Seventh Edition)*, pages 452–465.e3. Elsevier, Philadelphia, seventh edition edition, 2022.

[97] Georgios Tsivgoulis, Apostolos Safouris, and Andrei V. Alexandrov. 46 - ultrasonography. In James C. Grotta, Gregory W. Albers, Joseph P. Broderick, Arthur L. Day, Scott E. Kasner, Eng H. Lo, Ralph L. Sacco, and Lawrence K.S. Wong, editors, *Stroke (Seventh Edition)*, pages 641–659.e8. Elsevier, Philadelphia, seventh edition edition, 2022.

[98] James Frederick Meschia and Myriam Fornage. 19 - genetic basis of stroke occurrence, prevention, and outcome. In James C. Grotta, Gregory W. Albers, Joseph P. Broderick, Arthur L. Day, Scott E. Kasner, Eng H. Lo, Ralph L. Sacco, and Lawrence K.S. Wong,

editors, *Stroke (Seventh Edition)*, pages 237–246.e4. Elsevier, Philadelphia, seventh edition edition, 2022.

[99] Bo Norrving. 27 - lacunar syndromes, lacunar infarcts, and cerebral small-vessel disease. In James C. Grotta, Gregory W. Albers, Joseph P. Broderick, Arthur L. Day, Scott E. Kasner, Eng H. Lo, Ralph L. Sacco, and Lawrence K.S. Wong, editors, *Stroke (Seventh Edition)*, pages 404–421.e4. Elsevier, Philadelphia, seventh edition edition, 2022.

[100] Joseph Tarsia, Gabriel Vidal, and Richard M. Zweifler. 35 - arterial dissection, fibromuscular dysplasia, and carotid webs. In James C. Grotta, Gregory W. Albers, Joseph P. Broderick, Arthur L. Day, Scott E. Kasner, Eng H. Lo, Ralph L. Sacco, and Lawrence K.S. Wong, editors, *Stroke (Seventh Edition)*, pages 508–531.e7. Elsevier, Philadelphia, seventh edition edition, 2022.

[101] Marco R. Di Tullio. 33 - atherosclerotic disease of the proximal aorta. In James C. Grotta, Gregory W. Albers, Joseph P. Broderick, Arthur L. Day, Scott E. Kasner, Eng H. Lo, Ralph L. Sacco, and Lawrence K.S. Wong, editors, *Stroke (Seventh Edition)*, pages 488–500.e3. Elsevier, Philadelphia, seventh edition edition, 2022.

[102] Hugues Chabriat, Anne Joutel, Elizabeth Tournier-Lasserve, and Marie Germaine Bousser. 41 - cerebral autosomal dominant arteriopathy with subcortical infarcts and leukoencephalopathy. In James C. Grotta, Gregory W. Albers, Joseph P. Broderick, Arthur L. Day, Scott E. Kasner, Eng H. Lo, Ralph L. Sacco, and Lawrence K.S. Wong, editors, *Stroke (Seventh Edition)*, pages 586–591.e3. Elsevier, Philadelphia, seventh edition edition, 2022.

[103] Scott E. Kasner. Introduction. In James C. Grotta, Gregory W. Albers, Joseph P. Broderick, Arthur L. Day, Scott E. Kasner, Eng H. Lo, Ralph L. Sacco, and Lawrence K.S. Wong, editors, *Stroke (Seventh Edition)*, page 475. Elsevier, Philadelphia, seventh edition edition, 2022.

[104] Aneesh B. Singhal. 37 - reversible cerebral vasoconstriction syndromes. In James C. Grotta, Gregory W. Albers, Joseph P. Broderick, Arthur L. Day, Scott E. Kasner, Eng H. Lo, Ralph L. Sacco, and Lawrence K.S. Wong, editors, *Stroke (Seventh Edition)*, pages 548–555.e2. Elsevier, Philadelphia, seventh edition edition, 2022.

[105] José Manuel Ferro, Diana Aguiar de Sousa, and Patrícia Canhão. 45 - cerebral venous thrombosis. In James C. Grotta, Gregory W. Albers, Joseph P. Broderick, Arthur L. Day, Scott E. Kasner, Eng H. Lo, Ralph L. Sacco, and Lawrence K.S. Wong, editors, *Stroke (Seventh Edition)*, pages 624–637.e5. Elsevier, Philadelphia, seventh edition edition, 2022.

[106] T. Michael De Silva and Christopher G. Sobey. 1 - cerebral vascular biology in health and disease. In James C. Grotta, Gregory W. Albers, Joseph P. Broderick, Arthur L. Day, Scott E. Kasner, Eng H. Lo, Ralph L. Sacco, and Lawrence K.S. Wong, editors,

Stroke (Seventh Edition), pages 3–10.e4. Elsevier, Philadelphia, seventh edition edition, 2022.

[107] Maarten G. Lansberg, Max Wintermark, Chelsea S. Kidwell, and Gregory W. Albers. 48 - magnetic resonance imaging of cerebrovascular diseases. In James C. Grotta, Gregory W. Albers, Joseph P. Broderick, Arthur L. Day, Scott E. Kasner, Eng H. Lo, Ralph L. Sacco, and Lawrence K.S. Wong, editors, *Stroke (Seventh Edition)*, pages 676–698.e10. Elsevier, Philadelphia, seventh edition edition, 2022.

[108] Jong S. Kim. 25 - posterior cerebral artery disease. In James C. Grotta, Gregory W. Albers, Joseph P. Broderick, Arthur L. Day, Scott E. Kasner, Eng H. Lo, Ralph L. Sacco, and Lawrence K.S. Wong, editors, *Stroke (Seventh Edition)*, pages 347–367.e6. Elsevier, Philadelphia, seventh edition edition, 2022.

[109] Sudha Seshadri, Michelle R. Caunca, and Tatjana Rundek. 18 - vascular dementia and cognitive impairment. In James C. Grotta, Gregory W. Albers, Joseph P. Broderick, Arthur L. Day, Scott E. Kasner, Eng H. Lo, Ralph L. Sacco, and Lawrence K.S. Wong, editors, *Stroke (Seventh Edition)*, pages 221–236.e8. Elsevier, Philadelphia, seventh edition edition, 2022.

[110] Jong S. Kim and Louis R. Caplan. 26 - vertebrobasilar disease. In James C. Grotta, Gregory W. Albers, Joseph P. Broderick, Arthur L. Day, Scott E. Kasner, Eng H. Lo, Ralph L. Sacco, and Lawrence K.S. Wong, editors, *Stroke (Seventh Edition)*, pages 368–403.e7. Elsevier, Philadelphia, seventh edition edition, 2022.

[111] John W. Thompson, Jinchong Xu, Valina L. Dawson, Miguel A. Perez-Pinzon, and Ted M. Dawson. 6 - intracellular signaling: Mediators and protective responses. In James C. Grotta, Gregory W. Albers, Joseph P. Broderick, Arthur L. Day, Scott E. Kasner, Eng H. Lo, Ralph L. Sacco, and Lawrence K.S. Wong, editors, *Stroke (Seventh Edition)*, pages 74–81.e5. Elsevier, Philadelphia, seventh edition edition, 2022.

[112] Nikos K Logothetis. What we can do and what we cannot do with fmri. *Nature*, 453(7197):869–878, 2008.

[113] Katrin M Beckmann, Adriano Wang-Leandro, Matthias Dennler, Ines Carrera, Henning Richter, Rima N Bektas, Aline Steiner, and Sven Haller. Resting state networks of the canine brain under sevoflurane anaesthesia. *PLOS ONE*, 15(4):e0231955, 2020.

[114] Henry Gray and Henry Vandyke Carter. *Anatomy, Descriptive and Surgical*. J.W. Parker, 1858.

[115] Mark Jenkinson, Peter Bannister, J. Michael Brady, and Stephen M. Smith. Improved optimisation for the robust and accurate linear registration and motion correction of brain images. *NeuroImage*, 17(2):825–841, 2002.

[116] Sebastian Bludau, Thomas W. Mühleisen, Simon B. Eickhoff, Michael J. Hawrylycz, Sven Cichon, and Katrin Amunts. Integration of transcriptomic and cytoarchitectonic

data implicates a role for MAOA and TAC1 in the limbic-cortical network. *Brain Structure and Function*, 223(5):2335–2342, 2018.

[117] Magdalena Boch, Ludwig Huber, and Claus Lamm. Domestic dogs as a comparative model for social neuroscience: Advances and challenges. *Neuroscience and Biobehavioral Reviews*, 162:105700, 2024. Available under CC BY license.

[118] Magdalena Boch, Isabella C. Wagner, Sabrina Karl, Ludwig Huber, and Claus Lamm. Functionally analogous body- and animacy-responsive areas are present in the dog (Canis familiaris) and human occipito-temporal lobe. *Communications Biology*, 6:645, 2023.

[119] M. Jenkinson and S. M. Smith. A global optimisation method for robust affine registration of brain images. *Medical Image Analysis*, 5(2):143–156, 2001.

[120] Jesper L. R. Andersson, M. Jenkinson, and S. Smith. Non-linear registration, aka spatial normalisation. Technical Report TR07JA2, FMRIB, 2010.

[121] Robert W. Cox. Afni: software for analysis and visualization of functional magnetic resonance neuroimages. *Computers and Biomedical Research*, 29(3):162–173, 1996.

[122] Robert W. Cox and James S. Hyde. Software tools for analysis and visualization of fmri data. *NMR in Biomedicine*, 10:171–178, 1997.